Multi-scale modeling of geometric flow control in lateral flow assays

Zur Erlangung des akademischen Grades eines
Doktors der Ingenieurwissenschaften (Dr.-Ing.)
von der KIT-Fakultät für Maschinenbau des
Karlsruher Instituts für Technologie (KIT)

genehmigte
Dissertation
von

Farshid Jamshidi, M.Sc.

Tag der mündlichen Prüfung:	10.01.2025
Hauptreferentin:	Prof. Dr. rer. nat. Britta Nestler
Korreferentin:	Prof. Dr.-Ing. Jennifer Niessner

Abstract

Lateral flow assays (LFAs), such as pregnancy tests, are gaining significant interest due to their cost-effectiveness and suitability for resource-limited settings. However, challenges exist in fully understanding the underlying phenomena governing LFA performance, particularly in enhancing test sensitivity. Conventional approaches rely primarily on macro-scale experiments, which can be limited in capturing key mechanisms that occur at different length scales. In contrast, this dissertation addresses these limitations by employing multi-scale investigations that encompass both micro and macro-scale phenomena to comprehensively understand the governing processes in LFAs.

At the micro-scale, various parameters affecting wetting in porous polymeric membranes are investigated. These parameters include porosity, mean and effective pore radius, mean ligament radius, permeability, and tortuosity. To evaluate these parameters, the reconstructed digital twins of real porous membranes in equidistant three-dimensional grids are analyzed.

At the macro-scale, three complementary approaches are adopted: i) Experimental investigation: The gravimetric method is utilized to determine the porosity of the membrane, and the macro-scale wetting experiments are conducted to measure the wetting time and then calculate the wetting velocity. ii) Single-phase modeling: This approach studies fluid flow at the macro-scale in porous membrane structures, with and without variations in cross-section. The focus is on the analysis of the effect of geometric changes on the wetting process. This includes the study of different membrane geometries, such as hexagonal and T-shaped profiles. This proposed approach, centered on geometry tuning, serves as a basis for the development of application-specific membranes. iii) Two-phase simulation: A macroscopic two-phase model is implemented to investigate fluid flow in LFAs. This model accounts for the displacement of an initial fluid by an invading fluid during imbibition. Microscopic properties are incorporated as input to the macroscopic numerical simulations, allowing the study of wetting behavior in different LFAs. This multi-scale approach investigates capillary-driven flows in bifurcated (Y-shaped) and multi-branch membranes that are integral components of multiplexed LFAs. The study includes various parameters such as length ratio, width ratio, branching angle, bifurcation point location, inlet width, asymmetry, and membrane type.

In addition, a convection-diffusion-reaction model is employed as a systematic tool to address the challenge of quantitatively assessing signal intensity in LFAs. By leveraging data-driven information and understanding structure-sensitivity linkages, this multi-scale approach significantly contributes to ongoing efforts to improve the sensitivity of diagnostic assays.

The approaches presented in this work provide a comprehensive understanding of LFAs and facilitate their development. The knowledge gained is used to optimize design parameters, including wetting time and velocity, for specific LFA applications and target analytes.

Kurzfassung

Lateral-Flow-Assays (LFAs), wie beispielsweise Schwangerschaftstests, gewinnen aufgrund ihrer Kosteneffizienz und einfachen Handhabung in verschiedenen Forschungsbereichen zunehmend an Aufmerksamkeit. Ihre breite Anwendung erfordert jedoch ein fundiertes Verständnis der zugrunde liegenden Phänomene. Insbesondere die Verbesserung der Testempfindlichkeit, auch bekannt als Sensitivität, stellt eine zentrale Herausforderung dar, die für die zuverlässige Detektion von Zielanalyten in Proben essentiell ist.

Herkömmliche Ansätze zur Untersuchung von LFAs basieren häufig auf experimentellen Untersuchungen auf der Makro- beziehungsweise Anwendungsskala. Während diese Methoden wertvolle Einblicke in das Gesamtverhalten des Systems liefern, können sie bei der Erfassung von Schlüsselmechanismen, die auf unterschiedlichen Längenskalen ablaufen, eingeschränkt sein. Um diese Einschränkungen zu überwinden, verfolgt diese Dissertation Multiskalen-Ansätze, die sowohl mikro- als auch makroskalige Phänomene in LFAs systematisch untersuchen und miteinander verknüpfen.

Auf der Mikroskala werden die Einflussparameter auf die Benetzung in porösen Polymermembranen, dem Herzstück eines jeden LFA, detailliert analysiert. Dazu gehören die strukturellen Eigenschaften wie die Porosität, der mittlere und effektive Porenradius, der mittlere Stegradius, die Permeabilität und die Tortuosität. Diese Parameter werden anhand rekonstruierter digitaler Zwillinge realer poröser Membranstrukturen ermittelt.

Auf der Makroskala werden drei komplementäre Ansätze zur Untersuchung von Kapillarströmungsvorgängen in LFAs verwendet: i) Experimentelle Untersuchung: Zur Bestimmung struktureller Eigenschaften von porösen Membranen werden Methoden wie die Wiegemethode zur Berechnung der Porosität eingesetzt. Zur Ermittlung der Benetzungszeit und -geschwindigkeit in diesen Materialien werden sogenannte Wicking-Experimente durchgeführt. ii) Einphasenmodellierung: Dieser Ansatz konzentriert sich auf die Analyse des Einflusses geometrischer Querschnittsveränderungen auf den Benetzungsprozess in porösen Membranstrukturen. Dazu werden verschiedene Teststreifengeometrien, wie hexagonale und T-förmige Profile, untersucht. Die gewonnenen Erkenntnisse über die Beeinflussung des Fließverhaltens dienen als Grundlage für die Entwicklung anwendungsspezifischer Membranen. iii) Zweiphasensimulation: Zur Simulation des Flüssigkeitstransports in LFA wird ein makroskopisches Zweiphasenmodell implementiert. Dabei wird die Verdrängung eines initialen Fluids durch ein infiltrierendes Fluid betrachtet. Die Integration mikroskopischer Parameter in die makroskopischen Simulationen ermöglicht die Untersuchung des Benetzungsverhaltens in verschiedenen LFAs. Mit diesem Multiskalen-Ansatz werden Kapillarströmungen in Y-förmigen und mehrfach verzweigten Membranen analysiert. Dabei werden verschiedene Parameter wie Längenverhältnisse, Breitenverhältnisse und Verzweigungswinkel berücksichtigt.

Darüber hinaus wird ein Konvektions-Diffusions-Reaktionsmodell als systematisches Werkzeug zur quantitativen Bewertung der Signalintensität in LFA eingesetzt. Durch das Verständnis von Struktur-Sensitivitäts-Beziehungen leistet dieser Multiskalen-Ansatz einen wesentlichen Beitrag zur Verbesserung der Sensitivität diagnostischer Tests.

Die in dieser Dissertation vorgestellten Multiskalen-Ansätze liefern ein umfassendes Verständnis der komplexen Prozesse, die in der LFAs ablaufen. Die gewonnenen Erkenntnisse bilden die Grundlage für die Optimierung von Designparametern und die Entwicklung leistungsfähiger LFAs für ein breites Anwendungsspektrum in Forschung und Diagnostik.

Acknowledgments

I would like to express my sincere gratitude to Professor Britta Nestler for her invaluable guidance and mentorship during my time as a member of her research group. Her unwavering support has been instrumental in my academic development and research endeavors. Professor Nestler's mentorship has provided me with the autonomy to shape my research direction, delegated responsibilities within the institute, and offered unwavering support in both academic and organizational matters. Special recognition is due to Prof. Jennifer Niessner, who served as co-referee and provided an open-door policy for advice on academic and collaborative pursuits.

The realization of this endeavor owes much to the indispensable contributions of my colleagues. I am grateful to my predecessors for their programming contributions, as well as to the entire community at the Karlsruhe Institute of Technology and the Karlsruhe University of Applied Sciences. I would like to thank my colleagues Anastasia August, Patrick Altschuh, Andreas Reiter, Aron Kneer, Michael Selzer, Kaveh Dargahi Noubary, Paul Wilhelm Hoffrogge, Siamak Bayat, Willfried Kunz, Lars Christoph Griem, Saeideh Farzaneh Kalourazi, Leonie Wallat, Matthieu Laqua, and many others for their time and insightful discussions. Special thanks go to the institute administrators, Christof Ratz and Domenic Frank, and the dedicated secretariat, including Inken Heise, Birgitt Hardt, Sinan Isci, and others, for their diligent efforts in facilitating my work stay and beyond.

The collaborative success of the project is also due to the fruitful partnership with industry, in particular *Sartorius Stedim Biotech GmbH* in Göttingen, Germany.

I would like to express my sincere gratitude to Marcel Bremerich and Andrea Ernst for their invaluable help and support throughout this collaboration.

Finally, my heartfelt gratitude goes out to my family and friends, who have been steadfast companions throughout my Ph.D. journey and beyond. Special recognition goes to my sister Leyli and brother Rashid for their unique perspectives, enthusiasm, and constant support. I express my deepest gratitude to my parents for their enduring love and heartfelt messages. Throughout my academic journey and beyond, their unwavering support has been my anchor. Thank you, Baba and Maman.

Karlsruhe, January 2025 *Farshid Jamshidi*

Contents

1 Introduction

The growing use and importance of porous media in a wide variety of fields have made them a subject of great interest and research in recent decades. In engineering, porous media play a pivotal role in various scientific fields such as filtration, geotechnical exploration, and materials research. They also serve a crucial function in processes involving fluid flow, heat transfer, and mass transport, making them indispensable in the design and optimization of systems and structures [1]. In the environmental sciences, porous media have proven essential for studying phenomena related to groundwater flow, contaminant transport, and soil-water interactions. In order to manage natural resources, assess environmental impacts, and develop sustainable solutions to problems such as groundwater contamination and soil remediation, understanding the behavior of fluids and solutes in porous media is critical [2, 3]. Furthermore, applications of porous media extend beyond engineering and environmental sciences. Utilization is observed in the pharmaceutical industry, particularly in drug delivery systems and controlled-release formulations [4]. In the energy sector, porous media play an essential role in fuel cells, batteries, and energy storage, using their distinctive properties to enhance transport and conversion processes [5]. The diversity of porous media and the wide range of applications have led to significant advances in research and technology.

To further improve the performance and capabilities of porous media in various applications, scientists and engineers continue to explore novel materials, innovative manufacturing techniques, and advanced modeling approaches. As the understanding of porous media continues to evolve, the need for interdisciplinary collaboration and the exchange of knowledge between researchers from different fields becomes increasingly important. Bringing together expertise from engineering, environmental science, medicine, and related disciplines enables researchers to address complex challenges and gain new insights into the behavior and optimization of porous media.

This collaborative synergy is evident in the formulation of innovative solutions, particularly during critical scenarios such as the coronavirus disease 2019 (COVID-19) pandemic. Global research institutions and companies have been actively involved in efforts to accelerate diagnostics and mitigate the spread of the virus. One promising approach in this context is point-of-care testing (POCT). The World Health Organization (WHO) guidelines for POCT devices emphasize criteria that include affordability, sensitivity, specificity, ease of use, speed, robustness, device-free operation, and deliverability [6]. In this regard, rapid diagnostic tests (RDTs) play a key role in emergency or resource-limited healthcare settings. Among the most successful RDTs for point-of-care testing are lateral flow assays (LFAs). They are implemented in paper-based devices, which comply with WHO guidelines. This dissertation examines the propagation of fluids in LFAs, drawing on insights from a variety of fields.

1.1 Motivation

The advancement of lateral flow assays (LFAs), with a focus on improving reliability, accuracy, and functional breadth, faces several research challenges. After a brief elucidation of the mechanism of LFA, some of these challenges are discussed in more detail. Test samples (e.g., urine, serum, saliva) are combined with buffer solutions. They are then introduced into the porous media of the LFA. The liquid droplet first penetrates the depth and then spreads laterally due to capillary forces. Specifically, the changes in biochemical elements are due to convection, reaction, and diffusion processes within the LFA, with porous membranes acting as the transport pathway. The liquid encounters the immobilized antibodies on the test/control line of the LFA. After the reactions have occurred, a layer of antibody complexes remains on the outer and inner surfaces of the membrane.

This layer determines the optical manifestation of the color signals observed on the test/control line. The degree of color intensity is commonly referred to as the sensitivity of the assay.

Several challenges exist in the development of LFAs, including the need to i) minimize reagent and sample volume requirements, ii) achieve wetting over a broad range for improved quantitative results, iii) efficiently implement multiparameter assays through the integration of appropriately designed flow channels, and iv) achieve high sensitivity. These challenges underscore the necessity for robust testing and validation strategies across diverse applications [7]. Furthermore, the precise control of fluid flow in LFAs is critical, and batch-to-batch variation in paper material can lead to inconsistencies in assay results. Material and fabrication challenges extend to the limitations of conventional fabrication equipment and reduced biochemical activity efficiency due to prolonged storage [6]. Addressing these challenges, particularly by adopting a system-level perspective, enables researchers to advance the next generation of LFAs, characterized by improved sensitivity, specificity, and overall performance characteristics. This advancement holds the potential to transform diagnostic capabilities and contribute to improved healthcare outcomes.

Two distinct methodologies are employed in the study and development of LFAs: the experimental approach and the modeling approach. Conventional methodologies focus predominantly on macro-scale experiments, while modern techniques integrate mathematical modeling and computer-based simulations. The former requires state-of-the-art facilities for reliable results, while the latter often relies solely on computer resources, potentially offering cost and time savings compared to experimental investigations. It also reduces the likelihood of measurement errors due to human or equipment factors.

However, the modeling approach demands a comprehensive understanding of several aspects, including the morphology of porous membranes, fluid propagation within these membranes, and sensitivity analysis. In recent years, researchers have been investigating these phenomena. Yet, notable gaps remain, particularly in fluid propagation and sensitivity analysis within the modeling approach. This dissertation aims to provide a comprehensive study of LFAs by utilizing, synthesizing, and extending established methods documented in the literature. The intention is to address existing gaps, thereby contributing valuable insights to the field and enhancing the overall understanding of LFAs.

1.2 Objectives

The primary objective of this dissertation is to manipulate fluid propagation in lateral flow assays (LFAs) through geometric control, with the overall goal of increasing assay sensitivity.

To initiate the investigation, digital replicas of the open-cell, highly porous membrane structures commonly employed in LFAs will be generated. These digital replicas will undergo comprehensive characterization to extract micro-scale parameters such as porosity, pore radii, and ligament radii. Leveraging these digital twins and computer-aided simulation, fluid flow within the pore space will be meticulously studied to derive permeability values. Through the application of homogenization, which represents the translation of micro-scale results into macro-scale models, these effective parameters are then used in the macro-scale study of the LFA. At the macro-scale, different membrane geometries, including rectangular and hexagonal shapes, will be chosen to study the geometrical effects on fluid propagation. In addition, multi-branch geometries conducive to multi-parameter testing will be explored. Optimization of channel geometry and arrangement reduces measurement time by using parallel connections instead of the conventional series connection of test and control lines.

In addition, the dissertation aims to evaluate the sensitivity of the test using a convection-diffusion-reaction model. Furthermore, comparative experimental analyses will be conducted to validate the macroscopic modeling of fluid propagation. Taken together, these broad objectives contribute to a better understanding and control of fluid behavior in LFAs for improved test performance.

1.3 Outline

Chapter 2 functions as a thorough exploration of the theoretical underpinnings relevant to the study and the current state of research. It delves into the main theoretical foundations, explains the physical principles that govern capillary-driven fluid spreading, and describes the wetting process in detail. Special emphasis is placed on the characteristic parameters of porous materials, which serve as fundamental elements for understanding fluid flow in such media. The discussion extends to the field of lateral flow assays (LFA). Finally, computational simulation is introduced. This comprehensive review provides a solid foundation for the subsequent chapters and skillfully guides the reader through the necessary concepts.

Chapter 3 focuses on the characterization of paper-based membranes, using both computational and experimental methods over various length scales. The wetting process in porous polymeric membranes is primarily governed by effective parameters, which are derived in chapter 3. All properties related to the morphology of porous membranes, except porosity, are determined from 3D microstructures using computer-aided simulations. The porosity, on the other hand, is determined experimentally. Finally, the chapter elucidates the structural properties of two different porous membranes and provides insight into their interactions with different liquids. The knowledge gained in this chapter serves as input for the macro-scale modeling in the subsequent chapters.

In chapter 4, a macro-scale single-phase model of liquid transport in LFAs is developed to investigate the influence of membrane shape on liquid movement. Wetting behavior is investigated using different membrane geometries, and the model is validated through experimental studies. The chapter includes results on optimal test line placement and sensitivity analysis using a convection-diffusion-reaction model.

Chapter 5 presents a macro-scale two-phase model for the simulation of liquid transport in LFAs. This model is used to investigate the influence of membrane shape on liquid motion behavior. The chapter examines wetting behavior using different membrane geometries that provide multiple pathways for fluid flow. The geometries studied include Y-shaped membranes, tree-shaped networks, and multiplexed LFAs, which allow multiple tests to be performed simultaneously.

In chapter 6, the key findings of the study are summarized. Additionally, a discussion on potential areas for future research is presented.

2 Theoretical background and state of the art

This chapter explores porous media and their properties, as well as the dynamics of fluid flow through them, with a particular focus on the fundamental principles underlying lateral flow assays (LFA). The chapter concludes with an introduction to the basic principles behind the computational simulation techniques used in this thesis.

2.1 Porous media

Porous media are distinguished by the presence of dispersed voids within a solid phase. To fully characterize these structures, a thorough understanding of both the material matrix and the pore space is essential. The material matrix represents the interconnected solid framework that forms the overall structure, while the pore space is defined by the presence of pores and pore throats. Furthermore, the differentiation of pore types plays a key role in elucidating the diverse structural morphologies observed in porous media, including isolated pores, dead-end pores, and interconnected pores. A schematic cross-section, shown in Figure 2.1, illustrates these pore types [8, 9].

Based on pore connectivity, porous media can be broadly classified into two categories: closed-cell and open-cell. Closed-cell media consist mainly of isolated and dead-end pores, leading to enhanced mechanical strength-to-weight ratio and thermal conductivity when appropriate materials are used. Examples include

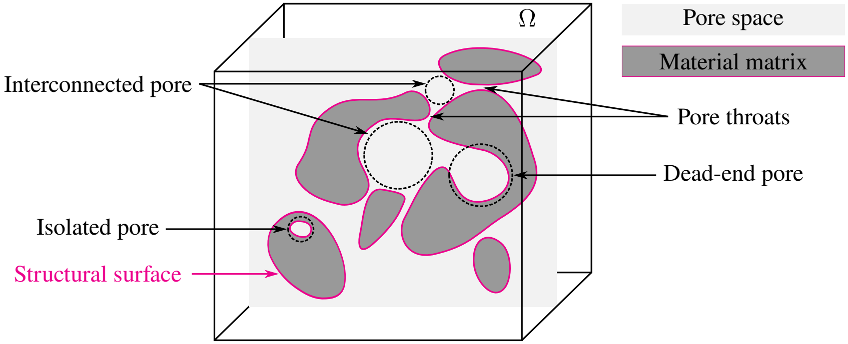

Figure 2.1: Porous structure with different types of pores.

low-density closed-cell metal foams, which exhibit exceptional stiffness, making them suitable for lightweight applications that require robust structural support. However, closed-cell structures typically have much lower fluid permeability compared to open-cell structures. Open-cell media have interconnected pores that form a continuous network, facilitating fluid flow through the material. This characteristic makes open-cell porous media highly suitable for applications in industries like the chemical industry, where fluid flow is essential. Examples of open-cell materials include sponges and ceramic foams [8–10].

This dissertation centers on the investigation of open-cell polymeric membranes employed in rapid diagnostic tests, including the rapid test for the detection of coronavirus disease 2019 (COVID-19).

2.2 Characteristic parameters of porous media

Porous materials are characterized by quantitative variables termed characteristic parameters. These parameters describe and quantify both the geometrical and topological aspects of the material. Geometrical parameters encompass properties like lengths, areas, and volumes, while topological parameters focus on the number and connectivity of voids (pores) [8]. Characteristic parameters provide quantitative measurements that facilitate the comprehension of the composition, functionality, and transport properties of a porous material. This section discusses several typical properties associated with porous media.

Porosity

Volumetric porosity, denoted as ε, is a dimensionless quantity that is defined as the ratio of the void volume ($\forall_\mathrm{p}$) to the total volume ($\forall_\Omega$) of the porous material

$$\varepsilon = \frac{\forall_\mathrm{p}}{\forall_\Omega}. \tag{2.1}$$

In the context of porous media, the void volume represents the total volume occupied by all pores within the material, including isolated pores, dead-end pores, and interconnected pores. In this study, however, the focus is specifically on porous membranes characterized by a predominance of interconnected pores that actively facilitate fluid flow. Therefore, porosity is defined in terms of the volume fraction of interconnected pores only, excluding isolated and dead-end pores that do not contribute to fluid flow.

Pore size

Despite spatial variations in the morphology and dimensions of pores within porous media, pore size remains a critical parameter for their characterization [8]. Pore identification is the process of distinguishing and delineating individual pores, essentially defining their boundaries. Following identification, pore quantification involves the measurement of various properties, such as size, shape, and distribution, to understand their influence on material behavior and performance. However, the accurate identification and quantification of pores, especially within the intricate and complex structures of porous membranes, constitutes a significant challenge. Due to this structural complexity, several distinct pore size definitions have been established, encompassing both geometric and hydraulic categories [8].

Determination of the geometric pore size requires direct measurement of the pore space. Typically, imaging techniques provide the foundation for this approach (see Figure 3.3a) [11]. In contrast, the hydraulic pore diameter (d_h) is an approximation derived from a simplified geometric model of the porous structure, often represented as a bundle of parallel capillaries of uniform size. If the cross-sectional area available for flow, i.e., the pore space area is denoted as A_p, the wetted perimeter by P, and the length by L, the hydraulic diameter can be related to the volume-specific surface area ($\mathcal{S}_{\forall}$), defined as the ratio of the structural surface area ($\mathcal{S}$) to the total volume ($\forall_\Omega$), using the following equation [12]

$$d_\mathrm{h} = 4\frac{A_\mathrm{p}}{P} = 4\frac{A_\mathrm{p}}{P} \cdot \frac{L}{L} = 4\frac{\forall_\mathrm{p}}{\mathcal{S}} \cdot \frac{\forall_\Omega}{\forall_\Omega} = 4\frac{\varepsilon}{\mathcal{S}_{\forall}}. \tag{2.2}$$

Tortuosity

Tortuosity, a defining characteristic of porous media, quantifies the degree of winding or twisting in a transport pathway. Various definitions of tortuosity have been proposed in the literature, including both geometric parameters and parameters related to hydraulic, electrical, or diffusive properties [13]. In the context of fluid flow through porous media, the presence of the matrix hinders the ability of the fluid to follow a straight line path, which is the shortest distance between two points. Thus, the geometric tortuosity (τ_geom) is expressed as the ratio of the effective length of the flow path (L_eff) to the straight line distance (L) in the macroscopic flow direction [14]

$$\tau_\mathrm{g} = \frac{L_\mathrm{eff}}{L}. \tag{2.3}$$

The straight line distance (L) can be determined by calculating the Euclidean distance between neighboring sides of the porous structure in the direction of transport [8]. The effective length (L_eff), on the other hand, is the average length of the flow paths, which can be calculated using two primary approaches. The first approach is to average the actual lengths of all flow paths, ignoring the different velocities of the fluid particles along these paths. The second approach is to average the lengths of flow paths for all fluid particles passing through a given cross-section during a given time period, resulting in a flux-weighted average. The latter approach is considered more appropriate for analyzing fluid flow in porous media. Therefore, the hydraulic tortuosity (τ_h) is defined as the square of the ratio of the flux-weighted average path length for hydraulic flow (L_eff) to the straight line length (L) [13]

$$\tau_\mathrm{h} = \left(\frac{L_\mathrm{eff}}{L}\right)^2. \tag{2.4}$$

Consequently, both the geometric and hydraulic tortuosity values are invariably greater than one. In the study of porous structures, geometric tortuosity is commonly used for simple geometries. However, when dealing with complex porous structures, an alternative approach is required to determine the effective tortuosity (τ_eff) using the effective conductivity, denoted as σ_eff. This involves considering transport as a total flow, with only the pore space as the conducting phase. The efficiency of transport within the pore space of the membrane structure with a porosity of ε is compared to an ideal pore space with the same pore volume [15]. The ideal pore space is a hypothetical construct representing a porous medium with perfectly connected, uniformly shaped pores free of any imperfections or obstructions. The effective conductivity (σ_eff) can be calculated from the porosity (ε), the conductivity of the pure pore space (σ_p), and the unknown effective tortuosity (τ_eff), as defined by the equation [8, 16]

$$\sigma_\mathrm{eff} = \frac{\varepsilon}{\tau_\mathrm{eff}}\sigma_\mathrm{p}. \tag{2.5}$$

If the effective conductivity for the complex pore space is known, the effective tortuosity can be calculated by rearranging Eq. (2.5) as $\tau_\mathrm{eff} = \varepsilon\mathscr{F}$, where $\mathscr{F}$ is the formation factor. The formation factor, a surrogate quantity that summarizes the conductivity ratio, is often determined empirically using Archie's law [17]. This empirical correlation establishes a relationship between the formation factor ($\mathscr{F}$) and the porosity (ε), expressed as $\mathscr{F} = \varepsilon^{-m}$. Therefore, an empirical correlation between effective tortuosity and porosity can be derived as [8, 13]

$$\tau_\mathrm{eff} = \varepsilon^{1-m}(m \geq 1), \tag{2.6}$$

where m represents an empirical parameter known as the cementation exponent, which typically ranges from 1.2 to 4 [18]. The value of m increases as the pore space becomes more tortuous. Furthermore, for a constant m, the tortuosity decreases with increasing porosity.

Permeability

Permeability is a critical parameter characterizing the ease with which a fluid can flow through the interconnected network of pores within a porous medium. It quantifies the resistance to fluid flow within the porous structure. Darcy's law, a fundamental principle governing fluid flow in porous media, provides a mathematical framework for relating the Darcy velocity to the driving pressure gradient [19]

$$\mathbf{u} = -\frac{\mathbf{K}\nabla p}{\mu}, \tag{2.7}$$

where $\mathbf{u}$ denotes the Darcy velocity vector, $\mathbf{K}$ the second-order permeability tensor, ∇p the pressure gradient, and μ the dynamic viscosity of the fluid. A higher permeability value signifies lower resistance to fluid flow, resulting in a reduced pressure drop across the porous medium.

The permeability of a porous medium is inherently linked to its structural characteristics, particularly its anisotropy. Structural anisotropy within a porous medium manifests as variations in permeability across different spatial directions. This directional dependence is reflected in the permeability tensor, where distinct permeability values are observed along the x, y, and z-directions in a Cartesian coordinate system.

In contrast, isotropic porous media exhibit uniform flow behavior in all directions. This isotropy is reflected in the permeability tensor, where the diagonal elements are identical, and all off-diagonal components vanish. Consequently, the permeability tensor simplifies to a scalar quantity, representing a single permeability value for the isotropic medium.

For a predominantly one-dimensional (1D) flow in the x-direction within an isotropic medium, where the flow occurs primarily along the x-axis with negligible components in the y and z-directions, the relationship between the pressure gradient and the Darcy velocity can be expressed as

$$\frac{\partial p}{\partial x} = -\frac{\mu u}{K}, \tag{2.8}$$

where $\partial p/\partial x$ is the pressure gradient in the x-direction and u is the Darcy velocity in the x-direction. The concept of Darcy velocity, alternatively referred to as superficial flow velocity, serves as a theoretical measure of velocity applicable to porous media. It is based on the assumption that only the target fluid occupies the designated cross-sectional area, disregarding the presence of other phases, particles, and the solid matrix itself. Consequently, the equation governing the superficial velocity is expressed as $u = u_{\mathrm{Darcy}} = u_{\mathrm{superficial}} = Q/A_{\mathrm{total}}$, where Q represents the volumetric flow rate and A_{total} denotes the total cross-sectional area normal to the x-direction.

Interstitial velocity refers to the velocity at which a fluid traverses the interconnected pores of a porous medium. Consequently, the void volume accessible for fluid movement within the material, denoted as $\forall_{\mathrm{p}}$, is considered when calculating the interstitial velocity. The equation for interstitial velocity is expressed as $U = U_{\mathrm{fluid}} = U_{\mathrm{interstitial}} = Q/A_{\mathrm{p}} = Q/\varepsilon A_{\mathrm{total}}$, where A_{p} represents the cross-sectional area for fluid flow and ε is the porosity of the porous medium. In conclusion, the fluid velocity (interstitial velocity) and Darcy velocity (superficial velocity) are related as $U = u/\varepsilon$. Alternatively, in vector notation, the relationship can be expressed as [20]

$$\mathbf{u} = \varepsilon \mathbf{U}. \tag{2.9}$$

Darcy's law, expressed by Eq. (2.8), establishes a mathematical relationship between Darcy velocity, permeability, pressure gradient, and fluid viscosity. Permeability, as a scalar coefficient in Darcy's law, quantifies the intrinsic geometric property of a porous medium, independent of the fluid, and is expressed in square meters (m^2). The analysis of permeability in porous media is based on several assumptions: the fluid flowing through the pores is assumed to be Newtonian, exhibiting constant viscosity despite varying shear rates; the flow regime is considered to be laminar, characterized by low velocities and smooth, predictable flow patterns; and the entire pore space is fully saturated with the fluid [21, 22].

Dimensional analysis demonstrates that permeability is influenced by both the porosity and the characteristics of the pore geometry and size. The Kozeny-Carman relationship provides a well-established, empirically derived, and dimensionally consistent correlation between these parameters [9]. The derivation of this equation commences with a comparison between the average Darcy velocity and the average velocity observed in the Hagen-Poiseuille pipe flow. The Hagen-Poiseuille equation is a well-established physical principle that governs the pressure drop experienced by an incompressible, Newtonian fluid flowing in a laminar state through a straight, cylindrical pipe with a uniform cross-sectional area [23]. The term incompressible fluid is used to describe a fluid whose density remains constant regardless of pressure variations. It is important to distinguish incompressible fluids from compressible fluids, such as gases, whose density can vary significantly with pressure changes. Newtonian fluids exhibit a linear relationship between shear stress and strain rate, resulting in a viscosity that is independent of both shear rate and stress (see section 2.3.1 for further details on viscosity). Laminar flow, in contrast to turbulent flow, represents a smooth flow regime where fluid layers move parallel to each other without any relative internal mixing or disruption.

To establish an equivalent representation of the porous structure, a bundle of straight, parallel capillaries is envisioned. Leveraging the Hagen-Poiseuille equation, the volumetric flow rate through a single cylindrical capillary can be calculated as

$$Q = \frac{\pi r_{\mathrm{p}}^4 \Delta p}{8 \mu L}, \tag{2.10}$$

where L is the length of the capillary. For a system of N parallel capillaries of equal radius (r_p), the total flow rate is expressed as

$$Q_\mathrm{total} = NQ = \frac{N\pi r_\mathrm{p}^4 \Delta p}{8\mu L} = \frac{A r_\mathrm{p}^2 \Delta p}{8\mu L}, \tag{2.11}$$

where A is the total cross-sectional area of all the capillaries. Consequently, the average velocity based on the Hagen-Poiseuille equation is given by

$$U = \frac{r_\mathrm{p}^2 \Delta p}{8\mu L}. \tag{2.12}$$

Comparing Eq. (2.8) and Eq. (2.12) leads directly to the following relationship for permeability

$$K = \frac{r_\mathrm{p}^2 \varepsilon}{8}. \tag{2.13}$$

Within the context of porous media, the hydraulic radius, defined as half the hydraulic diameter (Eq. (2.2)), can be substituted for the pore radius in Eq. (2.13). This substitution yields the Kozeny-Carman equation

$$K = \frac{\varepsilon^3}{2\mathcal{S}_{\forall}^2}. \tag{2.14}$$

By quantifying the volume-specific surface area ($\mathcal{S}_{\forall}$) for a cylindrical ligament, the Kozeny-Carman equation can be reformulated as follows

$$\mathcal{S}_{\forall} = \frac{\mathcal{S}_\mathrm{cylinder}}{\forall_\Omega} = \frac{\mathcal{S}_\mathrm{cylinder}}{\forall_\mathrm{cylinder}/(1-\varepsilon)} = \frac{2\pi r_\mathrm{l} L}{\pi r_\mathrm{l}^2 L/(1-\varepsilon)} = \frac{2(1-\varepsilon)}{r_\mathrm{l}} \Rightarrow$$

$$K = \frac{\varepsilon^3 r_\mathrm{l}^2}{8(1-\varepsilon)^2}. \tag{2.15}$$

Similarly, for a spherical grain, the Kozeny-Carman equation can be expressed as follows

$$\mathcal{S}_{\forall} = \frac{\mathcal{S}_{\text{sphere}}}{\forall_{\Omega}} = \frac{\mathcal{S}_{\text{sphere}}}{\forall_{\text{sphere}}/(1-\varepsilon)} = \frac{4\pi r_{\mathrm{l}}^2}{4\pi r_{\mathrm{l}}^3/(3(1-\varepsilon))} = \frac{3(1-\varepsilon)}{r_{\mathrm{l}}} \Rightarrow$$

$$K = \frac{\varepsilon^3 r_{\mathrm{l}}^2}{18(1-\varepsilon)^2}. \tag{2.16}$$

For a general ligament shape, the Kozeny-Carman equation as a function of porosity (ε) and ligament radius (r_{l}) can be written as

$$K = \frac{\varepsilon^3 r_{\mathrm{l}}^2}{c(1-\varepsilon)^2}, \tag{2.17}$$

where c is an adjustment parameter intended to capture complex pore geometries of real porous structures [8, 24].

2.3 Fluid flow through porous media

For a deeper understanding of fluid behavior in porous media, this section presents the fundamental principles of fluid mechanics as applied to these structures. These principles encompass fluid properties, the application of the Reynolds transport theorem, the relevant conservation laws, capillary-driven flows, and macroscopic wetting models.

2.3.1 Fluid properties

Viscosity

Fluids, which include both liquids and gases, are characterized by the presence of intermolecular forces that are inherently attractive and repulsive in all directions. These cohesive forces within the fluid contribute to its overall cohesion. In addition, they play a critical role in the development of internal friction, a property that ultimately manifests itself as a fluid viscosity [23]. Viscosity quantifies a fluid resistance to flow, essentially its resistance to deformation under applied shear stress. This property dictates the rate of strain experienced by the fluid in response to such stress [25].

Fluids are classified as Newtonian if the viscous stresses generated during flow have a linear relationship with the local strain rate. These stresses are proportional to the product of the dynamic viscosity (μ) and the shear rate, which is mathematically equivalent to the derivative of the velocity component in the shear direction with respect to the displacement in the perpendicular direction (dU/dy). For fluids, viscosity is a thermodynamic property that depends on both temperature and pressure. In general, pressure has a minimal effect on the viscosity of a fluid, while temperature plays a more significant role. Specifically, the dynamic viscosity of liquids decreases with increasing temperature, while the opposite trend is observed for gases [25].

When the temperature of a liquid deviates significantly from room temperature, its viscosity will change accordingly. For example, if a liquid initially at a higher temperature is used to wet a porous membrane, its temperature will gradually decrease to ambient conditions, leading to a corresponding change in viscosity. In this study, the temperature is maintained within a narrow range close to room temperature, minimizing the effect of temperature variations on the viscosity of the fluids.

Surface and interfacial tension

Within the bulk liquid, intermolecular forces act uniformly on the molecules in all directions. However, at the surface of the liquid, these attractive forces are only present from the bulk phase and are absent from the surrounding environment. This asymmetry results in a higher energy state for surface molecules compared to their bulk counterparts. This excess energy associated with surface molecules is referred to as surface energy. In order to achieve a lower energy state, the liquid system inherently seeks to minimize the number of high-energy boundary molecules. Consequently, surface energy acts as a driving force to minimize the surface area of the liquid.

The difference in intermolecular forces between bulk and surface molecules manifests itself as surface tension, a mechanical consequence. Surface tension is defined as the normal force per unit length acting on the surface of the liquid and is mathematically equivalent to surface energy density [26, 27]. Expanding the surface area requires work to overcome these intermolecular forces and transfer molecules from the bulk liquid to the surface. The concept of surface tension, denoted as γ, quantifies the amount of work (ΔW) required to increase the surface area (ΔA) [28]

$$\gamma = \frac{\Delta W}{\Delta A}. \tag{2.18}$$

Interfacial tension occurs at the interface between two immiscible or poorly miscible liquids. This phenomenon is a consequence of the surface free energy present at the interface. Immiscibility occurs due to significant differences in the cohesive forces between the molecules of the two liquids [26]. In essence, surface tension characterizes the property of a liquid at its interface with a gas phase, whereas interfacial tension, in contrast, represents the property exhibited between any two substances.

Surface tension varies considerably from substance to substance and also depends on the temperature of a particular substance. By way of illustration, the surface tension of water at 20 °C is measured to be $0.073\,\mathrm{N\,m^{-1}}$ and that of mercury $0.44\,\mathrm{N\,m^{-1}}$ when exposed to atmospheric air. Generally, the surface tension of a liquid diminishes with increasing temperature. The impact of pressure on surface tension is usually negligible. However, the presence of impurities can significantly alter the surface tension of a substance. Thus, certain chemicals known as surfactants can be added to a liquid to reduce its surface tension. For instance, soaps and detergents are capable of lowering the surface tension of water, allowing it to effectively permeate the narrow spaces between fibers, thereby enhancing the efficiency of cleaning processes [23].

Contact angle

Wettability, a fundamental property of a material system, describes the inherent tendency of a liquid to spread or adhere to a solid surface in the presence of another immiscible fluid. The amount of liquid spreading on the solid surface serves as a key indicator of the wetting behavior between the liquid and the solid.

When placed on a solid substrate, a liquid droplet forms a contact line at the interface between the gas (G), liquid (L), and solid (S) phases, as shown in Figure 2.2b. This contact line establishes an equilibrium contact angle (θ) between the free surface of the liquid and the solid surface. This equilibrium contact angle results from a balance between the cohesive forces within the liquid and the adhesive forces acting at the liquid-solid interface.

The contact angle (θ) formed between the free surface of the liquid and the substrate surface is a key parameter for quantitatively and accurately characterizing the spreading behavior of the liquid on the solid [8, 29]. This angle is significantly influenced by the surface and interfacial energies of the different phases

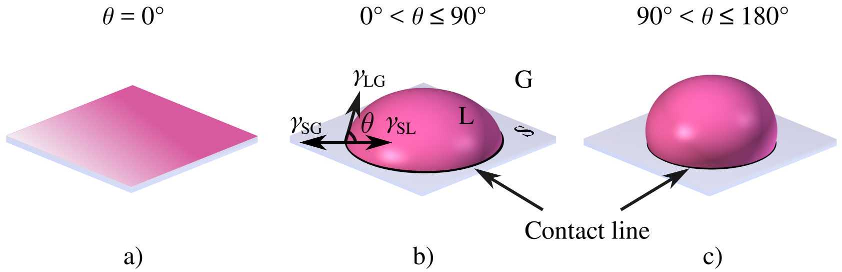

Figure 2.2: Different contact angles are observed at the interface between a liquid (L), a solid substrate (S), and a surrounding gas (G). In (a), $\theta = 0°$ indicates the formation of a thin liquid film spreading over the substrate surface, where the adhesive forces between the liquid and the substrate dominate the cohesion forces within the liquid. In (b), $0° < \theta \leq 90°$ represents the droplet with characteristics associated with strong interaction with the substrate driven by adhesive forces. In (c), $90° < \theta \leq 180°$ shows behavior associated with resistance to the substrate, indicating the predominance of cohesive forces within the liquid.

(liquid, solid, gas) present in the system. When the droplet reaches equilibrium, this relationship is formally described by Young's equation

$$\gamma_{\mathrm{LG}} \cos\theta = \gamma_{\mathrm{SG}} - \gamma_{\mathrm{SL}}, \tag{2.19}$$

where γ_{LG}, γ_{SG}, and γ_{SL} represent the liquid-gas, solid-gas, and solid-liquid surface tension coefficients, respectively. In the context of water wetting, complete wetting, characterized by a contact angle of $\theta = 0°$, means that the water spreads over a large area of the substrate. This scenario results in the formation of a thin liquid film where the adhesive forces between the water molecules and the substrate dominate over the cohesive forces within the water itself. Hydrophilic wetting is associated with contact angles in the range of 0° to 90°. Conversely, surfaces exhibiting hydrophobic behavior are characterized by contact angles between 90° and 180°, as shown in Figure 2.2.

The phenomenon of surface tension arises from a gradient of potential energy experienced by molecules at the surface of a liquid. Due to the inherent tendency of a system to minimize its energy, surface molecules arrange themselves to form minimal surfaces, often manifested as curved interfaces. A mechanical equilibrium analysis of this system reveals a pressure difference across the interface, with a higher pressure on the concave side. This pressure difference is reflected in a pressure jump (Δp) across the interface. For a hemispherical interface, as shown in Figure 2.3a, the pressure increase inside the droplet counterbalances the circumferential surface tension force, expressed by [25]

$$\pi R^2 \Delta p = 2\pi R \gamma_{\mathrm{LG}} \Rightarrow \Delta p = \frac{2\gamma_{\mathrm{LG}}}{R}, \tag{2.20}$$

where R symbolizes the radius of the hemispherical droplet.

In cases where the interface has an arbitrary curved configuration characterized by principal radii of curvature R_1 and R_2, as shown in Figure 2.3b, the magnitude

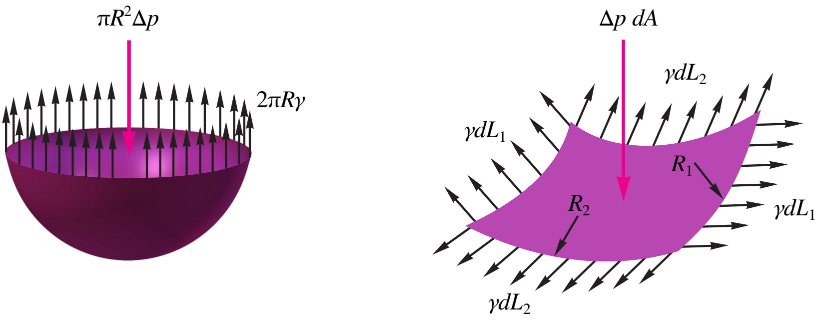

a) b)

Figure 2.3: Schematic representation of the pressure change across a curved interface due to surface tension: a) interior of a spherical droplet; b) general curved interface.

of the pressure jump depends on both the radii and the surface tension. This dependence is described by the general Young-Laplace equation

$$\Delta p = \gamma_{\mathrm{LG}} \left(\frac{1}{R_1} + \frac{1}{R_2} \right) = 2\gamma_{\mathrm{LG}} H, \tag{2.21}$$

where H is the mean curvature, a parameter that quantifies the overall curvature of the gas-liquid interface. It is important to note that Eq. (2.20) can be derived from Eq. (2.21) when $R_1 = R_2 = R$. In addition, the calculations presented here do not take into account the weight of the liquid.

2.3.2 Reynolds transport theorem

In many engineering applications, fluid behavior is described using a continuum framework. This approach ignores the intricate molecular constitution and associated motions of the fluid in favor of the dominant macroscopic motion. The continuum model is considered valid as long as the characteristic length scale of the system significantly exceeds the mean free path of the constituent molecules [23]. This idealization allows fluid properties to be treated as point functions, implying continuous spatial variation without abrupt jumps. Fundamental properties, such as density (ρ), pressure (p), velocity field ($\mathbf{U} =$

$(U,V,W)^{\mathrm{T}}$), and temperature (T), are treated as continuous functions in the domain of continuum mechanics. These functions depend on the spatial vector ($\mathbf{x} = (x,y,z)^{\mathrm{T}}$) and the temporal parameter (t). The governing equations for fluid flow are derived from the fundamental principles of conservation of mass (continuity equation), conservation of momentum (Navier-Stokes equation), and conservation of energy.

The Reynolds transport theorem is used to establish the principles of conservation in a continuum framework. This theorem is applied in the context of a stationary control volume (CV) of arbitrary definition, as illustrated in Figure 2.4. The figure shows a stationary CV through which an arbitrary flow pattern passes. Fluid enters and exits the CV through distinct and variable segments of the control surface (CS). In a general scenario, each infinitesimal area element (dA) on the surface will have a unique velocity (U) that forms a specific angle (α) with the local normal vector to dA ($\mathbf{n}$). Different element areas will have inflow volumes of $d\forall_{\mathrm{in}} = (UA\cos\alpha)_{\mathrm{in}}dt$, while others will have outflow volumes of $d\forall_{\mathrm{out}} = (UA\cos\alpha)_{\mathrm{out}}dt$, where dt is an infinitesimal time increment. For a fluid property denoted as B, its intensive value $\beta = dB/dm$ gives the amount of B per unit mass in infinitesimal fluid elements. The cumulative amount of property B confined within the CV is expressed by $B_{\mathrm{CV}} = \int_{\mathrm{CV}} \beta dm = \int_{\mathrm{CV}} \beta \rho d\forall$ [25].

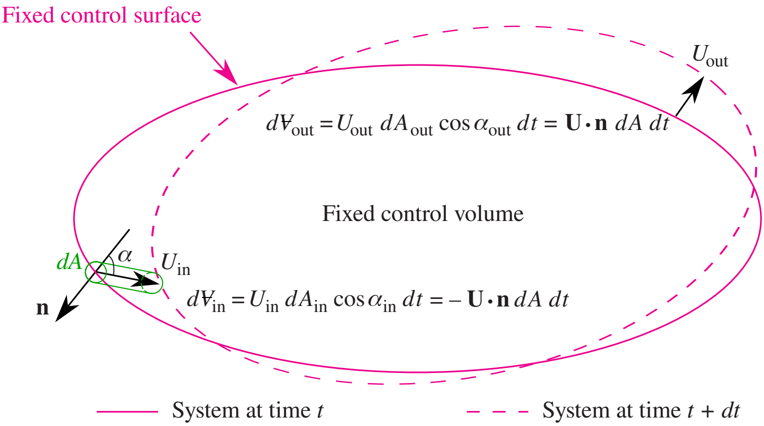

Figure 2.4: An arbitrary control volume with an arbitrary flow pattern.

Thus, there are three basic mechanisms that can cause a change in the amount of property B within the CV:

the change taking place within the CV: $\frac{d}{dt}\int_{\mathrm{CV}} \beta\rho d\forall,$ (2.22a)

the outflow of β from the CV: $\int_{\mathrm{CS}} \beta\rho U \cos\alpha dA_{\mathrm{out}},$ (2.22b)

the inflow of β to the CV: $\int_{\mathrm{CS}} \beta\rho U \cos\alpha dA_{\mathrm{in}}.$ (2.22c)

In the limit, as dt approaches zero, the instantaneous variation of the attribute B in the system is equal to the sum of the variations within the CV, subtracted by the inflow and added by the outflow. This relationship is succinctly encapsulated by the Reynolds transport theorem for a fixed control volume, manifested in [25]

$$\frac{d}{dt}(B_{\mathrm{system}}) = \frac{d}{dt}\int_{\mathrm{CV}} \beta\rho d\forall + \int_{\mathrm{CS}} \beta\rho \mathbf{U}\cdot\mathbf{n}\, dA. \tag{2.23}$$

After using the Leibniz integral rule for the first integral on the right side of Eq. (2.23), together with Gauss's theorem (divergence theorem) for the subsequent integral on the right side, this equation can be reformulated as follows

$$\frac{d}{dt}(B_{\mathrm{system}}) = \int_{\mathrm{CV}} \left[\frac{\partial}{\partial t}(\beta\rho) + \nabla\cdot(\beta\rho\mathbf{U})\right] d\forall. \tag{2.24}$$

By considering the property B as mass (m) in the Reynolds transport equation, the conservation of mass for a CV can be obtained. Similarly, by considering the property B as momentum ($m\mathbf{U}$), the conservation of momentum can be deduced. This study focuses on the wetting of a porous membrane under isothermal conditions. Consequently, the analysis is based on the principles of conservation of mass and momentum, while the conservation of energy is not explicitly considered because the temperature is assumed to be constant.

2.3.3 Conservation of mass

The conservation of mass principle states that the rate of mass increase within a fluid element must be equal to the net rate of mass flow into the element [30]. This fundamental principle, when applied to a closed system undergoing a change, can be derived mathematically using the Reynolds transport theorem, resulting in the continuity equation. By considering the property B as the mass (m), which gives $\beta = 1$, and recognizing that the mass of the system remains constant, which makes its time derivative zero (i.e., $dm_{\text{system}}/dt = 0$), the Reynolds transport equation (Eq. (2.24)) is simplified to [23]

$$0 = \int_{\text{CV}} \left[\frac{\partial \rho}{\partial t} + \nabla \cdot (\rho \mathbf{U}) \right] d\forall. \tag{2.25}$$

Since this condition must hold for any arbitrary control volume, it leads to the differential form of mass conservation

$$0 = \frac{\partial \rho}{\partial t} + \nabla \cdot (\rho \mathbf{U}). \tag{2.26}$$

By expanding the second term on the right-hand side, the continuity equation can be formulated as follows

$$0 = \underbrace{\frac{\partial \rho}{\partial t} + \nabla \rho \cdot \mathbf{U}}_{\frac{d\rho}{dt}} + \rho (\nabla \cdot \mathbf{U}). \tag{2.27}$$

Since the density of an incompressible fluid does not change with time ($d\rho/dt = 0$), the continuity equation leads to a divergence-free velocity field

$$0 = \nabla \cdot \mathbf{U}. \tag{2.28}$$

2.3.4 Conservation of momentum

Newton's second law, also known as the linear momentum equation in fluid mechanics, states that the net force acting on a fluid element is equal to the rate of change of its linear momentum. This is derived from the equation of forces acting on the system material $\mathbf{F} = m\mathbf{a} = d(m\mathbf{U})/dt$, where $\mathbf{a}$ is the acceleration vector and the linear momentum attribute is expressed as $m\mathbf{U}$, which is evaluated with respect to time. As a result, the property of the fluid (B) takes the form $B = m\mathbf{U}$ in the context of the Reynolds transport theorem, and consequently β is defined as $dB/dm = \mathbf{U}$. Thus, the following form can be used to describe the linear momentum equation regarding an immobile control volume

$$\frac{d}{dt}(m\mathbf{U})_{\text{system}} = \sum \mathbf{F} = \frac{d}{dt}\int_{\text{CV}} \mathbf{U}\rho \, d\forall + \int_{\text{CS}} \mathbf{U}\rho(\mathbf{U}\cdot\mathbf{n})\, dA. \tag{2.29}$$

In essence, the equation states that the sum of all external forces acting on a control volume (CV) is equal to the time derivative of the linear momentum of the substances within the CV plus the net momentum flux across the control surface (CS) [25]. In the form of Eq. (2.24), the conservation of momentum is

$$\frac{d}{dt}(m\mathbf{U})_{\text{system}} = \sum \mathbf{F} = \int_{\text{CV}} \left[\frac{\partial}{\partial t}(\mathbf{U}\rho) + \nabla\cdot(\rho\mathbf{U}\mathbf{U})\right] d\forall. \tag{2.30}$$

It is worth noting that within the domain of continuum mechanics, forces acting on a fluid element are typically categorized into two distinct types: body forces and surface forces. Body forces, such as gravity, originate from external fields and act on the entire volume of the fluid element. In contrast, surface forces arise from stresses exerted on the boundaries of the control surface. These stresses encompass both hydrostatic pressure and viscous forces.

The Navier-Stokes equation for incompressible flow with constant viscosity, derived from the momentum conservation equation (Eq. 2.30), describes the relationship between fluid acceleration, pressure gradient, viscous forces, and body forces (e.g., gravity) as follows [23]

$$\rho \frac{d\mathbf{U}}{dt} = -\nabla p + \mu \nabla^2 \mathbf{U} + \rho \mathbf{g}. \tag{2.31}$$

The Navier-Stokes equation provides a mathematical representation of the fundamental principles governing fluid motion. Under conditions of very low flow velocity, high fluid viscosity, or significantly small characteristic geometry size, the convective terms (inertial terms) within the Navier-Stokes equation can be neglected. In such cases, the flow behavior is primarily influenced by pressure, viscous, and volumetric forces. For incompressible fluids, the linearized form of the momentum equation, known as the Stokes equation [8], can be expressed as

$$0 = -\nabla p + \mu \nabla^2 \mathbf{U}. \tag{2.32}$$

This equation describes the creeping flow of a Newtonian fluid, excluding the effects of gravity.

2.3.5 Capillary-driven flows

Since a porous medium is often conceptually viewed as a bundle of dimensionally similar, aligned capillary tubes, the fluid flow in each tube represents fluid movement within the pore space of the porous material. As a result, the basis of the mathematical framework of capillary models is the flow of fluid through a single capillary tube [19]. Selecting the control volume shown in Figure 2.5 and applying the laws of conservation of mass and momentum give the following equation

$$\underbrace{\frac{2\gamma_{\mathrm{LG}} \cos\theta}{r}}_{\text{Capillary}} = \underbrace{\rho \frac{d(l\dot{l})}{dt}}_{\text{Inertia}} + \underbrace{\frac{8\mu l \dot{l}}{r^2}}_{\text{Friction}} + \underbrace{\rho g l}_{\text{Gravity}} . \tag{2.33}$$

The capillary pressure is written based on the Young-Laplace equation (Eq. (2.21)) where $R_1 = R_2 = R$ and $H = 1/R = \cos\theta/r$ with r as the capillary radius shown in Figure 2.5. Friction in a capillary tube can be modeled using the Hagen-Poiseuille equation (see Eq. (2.11)) with dynamic viscosity μ, head rise l, average flow velocity $\dot{l}$, and the square of the capillary radius r^2.

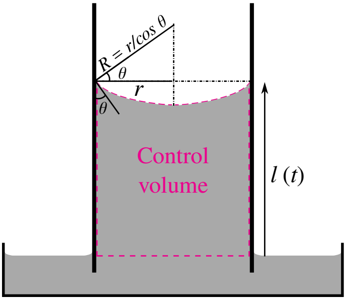

Figure 2.5: Control volume in a capillary tube.

In Eq. (2.33), when the effects of gravity and inertia are ignored, the capillary term is balanced by the viscous (friction) term. Therefore,

$$\frac{2\gamma_{\mathrm{LG}}\cos\theta}{r} = \frac{8\mu l\dot{l}}{r^2} \Rightarrow l\frac{dl}{dt} = \frac{\gamma_{\mathrm{LG}} r\cos\theta}{4\mu}. \tag{2.34}$$

By applying the initial condition $l(t=0) = 0$, this equation can be solved, yielding the well-known Lucas-Washburn equation in the following form

$$l(t) = \sqrt{\frac{\gamma_{\mathrm{LG}} r\cos\theta}{2\mu}} \cdot t^{1/2}. \tag{2.35}$$

Equation (2.34) allows for the derivation of a key dimensionless parameter, the capillary number

$$Ca = \frac{\mu\dot{l}}{\gamma_{\mathrm{LG}}} \tag{2.36}$$

The capillary number is a dimensionless quantity that represents the ratio of viscous forces to surface tension forces acting on a fluid within a capillary tube. When the capillary number is small, the flow regime can be classified as capillary-driven, indicating the dominance of surface tension forces over viscous forces.

When the effects of both gravity and friction on liquid spreading are considered, Eq. (2.33) can be condensed as follows

$$\frac{2\gamma_{\mathrm{LG}}\cos\theta}{r} = \frac{8\mu l\dot{l}}{r^2} + \rho g l. \tag{2.37}$$

A thorough analytical solution to Eq. (2.37) was introduced by Fries [31], expressed in the form $l(t)$ with a Lambert function W. The solution is as follows

$$l(t) = \frac{1}{\chi}\left[1 + W\left(-e^{-1-\frac{\chi^2 t}{\xi}}\right)\right], \tag{2.38}$$

with

$$\chi = \frac{\rho g r}{2\gamma_{\mathrm{LG}}\cos\theta} \text{ and } \xi = \frac{4\mu}{r\gamma_{\mathrm{LG}}\cos\theta}. \tag{2.39}$$

Finally, the equilibrium height at which the hydrostatic pressure equals the capillary pressure is calculated as follows

$$l_{\mathrm{eq}} = \frac{2\gamma_{\mathrm{LG}}\cos\theta}{\rho g r} = \frac{1}{\chi}. \tag{2.40}$$

2.3.6 Capillary-driven flows in porous media

At low capillary numbers, capillary forces govern fluid flow within porous media. Effective capillary pressure plays a crucial role in dictating fluid flow through porous structures. This pressure is influenced by the wetting conditions, which include surface tension and contact angle, as well as by the intricate geometry that characterizes the pore space. In an attempt to describe this phenomenon, the Young-Laplace equation (Eq. (2.21)) is used with the basic premise that the porous structures can be conceptually approximated as an array of parallel cylindrical capillaries. While determining the radius (r) for a single capillary is a straightforward process, this task becomes significantly more challenging for complex porous membranes. Consequently, the term “effective” capillary radius (r_{eff}) is introduced.

A primary challenge associated with using the Young-Laplace equation to model capillary pressure in porous media is the determination of the effective capillary radius [32, 33]. This difficulty arises because the pore space is typically highly complex and can only be inaccurately approximated by simple geometries such as cylinders. As a result, the assumptions underlying the Young-Laplace equation may initially lose their validity, or the ability to predict wetting processes may become inaccurate. To address these limitations, researchers have explored various methods, including macroscopic experimental techniques and microscopic analytical approaches [8]. Wetting experiments are a prominent approach for determining the effective capillary radius. An alternative strategy involves the use of micro-scale computational methods to analyze the geometric properties of pore spaces (see section 3.1.3).

In general, the use of the capillary model in porous media can be realized by drawing an analogy with a single capillary tube, as exemplified by Eq. (2.13). By leveraging this analogy, Eq. (2.33) can be reformulated to apply to porous media as follows

$$\frac{2\gamma_{\text{LG}}\cos\theta}{r_{\text{eff}}} = \rho\frac{d(l\dot{l})}{dt} + \frac{\varepsilon\mu l\dot{l}}{K} + \rho g l, \tag{2.41}$$

where r_{eff} is the effective pore radius, ε the porosity, and K the permeability. In scenarios dominated by viscous effects, with negligible gravitational and inertial contributions, Eq. (2.41) is thus modified to [34]

$$\frac{2\gamma_{\text{LG}}\cos\theta}{r_{\text{eff}}} = \frac{\varepsilon\mu l\dot{l}}{K}. \tag{2.42}$$

Given an initial condition of $l(t=0)=0$, this simplified equation leads to the following expression for the liquid-front height as a function of time

$$l(t) = \sqrt{\frac{4K\gamma_{\mathrm{LG}}\cos\theta}{\mu\varepsilon r_{\mathrm{eff}}}} \cdot t^{1/2}. \tag{2.43}$$

When both viscous and gravitational effects are important, the capillary model for porous media based on Eq. (2.41) can be expressed as

$$\frac{2\gamma_{\mathrm{LG}}\cos\theta}{r_{\mathrm{eff}}} = \frac{\varepsilon\mu l\dot{l}}{K} + \rho g l. \tag{2.44}$$

The solution to this equation is similar to that of Eq. (2.37), but with specific adjustments to account for the consideration of effective parameters

$$l(t) = \frac{1}{\chi_{\mathrm{eff}}}\left[1 + W\left(-e^{-1-\frac{\chi_{\mathrm{eff}}^2 t}{\xi_{\mathrm{eff}}}}\right)\right], \tag{2.45}$$

with

$$\chi_{\mathrm{eff}} = \frac{\rho g r_{\mathrm{eff}}}{2\gamma_{\mathrm{LG}}\cos\theta} \text{ and } \xi_{\mathrm{eff}} = \frac{\mu}{2\gamma_{\mathrm{LG}}\cos\theta}\frac{\varepsilon r_{\mathrm{eff}}}{K}. \tag{2.46}$$

Using these effective coefficients, the velocity of the liquid front can be expressed as

$$\dot{l}(t) = \frac{1}{\xi_{\mathrm{eff}}}\frac{1}{l} - \frac{\chi_{\mathrm{eff}}}{\xi_{\mathrm{eff}}}. \tag{2.47}$$

2.3.7 Macroscopic wicking models

Wicking, also known as spontaneous imbibition, is the process by which a liquid is drawn into a porous medium due to the negative capillary pressure at the liquid-gas interface [19]. A thorough review of macroscopic models for wetting in paper-like materials is provided by Liu et al. [35]. It is important to clarify that the term “macroscopic” in this context refers to the scale of the entire porous structure, not the size of the individual pores (see section 2.4.6). This section presents a concise overview of two established macroscopic methods for investigating wicking in rigid, open-cell porous media, along with some adaptations of these techniques reported in the literature [36].

Bell-Cameron-Lucas-Washburn wicking model (Lucas-Washburn wicking model)

The first method for studying wicking in rigid porous media leverages the Hagen-Poiseuille equation (Eq. (2.10)). This approach simplifies the pore space by conceptualizing it as a collection of parallel, cylindrical capillary tubes aligned with the flow direction, as described by Zarandi et al. [37]. Pioneering studies by Bell and Cameron [38], Lucas [39], and Washburn [40] independently analyzed liquid movement through vertical cylindrical tubes, considering liquid wetting on the tube walls. Collectively, these investigations established that the wicking length is proportional to the square root of the wicking time, a relationship known as the Bell-Cameron-Lucas-Washburn (BCLW) imbibition law or, more commonly, the Lucas-Washburn (LW) model (Eq. (2.35)).

It is important to recognize that real porous media often deviate significantly from the idealized model of a bundle of uniform circular tubes. In reality, pore structures can be non-circular, tortuous, and even intricate. As a result, the applicability of the Hagen-Poiseuille equation, and consequently the LW equation, to the study of wicking in most porous materials is limited. This limitation has led researchers to question the validity of the LW model for complex geometries. For instance, Berthier et al. [41] investigated confined porous media with non-circular but uniform cross-sections and proposed a modified prefactor for the LW model. Cai et al. [42] explored the influence of tortuosity in conjunction with capillary tubes of different shapes. Studies on periodically constricted tubes, including sinusoidal tubes, have been documented in the literature [43–45]. In addition, Reyssat et al. [46] conducted combined experimental and theoretical studies that revealed deviations from the LW model for geometries with axial variations. Their findings suggest that for such geometries, the LW model remains applicable only for short times, while for longer times, the wicking length becomes proportional to the fourth root of the wicking time.

The LW model is primarily used to describe capillary-driven liquid flow in porous media with non-expanding geometries. For expanding porous materials, alternative theoretical frameworks based on potential flow theory have been proposed for both two- and three-dimensional configurations, as documented in [47]. The well-established LW law captures the equilibrium between surface tension and viscosity, neglecting fluid inertia and gravitational effects. However, the model proposed by Liou et al. [48] incorporates all four factors in the context of capillary rise in axisymmetric tubes. Moreover, the LW model does not account for flow effects at the meniscus, a phenomenon investigated by Mehrabian et al. [49] using finite element method simulations to capture the interface behavior accurately. For a comprehensive overview of recent advances in mathematical modeling and numerical investigations related to the LW equation, including its adaptations and extensions for various microchannels and porous media, readers are referred to the review article by Cai et al. [50].

Darcy-based wicking model

The second approach to the study of wicking in rigid porous media centers on the application of Darcy's law (Eq. (2.7)). This law establishes a relationship between the superficial flow velocity and the pressure gradient for a viscous Newtonian fluid operating at low speeds, as documented in works such as those of [51, 52]. In their work, Masoodi et al. [34] used different formulations for the suction pressure within Darcy's law to simulate liquid absorption in polymer wicks. This approach led to the development of two distinct models. The first, known as the capillary model, incorporates capillary pressure as the suction pressure term (see Eq. (2.42)). The second, known as the energy balance model, reflects the equilibrium between surface free energy and viscous dissipation energy. By including the influence of gravity, the authors further developed two additional variations of these models. Their investigations revealed that the most satisfactory results were obtained from the energy balance model when the effects of gravity were taken into account.

2.4 Lateral flow assays (LFAs)

This thesis investigates capillary-driven fluid flow through porous membranes, specifically in the context of lateral flow assays (LFAs) used in medical applications. This section provides a detailed technical overview of the operating principles of LFAs.

In the medical field, rapid diagnostic tests (RDTs) are often deemed essential in emergencies or healthcare settings with limited resources. One prevalent type of RDTs is the lateral flow assay, which operates on the basis of antigen detection [53]. The simplicity, portability, rapid turnaround time, and high sensitivity of LFAs make them a valuable tool for point-of-care testing (POCT). Therefore, LFA is a widely adopted technology these days and is commonly used to diagnose a range of conditions, including pregnancy, cancers, and infectious diseases such as COVID-19. Posthuma-Trumpie et al. [54] conducted a literature survey that investigated the strengths, weaknesses, opportunities, and threats (SWOT) associated with LFAs.

2.4.1 LFAs principle

The LFA consists of four primary components [55]: i) a sample pad, ii) a conjugate pad, iii) a cellulose nitrate (CN) membrane, which houses a printed test line (TL) and control line (CL), and iv) an absorbent pad. All four components consist of porous media that are sequentially overlapped and bonded together to facilitate capillary-driven transport of sample fluid through the test strip. In addition, a carrier board (backing card) is commonly used to mount these components, simplifying manufacturing and handling while enhancing mechanical stability. Figure 2.6 depicts a schematic of a non-competitive sandwich LFA.

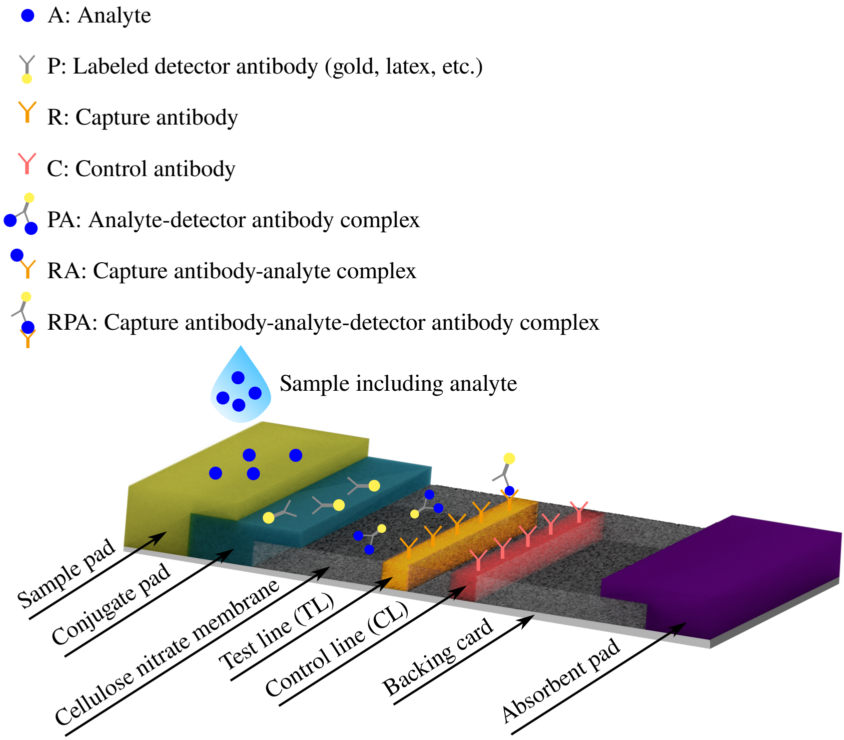

Figure 2.6: Schematic layout of a lateral flow assay in a non-competitive sandwich format.

The analysis of fluid samples, such as urine, serum, or saliva, targets a specific antigen, called the analyte (A), in the sample. The sample is applied to a sample pad, which then facilitates its migration to the conjugate pad. The conjugate pad houses labeled detector antibodies (P), which typically comprise colored particles such as gold or latex. This component is often regarded as the most expensive element of many LFAs.

These detector antibodies (P) bind specifically to the analyte (A), forming an analyte-detector antibody complex (PA). This complex migrates through the cellulose nitrate membrane, a highly porous material that serves as a transport pathway for the sample fluid. The complex can then bind to the immobilized capture antibodies (R) located on the test line (TL) or the control probe (C) on the control line (CL) of the membrane.

The establishment of a positive test result, characterized by a color signal in a lateral flow assay, is dependent on the accumulation of the capture antibody-analyte-detector antibody (RPA) complex on the TL. The control line, on the other hand, is used to confirm the test's reliability through the binding of the control line antibody with a control biomolecule that is always present in the sample fluid. Regardless of whether the target analyte is present in the sample, the control line must always show a color signal to ensure that the test has been performed correctly. Upon reaching the terminus of the test strip, the sample fluid is drawn into an absorbent pad. The absorbent pad acts as a reservoir for excess reagents. The inclusion of an absorbent pad allows for increased sample volume and potentially improved sensitivity. Conversely, without an absorbent pad, premature flow stoppage may occur when the fluid front reaches the end of the membrane [54].

The test result is determined by the accumulation of colored immunoconjugates on the TL and CL, which is influenced not only by the binding affinity of the reactants but also by the flow rate of the sample [56]. The latter is attributed to negative capillary pressure, which relies on the interfacial tension between the wetting and non-wetting phases (sample fluid and air) and the mean curvature of each individual pore [57, 58].

2.4.2 Diagnostic membrane

The porous cellulose nitrate (CN) membrane, incorporating surfactants, is a critical component of an LFA due to its exceptional binding capacity [7]. Its open-cell structure, characterized by high porosity, facilitates capillary-driven fluid flow through the membrane. As a result, porous membranes are often studied in terms of capillary flow dynamics. Manufacturers typically evaluate the wicking time, defined as the time required for complete wetting of a given membrane segment with a particular wetting liquid, usually water. Table 2.1 presents the main characteristics of two commercially available CN membranes provided by *Sartorius Stedim Biotech GmbH*, with a membrane length of 4 cm and water as the wicking liquid.

Table 2.1: Properties of commercially available CN membranes from *Sartorius* [59].

Membrane	Porosity (%)	Pore size (μm)	Capillary rise time (s/4 cm)
CN 95	82.0	15	87±2
CN 140	80.4	10	136±2

2.4.3 Characteristic timescales

In an LFA, the analyte moves across the membrane in a series of steps driven by capillary flow (convection) and then diffuses into the capture zones (diffusion) where molecular interactions lead to complex formation (reaction). By examining their distinct timescales, it is possible to assess the relative importance of each of these processes [56]:

1. **Convection**: The residence time ($t_{\mathfrak{R}}$) is formulated as $t_{\mathfrak{R}} = \mathscr{W}_{\mathrm{TL}}/U_{\mathrm{TL}}$, where $\mathscr{W}_{\mathrm{TL}}$ represents the width of the test line (TL), and U_{TL} the wicking velocity specifically within the TL. While the wicking velocity (U) exhibits a decreasing trend along the length of the membrane, it is reasonable to approximate the wicking velocity within the TL (U_{TL}) as constant. This assumption is grounded in the substantial difference between the TL width and the TL position (X_{TL}), as expressed mathematically by $\mathscr{W}_{\mathrm{TL}} \ll X_{\mathrm{TL}}$ (see Figure 2.7a).

2. **Diffusion**: The diffusion time is quantified by the equation $t_\mathrm{D} = d_\mathrm{p}^2/D$, where d_p is the mean pore size of the membrane and D is the molecular diffusion coefficient.
3. **Reaction**: The characteristic kinetic time, denoted as $t_\mathcal{K}$, is given by the expression $t_\mathcal{K} = 1/(k_\mathrm{B} \cdot C_\mathrm{initial})$, where k_B is the binding constant and C_initial is the concentration of the analyte.

By calculating the timescales of these three phenomena and comparing them, a time interval is determined in which all of them can occur. This is done using the LFA parameters from Table 2.2.

Table 2.2: Parameter values for calculating timescales in LFAs [36].

Parameter	Description	Value
$\mathscr{W}_\mathrm{TL}$	Width of the test line (TL)	1 mm [56]
U_TL	Wicking velocity at the TL	0.1–$0.5\,\mathrm{mm\,s^{-1}}$ [60]
d_P	Mean pore diameter	$3.74\,\mathrm{\mu m}$ [61]
D	Diffusion coefficient	20–$2000\,\mathrm{\mu m\,s^{-2}}$ [62]
k_B	Forward reaction rate	10^4–$10^7\mathrm{M^{-1}\,s^{-1}}$ [60]
C_initial	Initial concentration	0.5–$50\,\mathrm{nM}$ [63]

The obtained results show that the diffusion time ($0.007\,\mathrm{s} \leq t_\mathrm{D} \leq 0.7\,\mathrm{s}$) is significantly shorter than both the residence time ($2\,\mathrm{s} \leq t_\mathcal{R} \leq 10\,\mathrm{s}$) and the kinetic time ($2\,\mathrm{s} \leq t_\mathcal{K} \leq 2 \times 10^5$ s). This observation emphasizes the significantly faster molecular diffusion compared to convection and reaction processes. Consequently, when defining a design range, it becomes paramount to pay attention to the factors governing the convection and reaction kinetics. The design range is therefore the intersection of the residence time as a function of the wicking velocity through the test line (TL) and the characteristic kinetic time as a function of the analyte concentration. The design range is from 2 to 10 seconds [36] and corresponds to the interval given in Table 2.2 for U_TL and C_initial with a binding affinity of $k_\mathrm{B} = 10^7\ \mathrm{M^{-1}\,s^{-1}}$.

2.4.4 Wetting behavior

The contact angle, formed at the interface between a liquid and the intrinsic surface of a porous material, is a crucial property for understanding liquid-solid interactions. Within the range of 0° to 90°, spontaneous wetting and subsequent liquid transport within the porous medium occur.

Cellulose nitrate (CN) is inherently hydrophobic, resulting in hydrophobic behavior of CN membranes when in contact with aqueous solutions [64]. This causes the CN membranes to exhibit a larger contact angle and repel water. To overcome this problem, surfactants are added to alter the wetting behavior of CN membranes. This changes the hydrophobic properties of the CN membranes and gives them hydrophilic wetting properties. Contact angles become smaller as the surfactant concentration increases, indicating better surface wetting [65]. At the same time, the surface tension is reduced by the use of surfactants. This decrease in surface tension can counteract the increase in capillary pressure caused by the reduced contact angles [8].

2.4.5 Test strip profiles

As explained in section 2.4.1, in LFAs, chemical reactions take place between sample components and antibodies within the TL/CL, resulting in the formation of complexes. This depends on the flow velocity being in a range that is conducive to these chemical reactions occurring in a reasonable time frame. If the flow velocity exceeds this range, the chemical reactions do not occur, resulting in the absence of a color signal in the LFA. In other words, the LFA loses its validity. Conversely, if the flow velocity falls below this range, the appearance of the color signal can be observed, although it may be significantly delayed or prolonged. Ideally, the desired result is the prompt appearance of a color signal with discernible sharpness. Therefore, great care must be taken to control the flow rate.

Capillary-driven flow velocity within porous membranes can be influenced not only by the morphological characteristics of the porous structure, fluid properties, and contact angle [66] but also by the layout of the test strip itself. The latter means that the regulation/control of capillary flow can be achieved by tuning the architectural design, or more precisely, by geometric tailoring [67]. As indicated by Eq. (2.47), the flow velocity within the test region can be varied by adjusting the distance between the conjugate pad and the test line (X_{TL} in Figure 2.7a). Furthermore, the variation in the cross-sectional area of the test strip along the direction of propagation facilitates control of the volume flow directed to the TL [68]. Figure 2.7b shows a multi-segment membrane with a barbell configuration, where an enlargement of the cross-sectional area leads to a decrease in flow velocity. The wicking velocity can also be regulated by adjusting the width of the inlet channels in Figure 2.7c, which presents a multi-branch LFA designed to perform multiple tests on a single sample.

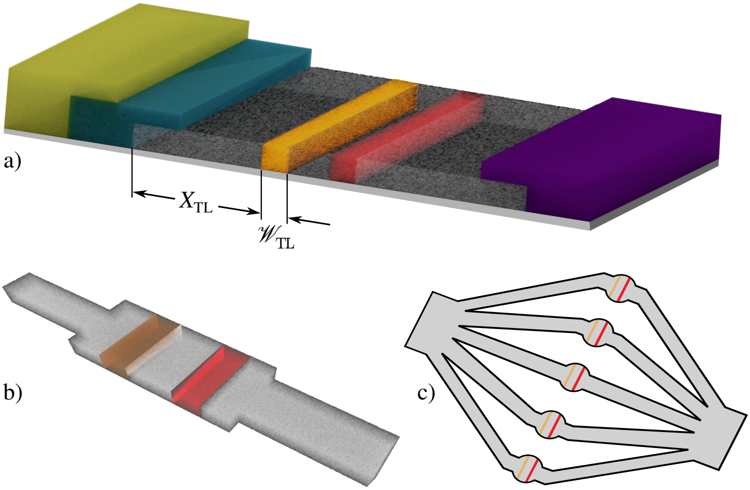

Figure 2.7: Various configurations of LFAs have been developed to control flow velocity by a) manipulating the distance between the conjugate pad and the test line; b) adjusting the cross-sectional area; and c) modifying the channel dimensions within a multi-branch LFA designed for multiplexed testing.

2.4.6 Relevant length scales

The generation of a test signal in lateral flow assays (LFAs) requires the consideration of multiple length scales. This dissertation delves into two specific length scales that are critical to LFA studies: the pore scale, referred to as the micro-scale, and the application scale, which is akin to the macro-scale. This distinction is illustrated in Figure 2.8.

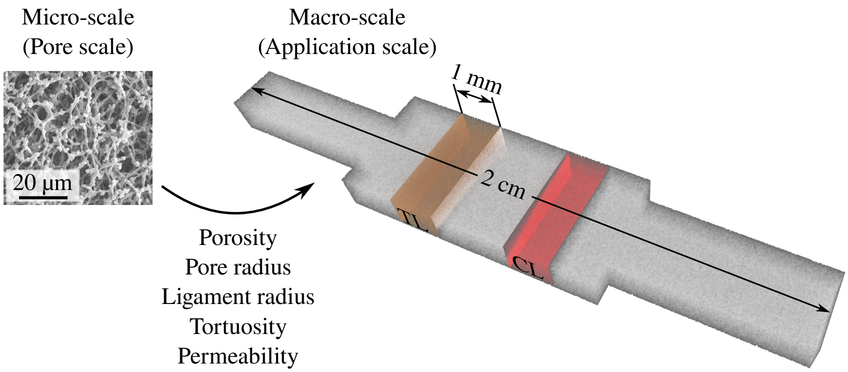

Figure 2.8: The in-depth knowledge gained from the micro-scale investigation is applied to macro-scale modeling.

At the pore scale, the dimensions are of the same order of magnitude as the diameter of individual pores. Accurate measurement of these dimensions requires advanced instrumentation, such as high-resolution microscopes, and sophisticated experimental techniques. It is noteworthy that the nominal pore size of CN membranes exhibits variability in the range of 3 to 20 µm [64]. In contrast, the application scale includes dimensions that are readily quantifiable, including parameters such as the typical width of test or control lines ($1\,\mathrm{mm} \leq \mathscr{W}_{\mathrm{TL}} \leq 2\,\mathrm{mm}$), as well as the separation distance between the conjugate pad and the test line ($2\,\mathrm{cm} \leq X_{\mathrm{TL}} \leq 3\,\mathrm{cm}$). The interface between the micro- and macro-scales is essentially defined by the thickness of the membrane, which typically ranges from 100 to 150 µm for CN membranes [8].

Chapter 3 presents an in-depth investigation of porous membrane structures at the micro-scale. The insights gained from this micro-scale analysis are subsequently utilized for macro-scale modeling purposes in chapters 4 and 5. A key step in bridging the gap between the intricate micro-scale and the broader macro-scale is the homogenization of microstructural heterogeneities.

Homogenization

Homogenization essentially involves the process of simplifying the intricate microstructure and transforming it into an equivalent continuous medium at the macro-scale. This simplification is achieved by treating the heterogeneities as almost negligible compared to the larger-scale phenomena of interest. Consequently, the material can be effectively represented as a uniform and continuous medium at the macroscopic level [69].

Homogenization, a technique used to bridge the micro- and macro-scales in systems with multi-scale properties, can be broadly classified into analytical and numerical approaches. Analytical homogenization employs an asymptotic series expansion to approximate the partial differential equations governing the continuum mechanical problem. This expansion captures the behavior of the material at both micro- and macro-scales, leveraging their differences in length scales. Numerical homogenization, on the other hand, directly models the microstructure and numerically solves the corresponding partial differential equations at the micro-scale. The resulting information is then transferred to the macro-scale study [70].

Homogenization, a field dedicated to bridging micro- and macro-scales in multiscale systems, employs various methods, including concurrent and hierarchical approaches. Concurrent methods focus on the simultaneous solution of equations at both micro- and macro-scales. These approaches often use iterative or multiscale modeling techniques to exchange information between these scales until a consistent solution is obtained. In contrast, hierarchical methods address multiple levels of scales and interactions within a system by constructing a hierarchy of models that articulate behavior at each scale. A notable hierarchical approach is known as the “bottom-up” approach, which initiates the modeling process at the micro-scale and aggregates information to derive macro-scale properties. Effective material properties are typically determined by homogenization methods in order to reduce the computational cost of all relevant scales. Consequently, the main motivation for the application of hierarchical methods is the minimization of the required numerical computations [8].

An example of homogenization is the conceptualization of the pore space as a network of capillary tubes, which allows the study of capillary-driven flows in porous media, as discussed in section 2.3.7, leading to the development of the Lucas-Washburn wicking model [71]. In the study of capillary-driven flows in CN membranes, a distinction is made between the microscopic (pore) scale and the macroscopic scale. To bridge the scale gap, a well-defined section of the microstructure called representative volume element (RVE) is employed. By performing meticulous microstructure simulations and conducting volume averaging over the RVE, effective parameters can be determined with statistical significance.

Representative volume element

The RVE is defined as the smallest volume (VE) element within which the average mechanical or physical properties are representative of the entire structure. In porous membranes, heterogeneities are often distributed over substantial volumes. Therefore, the RVE must include these heterogeneities to ensure statistical homogeneity [72]. Additionally, the RVE should be significantly smaller than the overall structure to maintain scale separation. This leads to two scenarios where the RVE is well-defined: i) Periodic boundary conditions: If the microstructure exhibits a periodic arrangement, the RVE can be defined as a single unit cell of the repeating pattern. This simplifies the analysis by assuming that the properties of the RVE are representative of the entire structure. ii) Extensive information: In cases where detailed information about the microstructure is available, the RVE can be defined as a volume that captures the essential features and heterogeneities of the material. This approach requires a careful selection of the RVE size and shape to ensure that it accurately represents the entire structure.

To determine the RVE, macroscopic properties such as porosity, tortuosity, and permeability are evaluated over expanding volume elements. As the volume element size increases from micro-scale ($\mathcal{O}(L_{\text{micro}})$) to macro-scale ($\mathcal{O}(L_{\text{macro}})$), the observed properties exhibit a transition from oscillatory behavior to consistent values, as shown in Figure 2.9. When the VE size falls within the range of ($\mathcal{O}(L_{\text{micro}})$) to ($\mathcal{O}(L_{\text{macro}})$), the properties converge to represent the effective macro-scale properties, confirming the identification of the RVE. This indicates that the collected data progressively approaches the effective properties of the entire structure.

It is noteworthy that multiple RVEs are present, each tailored to the specific properties under investigation [8]. By identifying all the desired RVEs, the transition

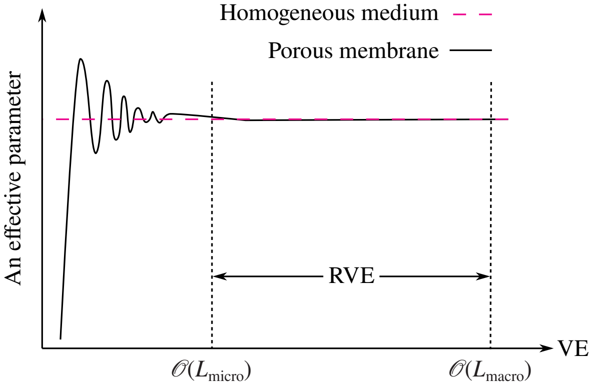

Figure 2.9: Qualitative evolution of an effective property as a function of volume element (VE) size. The choice of representative volume element (RVE) size can be made in the range between micro-scale ($\mathcal{O}(L_{\text{micro}})$) and macro-scale ($\mathcal{O}(L_{\text{macro}})$). Selecting an appropriate RVE size requires a delicate balance between computational efficiency and accurate representation of the microstructure.

from the micro-scale to the macro-scale, known as homogenization, becomes feasible. This transition is primarily based on the volume averaging method [73, 74], complemented by the principles of the theory of mixtures [75].

Chapter 3 includes a thorough microstructural analysis using computer simulations, while chapter 5 is devoted to the macro-scale study of two-phase flow using computer-aided numerical simulations. These investigations require a comprehensive elucidation of the fundamental principles relevant to the field.

2.4.7 Sensitivity enhancement

Lateral flow assays (LFAs) are valuable tools in medical and environmental contexts, particularly in resource-limited settings, due to their rapid turnaround time, cost-effectiveness, and several other advantages. While historically limited in sensitivity compared to traditional laboratory-based assays, recent research has demonstrated significant potential for improvement without compromising the benefits of LFAs [7]. However, the development of LFAs presents challenges that span both engineering and biochemical aspects, as comprehensively reviewed by Kasetsirikul et al. [6]. The following summary outlines some key challenges identified in their study.

Engineering challenges relate to both material and fabrication as well as flow characteristics. Material and fabrication issues include batch-to-batch variation, which refers to differences or inconsistencies observed between different batches of a product or material, particularly when produced in separate fabrication runs. In the context of LFAs, batch-to-batch variation in paper-based materials means potential differences in the physical properties of the paper, including surface area, pore size distribution, porosity, permeability, and wettability, between different production batches. These variations can significantly impact the performance and reproducibility of devices or assays that rely on consistent material properties. Furthermore, environmental factors such as humidity and temperature affect the quality of LFA products. This is due to the fragility and limited shelf life of the CN membrane, which makes it susceptible to environmental variations. Consequently, these variations pose a risk of invalidating strip test results [76]. Another engineering challenge relates to flow characteristics, where capillary flow rates vary between different substrates, affecting sensitivity and overall assay performance. Moreover, Backflow can also occur if no absorbent pad exists or if the paper contains a defect, resulting in a false positive signal. Consideration of these factors, along with the robustness of LFA devices, becomes imperative [6].

In addition to engineering challenges, the development of LFAs faces biochemical challenges. A major biochemical concern is the widespread use of colloidal gold nanoparticle-based reagents and markers in LFAs, although the inherent sensitivity of this type of LFA is limited. This necessitates the exploration of alternative markers with the potential to enhance analyte capture and/or amplify the color signal. Another biochemical challenge is related to the pretreatment of fluid samples. Using raw biological samples, such as blood, urine, and saliva, without a pretreatment step can significantly impact LFA performance due to the presence of complex compounds or other elements. These elements can cause chemical interference with biorecognition events on the conjugate pad or test line, leading to the occurrence of false negatives [77]. To mitigate this, it is recommended to filter out unnecessary elements before loading samples into LFAs. Furthermore, high concentrations of analytes in liquid samples can result in false negatives or underestimation of concentration, a phenomenon commonly referred to as the "hook effect". This decrease in assay line intensity is attributed to excessively high concentrations of a single antigen saturating both capture and detector antibodies simultaneously, preventing proper signal development [63, 78]. Other biochemical challenges include multiplexed detection, where multiple analytes must be identified for accurate disease diagnosis. Finally, readout challenges arise in the transition from qualitative to quantitative assays, requiring the use of tools for accurate signal assessment. Proposed solutions include smartphone-based approaches, but considerations also extend to factors such as image quality, reagent stability, and the development of luminescent labels [6].

The importance of addressing the inherent trade-offs and challenges associated with sensitivity enhancement strategies in LFAs was highlighted by Bishop et al. in [7]. Innovative strategies to address some of these challenges have been elucidated by considering the integrated chemical, physical, and optical properties of LFAs. A structured framework for systematically improving LFA sensitivity has been provided in [7] by categorizing enhancement approaches into three main principles: reaction, transport, and signal.

The reaction principle focuses on improving analyte-reagent interactions, with strategies such as the use of high-affinity capture and detection reagents, both natural and synthetic. However, there are challenges associated with the limited availability and scalability of high-affinity reagents. Within the transport category, methods are available to optimize the movement of samples, buffers, and reagents within LFA strips. Techniques involving modified pad geometries and flow rate adjustments can be used to increase sensitivity. Nevertheless, increased complexity in transport systems may result in trade-offs, such as longer assay times. It is worth noting that reaction and transport are inextricably linked, as changes in transport characteristics such as volume or flow rate inevitably lead to changes in reaction kinetics. Other examples of interrelated improvements that combine aspects of reaction, transport, and signal enhancement include electrophoretic methods for selective analyte transport and aqueous two-phase systems for concentration [7].

While advances in reaction kinetics, transport dynamics, and signal amplification hold promise for increasing sensitivity, they are often accompanied by complexities and limitations. Critical to ensuring the viability and adoption of improved LFA in real-world settings is the balance between sensitivity improvements and practical considerations such as assay time, cost, and ease of use [7].

2.5 Computational fluid dynamics

Empirical observations of the physical world serve as the foundation for developing theoretical models, which are then translated into mathematical equations that describe natural phenomena over various spatial and temporal scales. These equations are then discretized, limiting their scope to a finite set of points, and subjected to approximation.

Advances in computer technology have empowered researchers to conduct numerous numerical experiments with enhanced accuracy and cost-effectiveness. By making simple adjustments to computer programs, researchers can avoid the costly modifications required for experimental equipment. However, numerical simulations demand significant computational resources, particularly when simulating time-dependent processes in three dimensions. In addition to the accuracy and solvability of the mathematical model, computational efficiency is a critical consideration in the field of numerical simulations [79].

An influential area of application for numerical simulation is the study of fluid flow phenomena, facilitated by the computational fluid dynamics (CFD) framework. This methodology allows the simulation of a wide range of scenarios, including aerodynamic, hydrodynamic, capillary-driven fluid flows, and power plant applications. CFD has revolutionized the analysis of fluid systems, leading to significant advancements in various fields. Recent advances in computer technology have made CFD more accessible to a wider range of industries, such as the biomedical industry, and have accelerated its integration into computer-aided engineering tools [30]. The three core components of CFD analysis are pre-processing, processing, and post-processing, which are discussed below.

2.5.1 Pre-processing

The initial phase of CFD simulation is pre-processing, which involves: i) defining the region of interest, called the computational domain; ii) dividing the domain into smaller, non-overlapping subdomains, thereby forming a mesh of cells; iii) selecting the physical and chemical phenomena to be modeled; iv) defining the fluid properties; v) specifying initial conditions for all relevant variables within the computational domain; and vi) specifying appropriate boundary conditions on cells that coincide with or border the domain boundary [30].

Meshing

The accuracy of CFD simulations in determining fluid parameters such as velocity and pressure fields is significantly influenced by the number of grid cells. While a denser grid generally results in higher accuracy, it also requires more computational resources. To balance accuracy and computational cost, non-uniform grids are often employed, with finer meshes in regions of significant variation and coarser meshes in areas of minimal change.

CFD users must carefully consider the trade-off between accuracy and computational cost when designing a mesh [30]. There are two primary types of meshes: structured and unstructured. Structured meshes feature regular cell geometries and point placement, while unstructured grids offer more flexibility in adapting to complex geometries.

When solving the Navier-Stokes equation, it is common to discretize the domain using a “staggered grid”, where the different unknown variables are not located at identical grid points. The pressure (p) is located at the cell centers, the horizontal velocity (u) at the midpoints of the vertical cell edges, and the vertical velocity (v) at the midpoints of the horizontal cell edges. This approach helps to avoid non-physical oscillations in the pressure field [79].

Boundary conditions

To solve the system of equations, specifications for velocity and pressure must be defined as boundary conditions. The Dirichlet boundary condition, as the first type of boundary condition (BC), dictates the values of the solution along the domain boundary. One common example is the no-slip boundary condition, where the fluid remains stationary at the boundary, such as on substrate surfaces. In other words, the no-slip BC dictates that the flow velocity is zero. Another prominent example is the inflow condition, which specifies the values of the velocity components.

The Neumann BC, identified as the second type of BC, prescribes the derivatives of the flow variables. For instance, the outflow condition is applied at the domain boundary to adjust the velocity and maintain divergence-free conditions. This ensures that neither velocity component changes in the direction normal to the boundary [79].

Another type of boundary condition is the free-slip boundary condition, which allows the fluid to move tangentially along a wall without friction while preventing normal penetration. This condition maintains a zero derivative of the tangential velocity and a zero normal velocity at the boundary.

In scenarios such as flow over an undulating surface, periodic boundary conditions can be applied. With periodic boundary conditions, velocity and pressure values can be exchanged between opposing boundaries due to their identical nature.

2.5.2 Processing

Numerical solution techniques can be broadly categorized into four distinct methods: the finite difference method (FDM), the finite element method (FEM), the finite volume method (FVM), and the spectral method. In this thesis, the numerical simulations are based on FDM because of its simplicity, both mathematically and in coding [80]. The basic concept of the FDM is the local approximation of terms within a differential equation using differences derived from the Taylor series expansion. For a function $f(x)$, the Taylor expansion is expressed as

$$f(x+\Delta x) = f(x) + \Delta x \frac{df(x)}{dx} + \frac{1}{2}(\Delta x)^2 \frac{d^2 f(x)}{dx^2} + \cdots, \tag{2.48}$$

where Δx represents the spatial distance between two adjacent grid points. The approximation of the first derivative of $f(x)$ neglects all terms in the right-hand side of the expansion from $(\Delta x)^2$, yielding

$$\frac{df(x)}{dx} \approx \frac{f(x+\Delta x) - f(x)}{\Delta x}, \tag{2.49}$$

which is the forward scheme of FDM. Similarly, the backward scheme of the FDM is expressed as

$$\frac{df(x)}{dx} \approx \frac{f(x) - f(x-\Delta x)}{\Delta x}, \tag{2.50}$$

and the central difference as

$$\frac{df(x)}{dx} \approx \frac{f(x+\Delta x) - f(x-\Delta x)}{2\Delta x}. \tag{2.51}$$

Using the Taylor expansion series, the second derivative of the function $f(x)$ can be approximated using the central difference scheme as

$$\frac{d^2f(x)}{dx^2} \approx \frac{f(x+\Delta x) - 2f(x) + f(x-\Delta x)}{(\Delta x)^2}. \tag{2.52}$$

By differentiating each term within the grid, an algebraic equation is derived that relates each grid point to the values of neighboring cells and variables. These individual equations can then be combined into a comprehensive system of linear equations. Solving this system yields the values of the unknown variables at the grid points.

A thorough description of the numerical approach to the Navier-Stokes equation can be found in [79]. The authors introduced the FDM for discretizing the basic differential equations and applied this method to the continuous Navier-Stokes equation, resulting in a finite-dimensional (discrete) problem. They also developed specialized computer software for flow computations on rectangular domains, tailored to the discretized Navier-Stokes equation, and provided detailed instructions for its operation.

2.5.3 Post-processing

To enhance confidence in the model, verification against available literature, when possible, is recommended. Additionally, validation through experimentation or alternative methods is encouraged. A mesh independence study can be conducted to determine the minimum number of cells required for accurate simulation. These preliminary steps contribute to the overall reliability of the model and its applicability to specific applications.

Once simulation results are acquired, a thorough analysis is essential. Post-processing involves analyzing and visualizing the simulation results to extract meaningful insights. This includes generating various plots using the derived quantities and employing visualization tools to understand the results. By systematically adjusting input parameters and boundary conditions, the influence of each change on the results can be evaluated, providing a deeper understanding of the underlying physics.

3 Characterization of paper-based membranes

The characterization of porous structures can be accomplished over different length scales through the use of computational and experimental methods. The primary effective parameters governing the wicking process in porous polymeric membranes include porosity (ε), mean pore radius (r_p), mean ligament radius (r_l), and permeability (K) [81]. Moreover, the correlation between tortuosity (τ) and porosity helps to understand the diffusion process within lateral flow assays [60]. In this study, all properties related to the morphology of the porous membranes, except porosity, are derived from the 3D microstructures at the pore scale using the simulation framework PACE3D [82]. However, the porosity is determined experimentally. In addition, experimental investigations are used to analyze the wicking behavior at the macro-scale.

3.1 Microstructure modeling

This section begins with an elucidation of the generation process of porous membranes, followed by the use of computational methods to establish the correlation between the morphology of the microstructure and its effective properties.

3.1.1 Generation of porous membranes

In the field of computational modeling, porous structures can be generated synthetically using various algorithms such as Voronoi tessellation (VT). In addition, they can be generated by integrating imaging methods with data conversion techniques. In this way, the real and generated porous structures are digital twins.

Synthetic generation

Synthetic generation of porous structures allows the targeted manipulation of pore/ligament sizes and distributions, facilitating the study of numerous variants and the subsequent identification of optimized properties tailored to specific applications. The generation of porous structures based on the VT algorithm is described in detail in [83], which is implemented in the in-house software PACE3D [82]. This generation can be briefly outlined in two primary steps, as documented in [84]: i) Construction of the Voronoi diagram: First, a set of points, called Voronoi points, is pseudo-randomly distributed in the three-dimensional (3D) domain. To ensure reproducibility, consistent distributions can be achieved by employing a specific distribution function, commonly referred to as the “seed”. The algorithm is given the set of Voronoi points as an input. Voronoi regions are formed by Voronoi points in conjunction with their neighboring cells (voxels), with the proviso that within each region, each voxel is assigned to the Voronoi point that has the smallest Euclidean distance compared to the distances of that voxel to any other Voronoi point. ii) Structure generation: The solid matrix is generated by placing solid spheres along the cells that have at least three distinct Voronoi regions in their immediate vicinity. These spheres are then merged through a smoothing process to form the structure.

Digital twin of real porous membranes

The generation of porous structures can also be approached by combining imaging techniques with data conversion. This approach allows the creation of a digital replica, called a “digital twin”, derived from an actual structure. The goal is to use computational techniques to study and analyze this replicated structure. The first step is to obtain high-resolution 3D images of the porous structure. In this thesis, confocal laser scanning microscopy (CLSM) is used as one method to generate image stacks. In addition, computed tomography (CT) serves as another imaging technique capable of capturing images of a porous CN membrane, as shown in Figure 3.1a.

CLSM produces a stack of images from the top layer to the bottom layer of the membrane, with the brightness of the images decreasing as the depth of the stack increases. To compensate for this intensity gradient, each image within the CLSM stack is normalized to its maximum gray value. The images are then converted to 8-bit images, resulting in each image within the CLSM stack containing $2^8 = 256$ gray levels. Similarly, the CT scan method also produces grayscale images, but normalization is typically unnecessary due to the absence of intensity gradients. To mitigate unwanted effects and noise in both CLSM and CT scan images, image processing techniques are applied to the entire image stack. As suggested by [81], a Gaussian filter with a fixed standard deviation of 450 nm is applied to mitigate local gray value fluctuations.

Up to this point, the ability to clearly distinguish between the pores and the structure has not been achieved. This is where the segmentation step comes in. Achieving a clear separation between pores and ligaments within the slices of the image stack is a challenge. In other words, setting a threshold for distinguishing the pore space from the solid matrix is crucial. In this study, the segmentation method proposed by Ley et al. [61] is employed. Through an iterative procedure, the threshold value is systematically changed from an initial starting point. After each adjustment, the resulting porosity of the segmented structure is calculated (see section 3.1.2). The final threshold value is the one that yields the porosity closest to the previously known value derived from the gravimetric method (see section 3.2). Pixels with grayscale values below this threshold are classified as part of the pore space, while those above are classified as part of the solid matrix. This creates an image stack containing binary images, as shown in Figure 3.1b. This segmented image stack is then processed to generate an equidistant grid of voxel data, a step known as reconstruction, which produces the digital twin of the real membrane. Figure 3.1c shows the 3D structural model that can be used for further computational studies. Image processing is performed using Fiji-ImageJ 1.53c [85], and the final data conversion takes place within the PACE3D simulation environment.

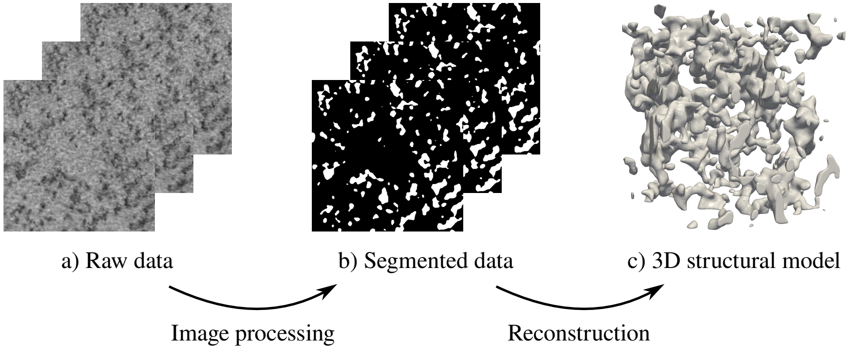
a) Raw data

b) Segmented data

c) 3D structural model

Figure 3.1: Conversion of CT scan data into the digital twin; a) Exemplary raw data set from a CT scan of a porous CN membrane displayed in three layers of an image stack. b) Distinctly segmented pore (black) and structure (white) spaces obtained by image processing. c) Generation of the reconstructed 3D model using the in-house software PACE3D [82].

3.1.2 Porosity

The interval from 0 to 1 establishes the limits for the porosity value. According to Eq. (2.1), the determination of the porosity (ε) involves the division of the pore volume ($\forall_{\mathrm{p}}$) by the total volume ($\forall_{\Omega}$). The use of an equidistant grid in this study allows this volume ratio to be represented by the corresponding cell count ratio. Thus, porosity can be expressed as the sum of all voxels representing pore space (N_p) divided by the total number of voxels within the domain (N), where N is the product of voxel counts along each dimension

$$\varepsilon = \frac{N_\mathrm{p}}{N} = \frac{N_\mathrm{p}}{N_x \cdot N_y \cdot N_z}. \tag{3.1}$$

Figure 3.2a depicts a sectional view of a binary voxel-based structure, where the structure is shown in gray with recognizable voxel boundaries. This visualization demonstrates the feasibility of counting all voxels representing pore space to calculate porosity. Figure 3.2b shows a larger segment of the 3D structure where the surface of the structure has been smoothed to improve clarity and facilitate visualization. This approach is also used for the presentation of the following figures in this chapter. The observed porosities of the membranes examined in this study fall within the approximate range of 0.8 to 0.9, which corresponds to a percentage range of 80 to 90%.

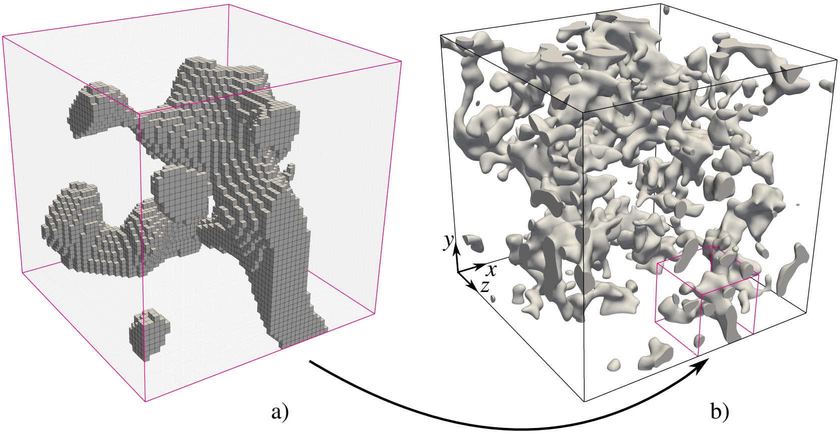

Figure 3.2: Visualization of a 3D structure in the Cartesian coordinate system. In a), a section of the 3D structure is shown, with a binary voxel-based structure represented in gray. In b), a larger representation of the structure is depicted, where the surface has been smoothed for visual clarity.

3.1.3 Pore and ligament radii

As discussed in section 2.3.6, the study of porous media is concerned with effective properties. This section contains a brief discussion of the derivation of geometric pore radii and pore size distributions, with reference to [8]. It then presents the methodology of [81] for calculating the effective pore radius in this work. As an aside, the possibility of experimental derivation of the pore radii using capillary flow porometry is briefly described in section 3.2.

After obtaining the digital twin of a real membrane (see section 3.1.1), the calculation of its mean geometric pore radius (r_p) is of interest, which is performed within the PACE3D software environment. To determine r_p, this approach first computes a Euclidean distance field (EDF) for each voxel in pore space based on the algorithm introduced in [86]. Next, a medial axis is constructed by a skeletonization algorithm adapted from [87] based on the previously computed EDF, where each voxel on this medial axis represents the maximum achievable radius of a sphere in pore space. Finally, all EDF values corresponding to the medial axis are recorded. By calculating the arithmetic mean of these values, the mean pore radius can be determined. In addition, a pore size distribution can be delineated by including all extracted values. Similarly, the same approach can be used for the structural space to determine the mean ligament radius (r_l) and the ligament radius distribution. Figure 3.3a shows a portion of a reconstructed membrane illustrating local pore radii. The area shown consists of 200×200×200 cells, corresponding to dimensions of 30×30×30 µm. In addition, Figure 3.3b shows the pore radius distribution for the digital twin. Figure 3.4 depicts the local ligament radii and their respective distributions within the same geometry.

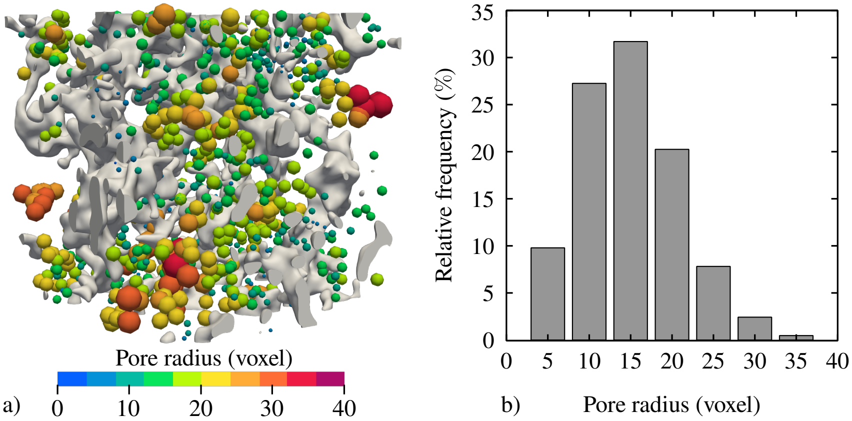

Figure 3.3: Visualization of a) local pore radii within a portion of the reconstructed membrane and b) their respective distributions.

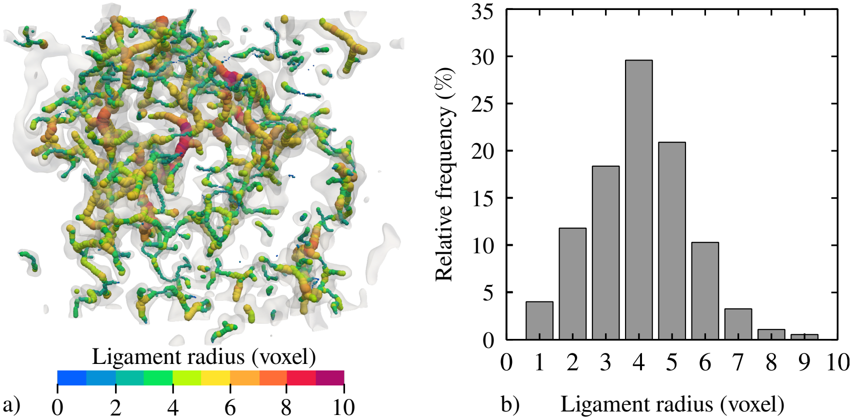

Figure 3.4: Visualization of a) local ligament radii within a portion of the reconstructed membrane and b) their respective distributions.

The effective pore radius is determined after the pore/ligament radii have been calculated [24]. Previous observations indicate that an effective pore radius, rather than the geometric pore radius, must be used to effectively predict the wicking process in open-cell and complicated porous microstructures using standard macroscopic flow models. In [81], a parametric study was performed to address this issue by simulating complex microstructures within the membrane using simplified structures. The meniscus evolution and the corresponding mean surface curvature for each structure were described using a phase-field technique with a special wetting boundary condition. The primary result of the study was the construction of an analytical relationship, with a correction factor (CF), between geometric structure parameters and an effective capillary radius (r_{eff})

$$r_{\mathrm{eff}} = CF(r_{\mathrm{l}}, r_{\mathrm{p}}) \cdot r_{\mathrm{p}}. \tag{3.2}$$

To obtain the correction factor in [81], this correlation was fitted to the simulation results of the simplified structures, resulting in

$$CF(r_{\mathrm{l}}, r_{\mathrm{p}}) = \frac{1.98}{r_{\mathrm{l}}/r_{\mathrm{p}}} + 3.012. \tag{3.3}$$

Experimental results have confirmed the reliability of the derived effective capillary radius, as documented in [81]. The use of this calculated correlation for effective pore radii obviates the need for further experimental fitting procedures in demonstrating structure-property linkages.

3.1.4 Tortuosity

After the acquisition of the digital twin for the actual membrane (section 3.1.1), the computation of its effective tortuosity (τ_{eff} from section 2.2) becomes a point of interest, and this computation is carried out within the PACE3D software framework. To achieve this, the Laplace equation given by

$$\nabla \cdot (-\sigma_{\mathrm{p}} \nabla \phi) = 0, \tag{3.4}$$

is solved numerically in a Cartesian grid using the finite difference method within the reconstructed membrane structure [8]. In this equation, σ_{p} is the intrinsic conductivity and ϕ is a potential function. To determine the effective tortuosity, a potential difference of $\Delta\phi = 1\,\mathrm{V}$ is applied across two edges of the membrane structure at a distance L, thereby defining a flow direction through the pore space. A homogeneous Neumann boundary condition is imposed on the surface between the pore space and the structure space to inhibit flow perpendicular to the solid matrix. The resulting current (I) through the pore space is derived from the local gradient of the potential field ($\nabla\phi$). Using Ohm's law, which states that the potential difference is equal to RI, the effective resistance (R) is determined, which leads to the effective conductivity [8, 16]

$$\sigma_{\mathrm{eff}} = \frac{I}{\Delta\phi} \cdot \frac{L}{A}, \tag{3.5}$$

where A is the cross-sectional area. Finally, the effective tortuosity τ_{eff} is obtained from Eq. (2.5). Figure 3.5 depicts a portion of a reconstructed membrane showing some lengths calculated by the tortuosity tool. The area shown consists of 200×200×200 cells, corresponding to dimensions of 30×30×30 µm. This means that a particle has to cross at least 200 voxels (cells) from one side of the domain to the other, for example in the x-direction. Essentially, a streamline can follow a straight path of 200 cells, assuming no solid bar obstructs its trajectory, as indicated by the blue color.

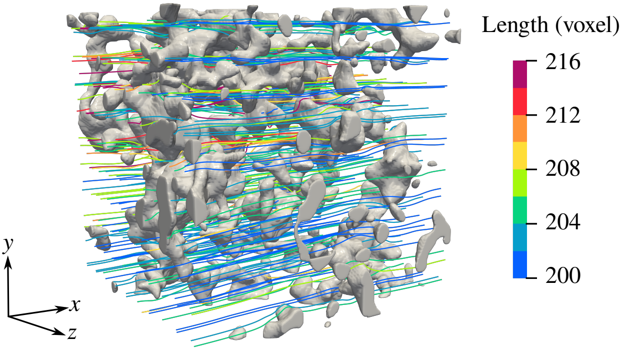

Figure 3.5: Visualization of winding of the transport pathways within a portion of the reconstructed membrane. The length of each transport pathway is evaluated relative to the domain length in the x-direction, which is set to 200 cells.

The determination of an effective tortuosity quantified as a singular numerical value, is derived from the overall structure. Eq. (2.6) establishes tortuosity as a function of porosity, where the cementation exponent serves as an empirical parameter. This study focuses on uncovering the relationship between tortuosity and porosity in porous membranes. For this purpose, 75 synthetic porous structures are generated using Voronoi tessellation with variations in pore shape and porosity by varying five different seeds for each porosity. The tortuosity tool then calculates the tortuosity of each structure in only one spatial direction. Figure 3.6 illustrates the reduction in tortuosity with increasing porosity, where each simulation point represents data from five structures with different seeds. This implies that the porosity of the structure influences the effective tortuosity, independent of the distribution of Voronoi points.

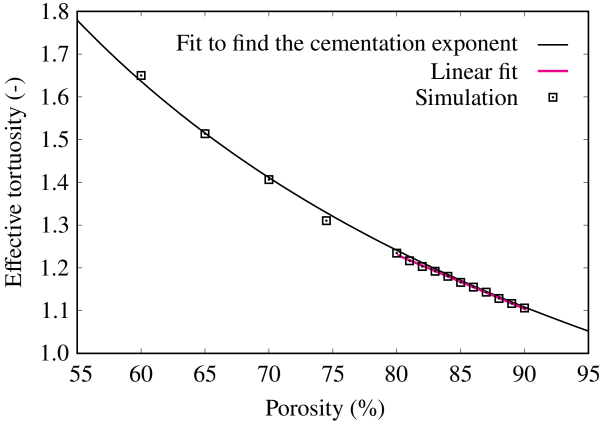

Figure 3.6: Effective tortuosity over porosity of porous structures generated based on Voronoi tessellation. Each simulation point represents data from five structures with different seeds.

Fitting the calculated tortuosities with Eq. (2.6) yields a cementation exponent of $m = 1.962322$. However, it is observed that for structures with porosities between 0.8 and 0.9, the tortuosity exhibits a linear behavior, expressed as

$$\tau_{\text{eff}} = -1.2621\varepsilon + 2.24028. \tag{3.6}$$

3.1.5 Permeability

Once the digital twin of the membrane has been obtained (see section 3.1.1), determining its permeability (**K**) represents a crucial step. Conventional techniques for calculating permeability, such as the Kozeny-Carman equation (Eq. (2.17)), often rely on simplified model assumptions for porous structures and ignore the intricate morphology of the porous framework. To address this limitation, these techniques incorporate an adjustment factor into their permeability calculation, which introduces a potential for inaccuracy. In this work, to obviate such an issue, the permeability is determined by performing numerical simulations within the PACE3D software environment.

To ascertain the permeability of the membrane, a simulation of fluid flow through the pore space is conducted. Water is chosen as the fluid and is assumed to be an incompressible, Newtonian fluid with a viscosity of $\mu = 1.0\,\mathrm{mPa\,s}$ at 20 °C. To induce flow through the pore space, a pressure gradient (∇p) is defined along a spatial direction, such as the x-direction, across two opposite sides of the simulation domain (inflow/outflow condition). The remaining four domain boundaries are assumed to be impermeable to fluid flow, with free-slip conditions applied. This results in zero normal velocity components at the boundary, while allowing for tangential flow. At the interface between the membrane and the fluid, a no-slip condition is applied. The numerical solution of the continuity equation (Eq. (2.28)) and the Stokes equation (Eq. (2.32)) is then performed within the pore space. Due to the substantially low ratio of fluid inertial to viscous forces, quantified by the Reynolds number, the Stokes equation becomes applicable for simulating fluid flow within the pore space.

As a side note, the Reynolds Number is defined as

$$Re = \frac{\rho_{\mathrm{L}} U r_{\mathrm{p}}}{\mu}, \tag{3.7}$$

where the density of water is $998\,\mathrm{kg\,m^{-3}}$ and the mean pore radius can be taken from Table 3.1. If the average wicking velocity of water (U) is approximated to be $0.3\,\mathrm{mm\,s^{-1}}$, the corresponding Reynolds numbers for water wicking in membrane types A and B are 7.35×10^{-4} and 6.87×10^{-4}, respectively. Since $Re \ll 1$, the influence of inertial forces can be considered negligible in this analysis. This allows for the use of the Stokes equation instead of the Navier-Stokes equation for simulating fluid flow within LFAs.

By solving the Stokes equation with appropriate boundary conditions, the local velocity distribution can be determined. The permeability is then calculated using Darcy's law according to Eq. (2.7). Different components of the permeability tensor can be obtained by varying the initial pressure boundary condition in alternative spatial directions (y and z-directions). The validation of the implemented algorithm can be found in [8].

3.2 Experimental characterization

In addition to computational methods, experimental techniques are employed in this study to characterize porous membranes. Two experimental techniques are the gravimetric method for determining porosity and capillary flow porometry for obtaining information about pore size distribution, as detailed in [8]. This study only uses the gravimetric method, though both methods are briefly explained.

In the context of this work, membrane characterization also includes the measurement of wicking time across the membrane. To address this aspect, the methodology used for the macro-scale wicking experiment is explained.

3.2.1 Gravimetric method

The gravimetric method, described in detail in [8] and summarized here, is used to experimentally determine the porosity of a porous CN membrane. Utilizing the known density of water, the difference in weight between the wet and dry membranes reveals the amount of water contained within the pores of the membrane. Assuming that the pores are completely saturated with water, the void volume can be determined and the porosity of the membrane can be derived from the formula

$$\varepsilon = \frac{m_{\text{wet}} - m_{\text{dry}}}{\rho_{\text{water}}} \frac{1}{V_{\Omega}}. \tag{3.8}$$

3.2.2 Capillary flow porometry

Capillary flow porometry is an experimental technique used to determine pore sizes in porous CN membranes. The method involves subjecting a fully wetted membrane to increasing gas pressure until the liquid is forced out of the pores. The appearance of flow indicates the presence of the largest pores, corresponding to the first bubble point. By applying a modified version of the Young-Laplace equation (Eq. (2.20)) to the pressure at the first bubble point, the maximum pore size can be calculated.

The plot of flow rate versus gas pressure is known as the wet curve. An additional measurement using a dry membrane can establish a dry curve. The half-dry curve is obtained by taking the average of the wet and dry curves. The mean pore size is determined at the intersection of the wet and half-dry curves, while the area between the first bubble point and the completely emptied membrane represents the pore size distribution [88].

3.2.3 Macro-scale wicking experiment[1]

After production, wicking experiments are often performed to evaluate the quality or classification of membranes. Since this study is primarily concerned with the effect of membrane profiles on wicking behavior at the macro-scale, wicking

---

[1] The wicking experiment formulated in this section is derived from the methodology described in the peer-reviewed journal article authored by Jamshidi et al. [36]. The content is reproduced from “Geometric flow control in lateral flow assays: Macroscopic single-phase modeling” Physics of Fluids, June 2022; 34(6): 062110, with the permission of AIP Publishing.

experiments were performed with different membrane profiles. The experimental measurements were performed in collaboration with *Sartorius Stedim Biotech GmbH* in Göttingen, Germany. Figure 3.7 shows some of the membrane profiles investigated in this study, namely straight, barbell, hexagon, sand timer, and T-shaped channels. The membrane itself was a commercially available cellulose nitrate membrane reinforced with a polyester film, known as *UniSart*®, *CN 140 backed*, provided by *Sartorius*. This membrane has an average thickness of 240 µm. According to the manufacturer, purified water requires between 95 and 155 s to travel a distance of 40 mm across this membrane. The time required for complete wetting of a membrane is referred to as the total wicking time, while the progressive pattern of wicking length with time elucidates the inherent wicking behavior. The profiles sought in this investigation have larger widths compared to the critical width of the *CN 140* membrane (600 µm [89]). This implies that the profile widths have no influence on the wicking process and eliminate any boundary effects.

A standardized experimental methodology is presented to obtain wicking curves for membranes with profiles shown in Figure 3.7a–d. To create controlled and reproducible conditions, a specially designed wicking time-measuring device from *Sartorius* was used for the experiments. The membrane samples were first cut into the desired profiles, and then the shorter edges (bottom and top) of the membranes were clamped to a rectangular plastic frame. This held the paper-based membranes in a flat and stable configuration, preventing any bending. The frame was then placed in the basin of a custom-built apparatus specifically designed for wicking time measurements. A thin layer of the test liquid (in this case, water) was present at the bottom of the basin.

Upon contact of the frame with the bottom of the device, water initiated the wicking process across the membrane while a camera captured sequential images of the front surface of the membrane at a rate of one per second. The back of the membrane was illuminated by a light-emitting diode (LED). Custom algorithms were used to determine the evolution of the liquid front over time by detecting changes in the contrast between the dry and wet portions of the membrane.

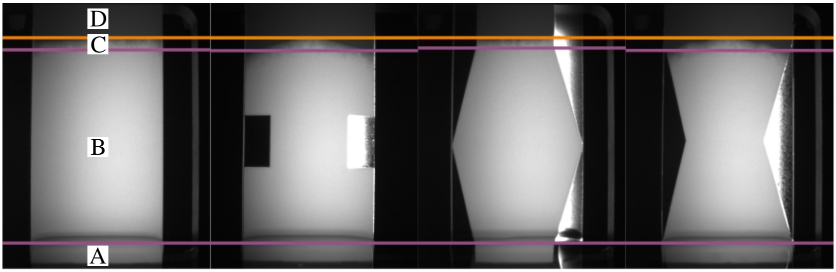

a) Straight b) Barbell c) Hexagon d) Sandtimer

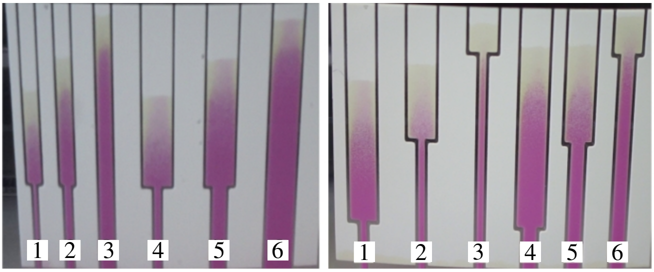

eI) T-shaped I eII) T-shaped II

Figure 3.7: Wicking experiments with varying membrane profiles. a–d) The membranes were in contact with the water source, resulting in full saturation in region A. Full saturation is also observed between the magenta lines, designated as region B. Partial saturation is indicated between the upper magenta and orange lines, illustrating the diffuse interface (region C), while the membranes remain completely dry above the orange lines. eI and eII) The visualization of the wicking process in samples 1–6 is enhanced by the inclusion of phenol red in the liquid (water). Reproduced from [36], with the permission of AIP Publishing.

For membranes with a width of 5 mm, excessive light from the source penetrated through the membrane, resulting in overexposed photographs. Consequently, a minimum threshold of 15 mm was set for the membrane width to mitigate this effect. Furthermore, the limitations of the custom-made device dictated the selection of a maximum width of 25 mm and a maximum length of 40 mm. To ensure reproducibility, the wicking experiments were repeated six times for each profile.

The membrane has four distinct regions, as shown in Figure 3.7a. In region A, the membrane interfaces with a liquid source, ensuring a continuous supply of liquid for complete wetting. Region B is the portion where the membrane is fully saturated with liquid. Region C is a "mushy" region characterized by sections with both partially wetted and dry surface areas. Region D indicates the absence of any liquid in the membrane. The boundary between regions C and D, designated by the orange line, is identified as the precursor of impregnation, following the terminology in [90]. In this study, it serves as the liquid front. Consequently, the wicking length is defined as the sum of the lengths of regions B and C.

In addition to conducting experiments with straight, barbell, hexagon, and sand timer profiles using the specified instrument, *Sartorius* provided videos showing experiments with alternative membrane profiles, such as the T-shaped membranes shown in Figure 3.7eI and eII. The addition of phenol red dye as a coloring agent to the water reservoir prior to video recording was intended to improve visibility and ease the analysis process, resulting in a comprehensive observation and understanding of the wicking process. One frame per second was then extracted from each video sequence. The extracted image sequence was analyzed using the image processing software Fiji-ImageJ 1.53c [85], specifically using its "ColorThreshold" tool. The goal was to identify and track the foremost colored pixel to determine the position of the liquid front for subsequent analysis.

3.3 Characteristics of studied membranes

This section initially presents the structural properties of two types of CN membranes. Subsequently, the behavior of these membranes in contact with two different liquids is discussed. The insights gained from this analysis will be utilized in the macro-scale modeling presented in the subsequent chapters.

3.3.1 Structural properties

The company *Sartorius* provided images of two types of membranes using confocal laser scanning microscopy (CLSM). The image stack of the first membrane type (type A) had an image resolution of 80 nm/voxel, while that of the second type (type B) had a resolution of 160 nm/voxel. Digital twins of these membranes were generated as described in section 3.1.1. In order to ensure an identical resolution for both membranes, the reconstructed structure grid of type A was modified to 160 nm/voxel. Using PACE3D, every two cells are combined in each spatial direction. This resulted in domains of $1020 \times 1020 \times 860$ cells and $620 \times 620 \times 880$ cells (in x, y, and z-directions) for membrane types A and B, respectively.

These domains span the entire thickness of the membrane (in z-direction), about 140 µm. Is this domain size representative of the entire membrane, one might ask. In [8], a representative volume element (RVE) analysis was performed to answer this question. The primary goal of the RVE analysis is to demonstrate that the images provide sufficient detail about the microstructure of the membranes. The second objective is to show that larger parts do not provide more information. Considering the entire membrane thickness, the RVE analysis in [8] indicates a minimum length of 36 µm in each remaining direction. In this work, the domain size in its shortest dimension is approximately 100 µm, which exceeds the RVE length for CN membranes. Thus, these domains act as representative models for the entire membranes and are suitable for evaluating the porosity, permeability, and pore/ligament radius values derived from the microstructure modeling described in section 3.1. These values for type A and type B membranes are given in Table 3.1. Using the pore and ligament radii from this table and applying Eq. (3.2), the effective pore radii for type A and type B membranes are determined to be 24.4 and 19.2 µm, respectively.

Table 3.1: Properties of the reconstructed CN membranes from CLSM images provided by *Sartorius*.

Membrane	Porosity (%)	Mean pore radius (μm)	Mean ligament radius (μm)	Permeability (m^2)
Type A	90.6	2.45	0.70	2.47×10^{-12}
Type B	81.7	2.29	0.85	1.29×10^{-12}

3.3.2 Wetting properties

The wetting behavior of the two types of CN membranes supplied by *Sartorius* is investigated. A Newtonian liquid, either water or another liquid known under the trade name *Porefil*® from *Porometer*, replaces the gas (air) in the pore space of the membrane. Table 3.2 presents the density and viscosity values of the fluids used in this investigation.

Table 3.2: Properties of the fluids involved in the wicking of CN membranes at 20 °C [8].

Fluid	Density (kg m^{-3})	Viscosity (kg m^{-1} s^{-1})
Air	1.0	1.76×10^{-5}
Water	998	1.0×10^{-3}
Porefil®	1800	2.2×10^{-3}

As described in section 2.4.4, the hydrophobic to hydrophilic transformation of CN membranes is achieved by surfactant impregnation. These surfactants, which are known to migrate from the solid matrix surface during wicking, induce dynamic changes in both the contact angle and the surface tension coefficient. In the present study, this dynamic behavior is ignored for simplicity. Therefore, using constant values from [8], the water-air surface tension coefficient within CN membranes is considered to be 0.053 N m^{-1} with a corresponding contact angle of 36°. For *Porefil®*, the surface tension coefficient is $0.016\,\mathrm{N\,m^{-1}}$ and the contact angle is 0°.

To predict wicking behavior at the macro-scale, Eq. (2.41) is selected as a one-dimensional (1D) momentum balance. By evaluating the relative magnitudes of the forces involved, dominant terms in the equation can be identified, allowing less influential forces to be neglected. The consideration or neglect of gravitational effects can be accomplished by analyzing the Bond number (Bo) [36]. The Bond number is a dimensionless parameter that characterizes the ratio of gravitational to capillary forces and is defined as [91]

$$Bo = \frac{\rho_{\mathrm{L}} g H}{\gamma_{\mathrm{LG}}/r_{\mathrm{p}}}, \tag{3.9}$$

where indices L and LG represent the liquid phase and the liquid-gas interface, respectively. The variable ρ_{L} denotes the liquid density, g the gravitational acceleration, H the total wicking length, γ_{LG} the surface tension coefficient between the liquid and gas phases, and r_{p} the mean pore radius. The properties of water as the liquid phase and air as the gas phase can be taken from Table 3.2 and the mean pore radius from Table 3.1. Additional constants include $g = 9.8\,\mathrm{m\,s^{-2}}$ [23], $H = 0.04\,\mathrm{m}$. Substituting these values into Eq. (3.9), the resulting Bond numbers for membrane type A and type B are 0.0181 and 0.0169, respectively, indicating that $Bo \ll 1$. As a result, despite the vertical orientation of the membranes in the wicking experiments with water, the influence of gravity remains insignificant – a circumstance that is also true in practical scenarios where lateral flow assays (LFAs) are positioned horizontally. Therefore, gravitational forces are considered negligible compared to capillary forces when water is used as the wetting fluid. When *Porefil®* serves as the wetting fluid, the Bond numbers for membrane types A and B are 0.1082 and 0.1011, respectively. In such cases, gravitational forces must be taken into account. For a more detailed exploration of considerations regarding the influence of gravity, readers are directed to [92].

The assessment of whether to include or neglect inertial forces can be made by examining the Weber number. The Weber number, a dimensionless parameter that measures the importance of fluid inertia relative to surface tension, is defined as [8]

$$We = \frac{\rho_\mathrm{L}\dot{l}^2}{\gamma_\mathrm{LG}/r_\mathrm{p}}, \tag{3.10}$$

where the average wicking velocities, denoted as $\dot{l}$, are approximately $0.3\,\mathrm{mm\,s^{-1}}$ for water and $0.04\,\mathrm{mm\,s^{-1}}$ for *Porefil*®, due to its low surface tension. The corresponding Weber numbers for water wicking in membrane types A and B are 4.16×10^{-9} and 3.89×10^{-9}, respectively, while those for *Porefil*® wicking are 4.42×10^{-10} and 4.13×10^{-10}, respectively. Consequently, the effect of inertial forces can be considered negligible in this study. Finally, the presence of very small pores with relatively large surfaces in CN membranes introduces a significant influence of frictional forces, which counteracts the driving capillary force and results in Eq. (2.43) as the expression governing the wicking height.

3.4 Summary

In this chapter, the primary parameters affecting wicking in porous polymeric membranes are investigated, including porosity, mean and effective pore radius, mean ligament radius, permeability, and tortuosity. These parameters are evaluated employing reconstructed digital twins of real porous membranes in equidistant 3D grids. In addition, experimental methods such as the gravimetric method for porosity determination and a macro-scale wicking experiment are explained. Furthermore, the structural properties and wetting behavior of two types of CN membranes are presented, laying the foundation for macro-scale modeling in subsequent chapters. By integrating computational and experimental approaches, this chapter provides a comprehensive characterization of paper-based membranes for lateral flow assays.

4 Macroscopic single-phase modeling of wetting and sensitivity analysis in lateral flow assays[1]

To study fluid propagation in CFD simulations, it is essential to mesh the entire fluid space. In the context of studying fluid propagation in porous media, this means discretizing all the pores within the porous structure. However, in the case of porous membranes with extremely small pores, attempting to discretize all pores becomes impractical. As a result, simulations can only cover a limited distance, typically a few hundred micrometers. If the goal is to analyze the wicking behavior over the entire length of the membrane, which is typically 2 to 4 cm, it becomes infeasible to mesh the entire pore space due to the tremendous increase in the number of mesh cells. Solving equations, such as the Stokes equation, for an excessively large number of cells becomes computationally impractical.

To address this challenge in computational simulations or mathematical modeling of fluid propagation in lateral flow assays (LFAs), it becomes necessary to

---

[1] The single-phase wicking model developed in this chapter is based on the work published in the peer-reviewed journal article by Jamshidi et al. [36]. Reproduced from "Geometric flow control in lateral flow assays: Macroscopic single-phase modeling" Physics of Fluids, June 2022; 34(6): 062110, with the permission of AIP Publishing. The research data of the developed wicking model have been managed using Kadi4Mat, a research data infrastructure tailored for materials science [93]. Subsequently, the complete dataset was exported from Kadi4Mat and is currently available in an open-access repository on Zenodo at https://doi.org/10.5281/zenodo.6389659 [94].

treat the domain as a porous zone. This chapter presents the development of a macro-scale single-phase model for fluid flow in LFAs, where the domain is considered a porous zone. The model aims to evaluate the effect of the membrane shape on the motion of the fluid front. The wicking behavior is investigated by studying axisymmetric geometries with different cross-sections. The validity of the model is confirmed by experimental studies. The calculated velocity obtained from the model is then used in a convection-diffusion-reaction model to explore the reaction processes. This is followed by a sensitivity analysis in sandwich-type LFAs.

4.1 Single-phase wicking model

Theoretical modeling of liquid transport in porous media serves as a fundamental framework for optimizing and controlling the wicking process. Modeling approaches facilitate the achievement of specific flow velocities at specific locations, such as at the TL/CL, or the achievement of the fastest imbibition, as demonstrated in [95]. Elizade et al. [68] delved into the macroscopic study of capillary-driven flow in paper-based membranes, presenting a mathematical solution to determine the wicking time associated with an arbitrary cross-sectional profile. In addition, their methodology allowed the solution of the inverse problem, enabling the identification of the shape required to achieve a given fluid velocity. The study by Shou et al. [96] investigated the effect of local segment width and length on capillary motion in the presence of different segments. For this work, an extension of the models proposed by Elizade et al. [68] and Shou et al. [96] is employed to model capillary-driven flow through membranes of varying shapes. These models are generalized to derive the wicking time (t) applicable to any membrane shape with a single-passage profile, specifically addressing multi-segment membrane profiles as shown in Figure 3.7. In this section, the developed single-phase model is introduced to elucidate fluid propagation first within single-segment and then multi-segment membranes.

4.1.1 Single-segment membranes

Figure 4.1 shows a schematic of a membrane with an arbitrary shape next to a straight membrane. The term “arbitrary shape” implies that the membrane profile can be described by a single function. On the other hand, a straight membrane is characterized by a single rectangular configuration, where no cross-sectional change is present for the fluid front. Since multi-segment membrane profiles will be studied later, these two profiles are currently referred to as the first segment.

The majority of paper-based devices are characterized by a limited surface area for reagent storage, where the thickness dimension of the membrane is considerably smaller than the length and width dimensions. Thus, these devices typically adopt a two-dimensional (2D) geometry. Fluid imbibition within their homogeneous porous media induces unidirectional flow that progresses from wet to dry regions, thereby limiting the complexity of the assay [97]. In the context of LFAs discussed in this chapter, a single-passage profile is considered for fluid flow. Since the test strips are intentionally designed to facilitate flow in only one direction, the application of the Darcy equation is limited to a unidirectional framework. Consequently, despite the 2D variation evident in $A(x)$ as the cross-sectional area, the flow dynamics remain unidirectional, resulting in a one-dimensional (1D) model presented in this chapter.

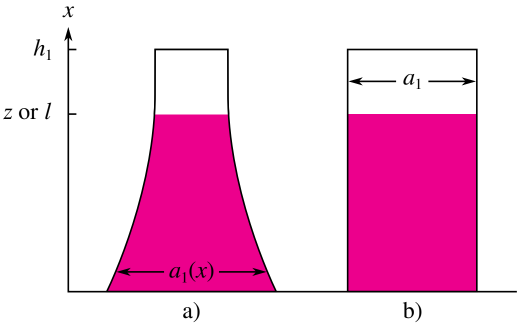

Figure 4.1: Illustration of the membrane profiles: a) arbitrary shape, b) straight configuration.

Figure 4.1a shows a membrane of arbitrary shape, characterized by a total length h_1. With a constant thickness throughout, the width of the membrane, denoted as $a_1(x)$, serves as a representation of the cross-sectional area for the fluid flow ($A_1(x) = a_1(x) \cdot \text{thickness}$). If the fluid front moves within this membrane, it can be written as $z \leq h_1$, where z is the fluid front position. The volumetric flow rate (Q) in this case, according to the 1D Darcy equation, is expressed as [96]

$$Q = U_{\text{fluid}} A_{\text{p}} = \frac{u_1(x)}{\varepsilon} A_1(x) \varepsilon = u_1(x) A_1(x) \Rightarrow Q = -\frac{K}{\mu} \frac{dp}{dx} A_1(x). \tag{4.1}$$

By integrating Eq. (4.1), the following expression is obtained

$$\int_{p_{\text{inlet}}}^{p_z} dp = -\frac{\mu Q}{K} \int_0^z \frac{dx}{A_1(x)}. \tag{4.2}$$

In this equation, the negative sign on the right side indicates a decrease in fluid pressure from the inlet to the fluid front along the membrane. The pressure at the inlet is atmospheric pressure (p_{atm}), and the pressure at the liquid front is $p_z = p_{\text{atm}} - \Delta p_{\text{c}}$, with Δp_{c} as the capillary pressure. Therefore, it can be written

$$\Delta p_{\text{c}} = \frac{\mu Q}{K} \int_0^z \frac{dx}{A_1(x)}. \tag{4.3}$$

Within this model, the neglect of gravitational and inertial effects is justified by the small values of both the Bond and Weber numbers (see section 3.3.2). Therefore, the only driving force, namely the capillary force, counteracts the viscous force. As a result, the magnitude of the pressure drop is equal to the capillary pressure. Considering $Q = U_{\text{fluid}} A_{\text{p}}$ and $U_{\text{fluid}} = dz/dt$ [34], it can be written

$$Q = \frac{dz}{dt} A_1(z) \varepsilon. \tag{4.4}$$

Inserting Eq. (4.4) into Eq. (4.3) gives the wicking time for a membrane with any profile

$$t_1(l) = \frac{\mu \varepsilon}{K \Delta p_{\text{c}}} \int_0^l A_1(z) \left[\int_0^z \frac{dx}{A_1(x)} \right] dz. \tag{4.5}$$

Keeping the membrane thickness constant, Eq. (4.5) can be rewritten using the width of the membrane $a_1(x)$

$$t_1(l) = \xi_{\text{eff}} \int_0^l a_1(z) \left[\int_0^z \frac{dx}{a_1(x)} \right] dz, \tag{4.6}$$

where the term preceding the integral $\xi_{\text{eff}} = \mu\varepsilon/(K\Delta p_{\text{c}})$ is identified as the wicking coefficient – a consistent value that depends on the membrane type and wetting conditions, regardless of the membrane profile. Using an identical membrane type and the same wetting conditions across different membrane profiles ensures the same wicking coefficient. The influence of shape on wicking behavior is governed solely by the integral term.

As shown in Figure 4.1b, for a straight membrane, the cross-sectional area remains constant ($A_1(x) = A_1$) because both the width and thickness of the membrane are constant. Therefore, the wicking time for a straight membrane can be expressed as follows, consistent with the result of the capillary model considering capillarity and friction (Eq. (2.43))

$$t_1(l) = \xi_{\text{eff}} \int_0^l A_1 \left[\int_0^z \frac{dx}{A_1} \right] dz = \frac{1}{2} \xi_{\text{eff}} l^2, \tag{4.7}$$

where $\xi_{\text{eff}} = \mu\varepsilon/(K\Delta p_{\text{c}})$ is the wicking coefficient, with $\Delta p_{\text{c}} = 2\gamma_{\text{LG}} \cos\theta / r_{\text{eff}}$.

4.1.2 Multi-segment membranes

The objective of this work is to investigate the effect of geometry on wicking behavior at the macroscopic level. In this section, the single-phase model developed to elucidate fluid propagation in single-passage, multi-segment membranes is presented. Figure 4.2 schematically displays membrane profiles in hexagonal, sand timer-shaped, and T-shaped configurations, with corresponding experimental investigations presented in Figure 3.7.

The mathematical formulations that govern wicking in the first segment are explained in section 4.1. Attention now turns to the subsequent advancement of the liquid, within the second segment. When the liquid front is within the second segment ($h_1 < z \leq h_2$), the cumulative pressure drop is composed of the pressure drops across the entire first segment and the portion of the second segment wetted by the liquid. This cumulative pressure drop corresponds to the capillary pressure

$$\Delta p_c = \frac{\mu Q}{K} \int_0^{h_1} \frac{dx}{A_1(x)} + \frac{\mu Q}{K} \int_{h_1}^{z} \frac{dx}{A_2(x)}. \tag{4.8}$$

Considering $Q = U_{\text{fluid}} A_p = u_2(z) A_2(z)$ and $U_{\text{fluid}} = dz/dt$, it can be written

$$Q = \frac{dz}{dt} A_2(z) \varepsilon. \tag{4.9}$$

Consequently, Eq. (4.8) is reformulated as

$$\Delta p_c = \frac{\mu}{K} \frac{dz}{dt} A_2(z) \varepsilon \left[\int_0^{h_1} \frac{dx}{A_1(x)} + \int_{h_1}^{z} \frac{dx}{A_2(x)} \right], \tag{4.10}$$

and the wicking time for the second segment is given by

$$t_2(l) = \frac{\mu \varepsilon}{K \Delta p_c} \int_{h_1}^{l} A_2(z) \left[\int_0^{h_1} \frac{dx}{A_1(x)} + \int_{h_1}^{z} \frac{dx}{A_2(x)} \right] dz. \tag{4.11}$$

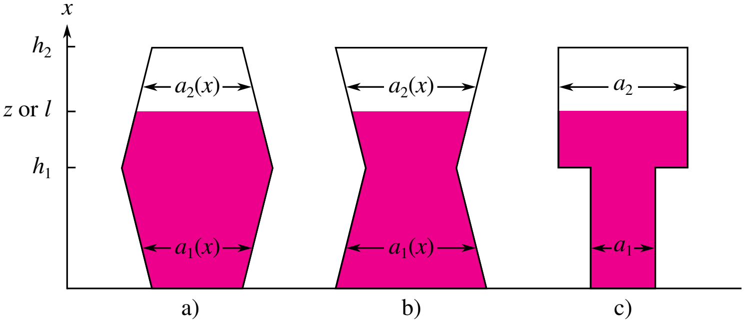

Figure 4.2: Illustration of the membrane profiles: a) hexagonal, b) sand timer-shaped, and c) T-shaped configuration.

Figure 4.3 schematically depicts membrane profiles with a barbell-shaped configuration, providing an opportunity to study the wicking process in the third segment using the developed model. Analogous to the second segment, the wicking time for the third segment can be formulated as

$$t_3(l) = \frac{\mu\varepsilon}{K\Delta p_c}\int_{h_1+h_2}^{l} A_3(z)\left[\int_0^{h_1}\frac{dx}{A_1(x)} + \int_{h_1}^{h_1+h_2}\frac{dx}{A_2(x)} + \int_{h_1+h_2}^{z}\frac{dx}{A_3(x)}\right]dz. \tag{4.12}$$

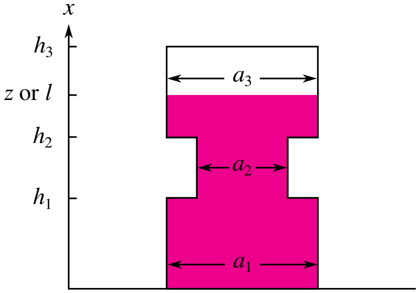

Figure 4.3: Illustration of the membrane profile with a barbell-shaped configuration.

In this investigation, as noted earlier, uniformity of membrane thickness is maintained across all segments. On the other hand, the segment widths denoted as $a_1(x)$, $a_2(x)$, and $a_3(x)$, change. This causes the membrane profiles to change. Therefore, the segment widths represent the cross-sectional areas and can be used to formulate wicking times

$$t_1(l) = \xi_{\mathrm{eff}}\int_0^l a_1(z)\left\{\int_0^z \frac{dx}{a_1(x)}\right\}dz, \tag{4.13a}$$

$$t_2(l) = \xi_{\mathrm{eff}}\int_{h_1}^l a_2(z)\left\{\int_0^{h_1} \frac{dx}{a_1(x)} + \int_{h_1}^{z}\frac{dx}{a_2(x)}\right\}dz, \tag{4.13b}$$

$$t_3(l) = \xi_{\mathrm{eff}}\int_{h_1+h_2}^l a_3(z)\left\{\int_0^{h_1} \frac{dx}{a_1(x)} + \int_{h_1}^{h_1+h_2}\frac{dx}{a_2(x)} + \int_{h_1+h_2}^{z}\frac{dx}{a_3(x)}\right\}dz. \tag{4.13c}$$

The wicking time in a membrane with three segments can be calculated as the sum of the wicking times for each segment, i.e., $t = t_1(h_1) + t_2(h_1 + h_2) + t_3(l)$. This model can be extended to calculate the wicking time in a membrane with n segments as $t = t_1(h_1) + t_2(h_1 + h_2) + t_3(h_1 + h_2 + h_3) + ... + t_n(l)$. To achieve $t_n(l)$ as the wicking time for the nth layer, $H_n = \sum_{m=0}^{n} h_m$ is defined as the cumulative length of n layers, where $H_0 = h_0 = 0$. Consequently, it can be written

$$t_n(l) = \xi_{\text{eff}} \int_{H_{n-1}}^{l} a_n(z) \left\{ \left(\sum_{m=1}^{n-1} \int_{H_{m-1}}^{H_m} \frac{dx}{a_m(x)} \right) + \int_{H_{n-1}}^{z} \frac{dx}{a_n(x)} \right\} dz. \tag{4.14}$$

Using the developed single-phase methodology, it is possible to predict the wicking time for a single-passage membrane consisting of multiple segments with arbitrary cross-sections. A notable advantage of this approach is its simplicity compared to other methods that require the use of a mesh and the numerical solution of differential equations. Assuming that the determination of this integral is not complex, the main challenge is to find the wicking coefficient (ξ_{eff}).

4.1.3 Determination of wicking coefficients

For the analysis of fluid propagation in a straight membrane, the wicking model provides Eq. (4.7), expressed as $t_1 = \xi_{\text{eff}} l^2/2$, where the wicking coefficient (ξ_{eff}) is defined as $\mu\varepsilon/(K\Delta p_{\text{c}})$, with $\Delta p_{\text{c}} = 2\gamma_{\text{LG}} \cos\theta / r_{\text{eff}}$. Using data from type A and type B membranes and considering water as the wetting fluid (see section 3.3), the wicking coefficients for type A and type B membranes are 1.05×10^5 and 1.41×10^5 s m^{-2}, respectively. This determination of the wicking coefficient is based on micro-scale characterization techniques used for macro-scale modeling, utilizing the concept of bottom-up homogenization. Alternatively, wicking coefficients can be determined experimentally. By conducting wicking experiments on straight membranes, as shown in Figure 3.7a and eI (samples 3 and 6), the variation of wicking length over time can be observed, as explained in section 3.2.3. Using Gnuplot 5.0 patchlevel 5 [98], Eq. (4.7) ($t_1 = \xi_{\text{eff}} l^2/2$) is fitted to the experimental data. This yields a wicking coefficient of 1.35×10^5 s m^{-2} for the membrane in Figure 3.7a. In addition, the arithmetic mean of the wicking coefficients is determined to be $1.22 \times 10^5\ \mathrm{s\,m^{-2}}$ for samples 3 and 6 in Figure 3.7eI. In this section, the elucidation of the wicking coefficient determination has been presented through two different approaches: i) computational, depending on the availability of microstructural evaluation, and ii) experimental, depending on the availability of experimental data. It is noteworthy that the wicking coefficients determined by the two methods are in the same order of magnitude and close to each other. Any differences are due to the different nature of the CN membranes and, additionally, to the neglect of the influence of the backing card in the first method. Since experimental data are readily available, the wicking coefficients derived from the second method are used for further investigation in this chapter. Figure 4.4 shows the experimental wicking data for the *UniSart® CN 140 backed* membrane and the fitting function used to calculate the wicking coefficient.

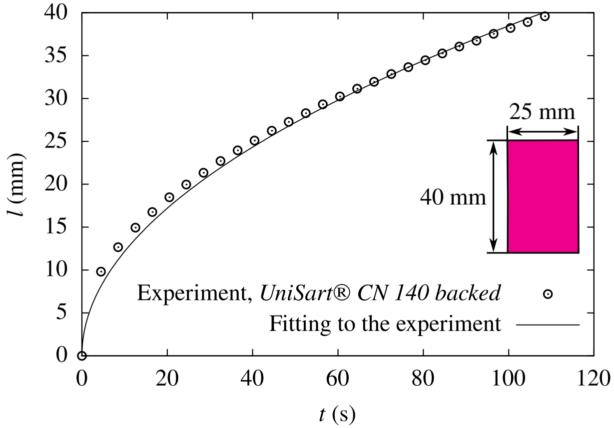

Figure 4.4: Experimental results and the fitted function for wicking in a straight membrane.

4.2 Influence of geometry on wicking in single-passage membranes

This section focuses on wicking behavior within single-passage membranes with variations in their cross-sectional areas. These variations can manifest as changes in membrane width along the flow path. Because single-passage membranes lack branching structures, such as bifurcations, they cannot offer alternative routes for the wicking fluid. Consequently, the fluid traverses a single path from the inlet to the opposite end of the membrane. A comprehensive investigation of wicking in multi-branch membrane profiles, characterized by the presence of multiple fluid flow paths, will be presented in chapter 5.

4.2.1 Wicking in hexagonal and sand timer-shaped membranes

Figure 4.5 depicts the temporal evolution of the fluid front position for hexagonal and sand timer-shaped membranes. These membranes have a length of 40 mm, varying from the narrowest width of 15 mm to the widest width of 25 mm. Water

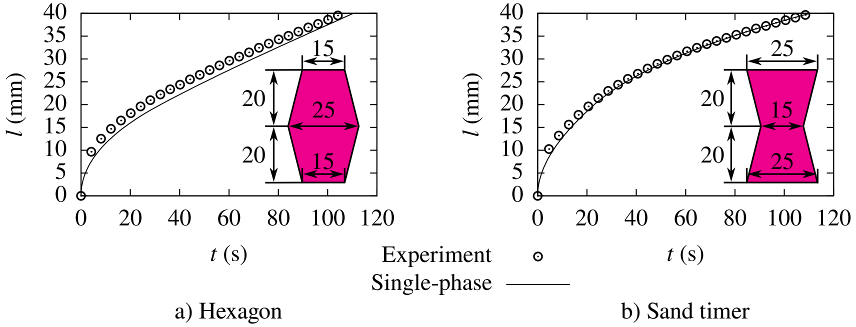

a) Hexagon

b) Sand timer

Figure 4.5: Temporal evolution of meniscus position using the single-phase approach and experimental data for a) hexagonal and b) sand timer-shaped configurations. The inset figures show the dimensions of each profile in millimeters.

is used as the wetting fluid. The results of the single-phase model are compared with experimental data, demonstrating that the wicking model accurately predicts the wicking behavior for both membrane configurations.

To perform a design study and better understand the effect of converging and diverging segments on wicking behavior, hexagonal and sand timer profiles are generated with different ratios of the first segment to the total membrane length. A nondimensionalization analysis is then performed. The total wicking time of the straight test strip is chosen as the scale, resulting in t_1 from Eq. (4.13a) and t_2 from Eq. (4.13b) being divided by $t_{\text{total, straight}} = \xi_{\text{eff}} h_1^2/2$. The dimensionless time is then plotted against the ratio of the wicking length to the total membrane length in Figure 4.6a. The gray line represents the wicking time of the straight membrane, while the red and blue curves correspond to the hexagonal and sand timer-shaped profiles, respectively. Since the wicking processes in all profiles are compared to the reference straight test strip, the graph remains independent of the membrane material and the fluid properties.

In the legend, the symbol h_1/H represents the normalized length of the first segment, defined as the ratio of its length (h_1) to the total membrane length ($H = 40\,\text{mm}$). Schematic representations of the membrane profiles are provided for reference. All hexagonal profiles have the same width of 15 mm at both ends. This value is 25 mm for sand timer-shaped profiles.

The dimensionless analysis indicates that for profiles with equal widths at the beginning and end, if half or more of the membrane profile consists of a diverging segment, the resulting wicking time will be longer than that of a straight membrane. Conversely, if the membrane has a predominantly converging shape for more than half of its length, the wicking time will decrease. Moreover, the diagram shows a common termination point when the diverging (or converging) parts of the hexagonal and sand timer-shaped profiles are of equal length. In essence, only the length of each segment affects the final wicking time, not the arrangement of the diverging and converging segments.

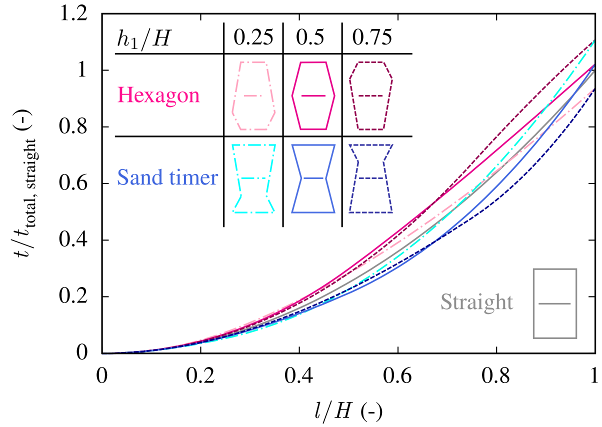

a)

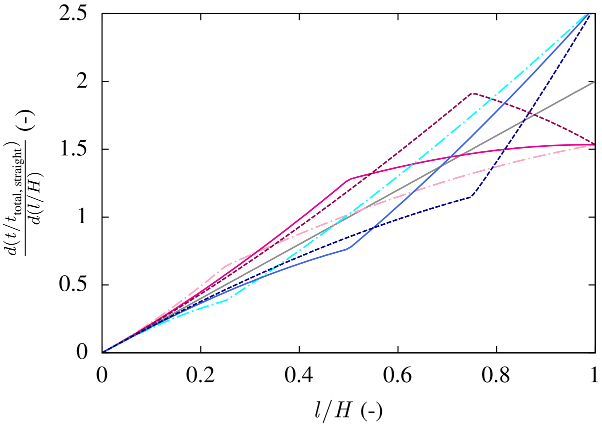

b)

Figure 4.6: Visualization of a) dimensionless wicking time and b) its derivative, comparing the hexagonal and sand timer-shaped profiles with the reference of a straight membrane (indicated by the gray line). The legend includes inset figures with schematics of each profile.

In addition to plotting the dimensionless time, its derivative is also plotted in Figure 4.6b to highlight variations in wicking time. Note that the slope of each curve changes as the cross-section changes. A higher slope in this graph indicates a lower wicking velocity. Consequently, this graph provides an estimate of the influence of shape on capillary flow velocity. The decrease in wicking velocity caused by diverging parts and the increase in wicking velocity caused by converging parts are evident. In particular, the fluid flow in the first segment of the hexagonal profile (diverging segment) is observed to be slower compared to the fluid flow in the first segment of the sand timer-shaped profile (converging segment). This observation is also evident in the second segment of the sand timer-shaped profile, indicating a slower fluid propagation in the second segment compared to the first.

Furthermore, the graph demonstrates that by altering the length of each segment, the flow velocity can be effectively adjusted in different regions, including the test and control line zones. This adjustment is crucial because one of the design criteria for lateral flow assays (LFAs) is the wicking velocity at the test line (TL). At $l/H \approx 0.7$, the wicking velocities through hexagonal and sand timer-shaped profiles with $h_1/H = 0.5$ are nearly identical to that of the straight membrane. Therefore, if the TL is inserted at 0.7 of the total length, the wicking time is much shorter for the sand timer-shaped profile despite the same wicking velocity. When the TL is inserted at $l/H = 0.8$ for all h_1/H, the fluid passes through the cross-sectional variation of the hexagonal and sand timer-shaped profiles. It is observed that for all these profiles, with a total length of 40 mm, a minimum width of 15 mm and a maximum width of 25 mm, the wicking velocity falls within the range of LFA velocities as reported in [60]. Consequently, with a TL width of 1 mm, the residence time is within the design range (see section 2.4.3).

Erickson and Park [99] performed numerical simulations using the finite element method to investigate the wetting behavior of converging-diverging and diverging-converging capillaries. In contrast to the present work, a straight section separated the converging and diverging parts in their simulations, and they did not study porous media. Nevertheless, their findings align with the current results, as both studies identify capillary force as the driving force of the flow and viscous force as the resisting force.

4.2.2 Wicking in T-shaped membranes

The experiment on T-shaped membranes depicted in Figure 3.7eI was designed to investigate the effect of a sudden change in width, with this change occurring at the same length for all profiles. Additionally, T-shaped membranes (Figure 3.7eII) were examined to study the impact of cross-sectional changes at varying lengths. Individual liquid rise profiles over time for the T-shaped membranes are shown in Figures 4.7 and 4.8. The experimental data are represented by point symbols, while solid curves in corresponding colors depict the predictions of the single-phase model, as detailed in section 4.1.

Among all the membranes, only samples 3 and 6 in Figure 4.7 (and Figure 3.7eI) exhibit straight profiles. Fitting the experimental data of these two samples and using their arithmetic mean facilitated the determination of the coefficient ξ_{eff} in Eq. (4.7), as explained in section 4.1.3. The model shows a good agreement with the experimental data in Figure 4.7. Even though straight samples 3 and 6 possess different widths, 2 and 4 mm, respectively, their wicking behaviors exhibit a high degree of similarity. This resemblance is attributed to two main factors. Firstly, it is related to their matching microstructural characteristics. Secondly, in the context of porous membranes, the critical width of the membrane profile is 600 µm, beyond which the wicking velocity becomes independent of the width, as established by Hecht et al. [89]. Hong and Kim's study of the wicking process in straight membranes with cut and wax boundaries also supports the finding that the wicking velocity is not affected by the channel width in the case of cut boundaries [100]. Considering that samples 3 and 6 possess cut boundaries (as opposed to wax boundaries) and exceed the critical width, their wicking processes are nearly identical.

For the remaining samples, it is evident that expansion leads to a decrease in velocity in the subsequent segment, where the wicking velocity remains nearly

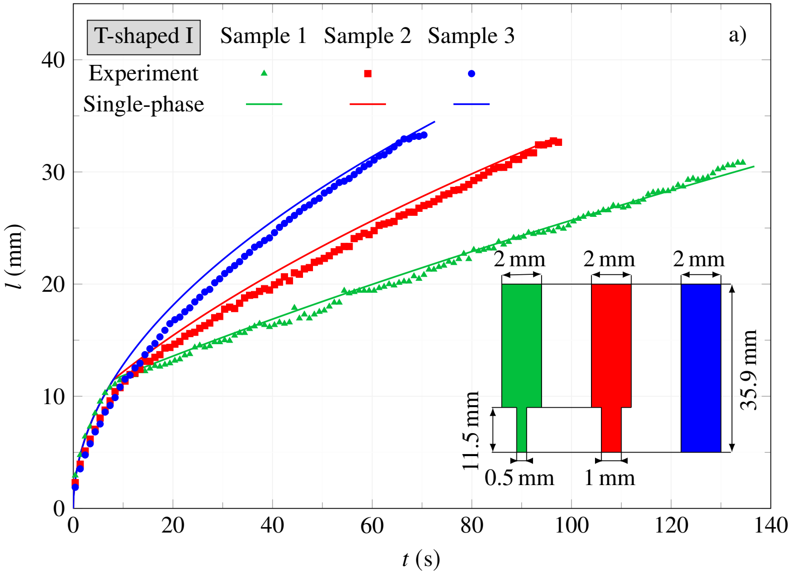

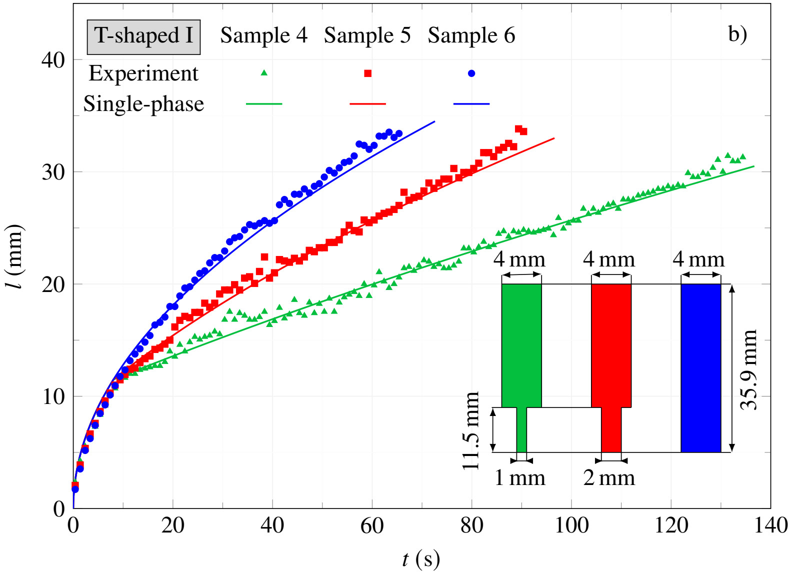

Figure 4.7: The wicking length over time in the T-shaped membranes I for the a) samples 1–3 and b) samples 4–6. Reproduced from [36], with the permission of AIP Publishing.

constant [101]. As discussed in [96], it is difficult for a thinner segment to supply sufficient liquid to a wider membrane. In other words, the source struggles to meet the increasing demand for fluid, resulting in a longer time for fluid propagation in the wider cross-section. Furthermore, the observation in samples 1 and 2, as well as in samples 4 and 5, reveals that the flow resistance decreases as the aspect ratio decreases, allowing the fluid to reach its final position more quickly.

Figure 4.8 illustrates the effect of variations in cross-sectional dimensions at different lengths on wicking time. In samples 1 and 4, 2 and 5, and 3 and 6, the length ratios of the second segment to the first segment are identical within each pair. Furthermore, the width ratios of the two segments are 4 for samples 1–3 and 2 for samples 4–6. As observed in Figure 4.8a, earlier liquid entry into the second segment results in a steeper slope of the wicking length, indicating a higher liquid velocity in this segment. Specifically, the wicking velocity in the second segment of sample 1 (green line) exceeds that of sample 2 (red line), causing the liquid front of sample 1 to overtake that of sample 2. As a result, considering a wicking length of 37.1 mm the overall wicking process in sample 2 is slower than in sample 1. Consistent with the findings of Azpiroz et al. [101], this work observes faster imbibition through the membrane with the shorter narrow segment (sample 1) compared to sample 2. Conversely, Fu et al. [102] reported that the liquid front has the longest transport time for the shortest first segment (sample 1). They used a shorter time interval in which the front of sample 1 had not yet reached its final position and could not overtake the liquid front of sample 2.

By increasing the length of the first segment, the liquid source for the second segment becomes more limited, resulting in increased flow resistance in the second segment and slower liquid propagation. Therefore, the flow velocity in the second segment of sample 3 is the lowest. However, the total wicking time for sample 3 is the shortest because the expansion of sample 3 occurs later than in samples 1 and 2, allowing faster flow in a longer straight channel (30.8 mm).

A similar interpretation applies to Figure 4.8b, where the liquid front of sample 4 overtakes that of sample 5, but not that of sample 6. The only difference from samples 1–3 is that the first segment is wider, which allows a greater flow rate

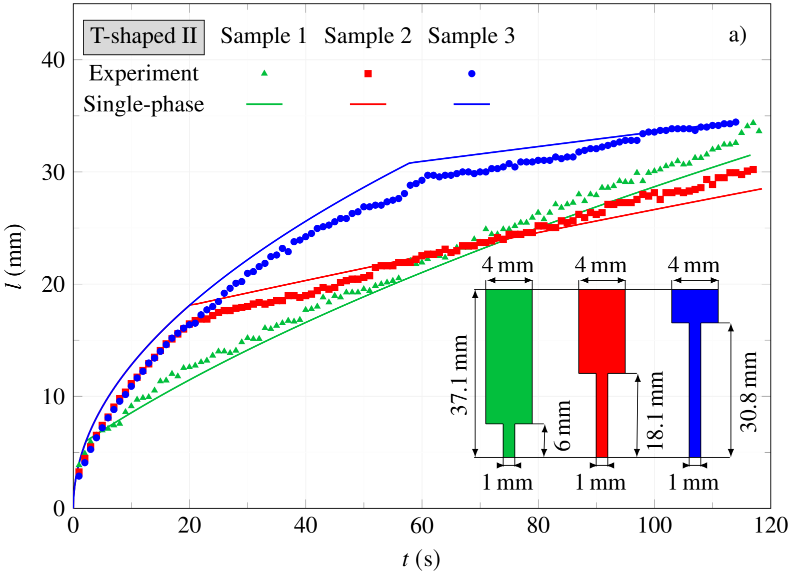

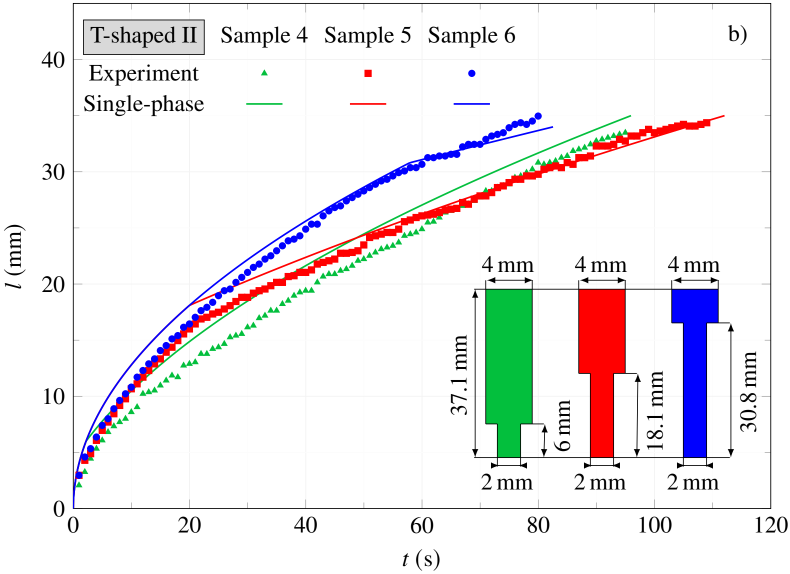

Figure 4.8: The wicking length over time in the T-shaped membranes II for the a) samples 1–3 and b) samples 4–6. Reproduced from [36], with the permission of AIP Publishing.

through the first segment and reduces the problem of a limited source for the second segment. Consequently, the changes in the slope of liquid propagation between the first and second segments of samples 4–6 are not as pronounced as those of samples 1–3. In essence, a reduction in the aspect ratio of an expansion is associated with an increase in wicking velocity.

It is noteworthy that the coefficient ξ_{eff} is derived from the wicking process of straight membranes in the experiment with T-shaped membrane I. The larger deviation between experimental and modeling results for T-shaped membrane II, especially for sample 4, can be attributed to errors associated with the transfer of the constant ξ_{eff} from a separate video with different zoom and exposure values. An additional reason for this deviation in sample 4 was the challenge of determining the liquid front.

In summary, expansion in different membrane profiles reduces the wicking velocity, and all slopes of liquid propagation in the second segments are lower than that of the straight membrane. This indicates that the wicking process in T-shaped membranes slows down with expansion, in contrast to the behavior observed in straight membranes. Furthermore, Shou et al. [96] previously demonstrated that an expansion positioned in the middle of the membrane length results in the slowest wicking. The current study shows that expansions below this critical length lead to higher velocities in the second segment, thereby facilitating a faster wicking process.

4.2.3 Wicking in barbell-shaped membranes

The single-phase approach can effectively capture the influence of multi-segment channels, such as those in a barbell-shaped membrane where each segment maintains a constant width. The wicking model is applied to a barbell-shaped membrane in Figure 4.3 where the dimensions a_1, a_2, and a_3 are 25, 15, and 25 mm, and h_1, h_2, and h_3 are 15, 10, and 15 mm. The resulting wicking behavior is then compared to the experimental data shown in Figure 4.9.

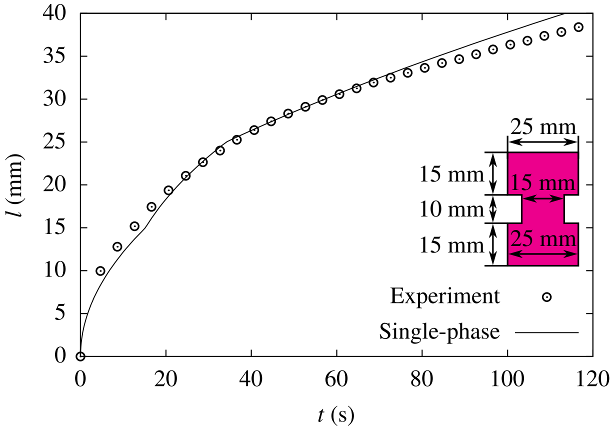

Figure 4.9: The wicking curve of the single-phase model for the barbell-shaped membrane compared with experimental data.

The barbell membrane consists of three straight segments, each of which has a different wicking function. Due to the reduced width of the second segment, the wicking velocity increases. However, upon entering the third segment, the fluid flow slows down. In contrast to the smooth flow observed for membranes with straight, hexagonal, or sand timer-shaped profiles, the single-phase model reveals a non-smooth motion of the fluid in the barbell-shaped profile. This is manifested by distinct knees in the wicking curve, which accurately reflects the wicking behavior observed in the experiment.

In this section, various membrane profiles with single-passage fluid flow were investigated to examine the influence of geometric changes on the wicking process. The model is adaptable to other membrane shapes and multi-segment configurations. By defining a specific objective, such as achieving a desired flow velocity for sensitivity enhancement, the developed model can be used to determine the necessary geometry to achieve that objective.

4.3 Sensitivity analysis

This section systematically explores fundamental processes in lateral flow assays (LFAs) through the application of a convection-diffusion-reaction model. Following the introduction of the model, an investigation is conducted to determine the optimal position for printing the test line (TL) on membranes. Test sensitivities are then derived for membranes with different characteristics. Sensitivity analysis is a valuable tool for improving the overall sensitivity of diagnostic assays.

4.3.1 Convection-diffusion-reaction model

As discussed in section 2.4.7, enhancing sensitivity in LFAs presents several challenges, including the transition from qualitative to quantitative signal intensity. This necessitates an examination of the temporal and spatial alterations in all species within LFAs by different processes, namely convection, diffusion, and reaction. In this regard, a 1D mathematical model, as presented in the literature [103–105] and validated by experimental data in these studies, is employed in this work. The model allows for a comprehensive understanding of the temporal and spatial dynamics of all components within LFAs, facilitating the evaluation of device performance under various operating conditions.

The principle of LFAs is explained in section 2.4.1. Excluding the sample pad, the conjugate pad, and the absorbent pad, and considering the CN membrane as the only porous medium, the following set of equations represents the chemical reactions taking place in this hypothetical test strip

$$\mathrm{A}+\mathrm{P} \underset{k_{\mathrm{d1}}}{\overset{k_{\mathrm{a1}}}{\rightleftarrows}} \mathrm{PA} \;\Rightarrow F_{\mathrm{PA}} = k_{\mathrm{a1}}[\mathrm{A}][\mathrm{P}] - k_{\mathrm{d1}}[\mathrm{PA}], \tag{4.15a}$$

$$\mathrm{A}+\mathrm{R} \underset{k_{\mathrm{d2}}}{\overset{k_{\mathrm{a2}}}{\rightleftarrows}} \mathrm{RA} \;\Rightarrow F_{\mathrm{RA}} = k_{\mathrm{a2}}[\mathrm{A}][\mathrm{R}] - k_{\mathrm{d2}}[\mathrm{RA}], \tag{4.15b}$$

$$\mathrm{R}+\mathrm{PA} \underset{k_{\mathrm{d}3}}{\overset{k_{\mathrm{a}3}}{\rightleftarrows}} \mathrm{RPA} \quad \Rightarrow F_{\mathrm{RPA1}} = k_{\mathrm{a}3}[\mathrm{R}][\mathrm{PA}] - k_{\mathrm{d}3}[\mathrm{RPA}], \tag{4.15c}$$

$$\mathrm{P}+\mathrm{RA} \underset{k_{\mathrm{d}4}}{\overset{k_{\mathrm{a}4}}{\rightleftarrows}} \mathrm{RPA} \quad \Rightarrow F_{\mathrm{RPA2}} = k_{\mathrm{a}4}[\mathrm{P}][\mathrm{RA}] - k_{\mathrm{d}4}[\mathrm{RPA}]. \tag{4.15d}$$

The chemical reaction between the analyte and the labeled detector antibody (Eq. (4.15a)) occurs throughout the test strip while Eqs. (4.15b) - (4.15d) describe the other chemical reactions that can only occur on the test line (TL) due to the immobilized capture antibody.

In Eq. (4.15), each reaction is defined by both an association rate constant (k_{a}) and a dissociation rate constant (k_{d}). Additionally, the rate of formation (F) is given for each product. This factor is influenced by k_{a} and k_{d} as well as the concentrations of the elements involved in the reaction. Specifically, [A], [P], [PA], [RA], and [RPA] denote the concentrations of analyte, detector antibody, analyte-detector antibody complex, capture antibody-analyte complex, and capture antibody-analyte-detector antibody complex, respectively.

The governing set of differential equations for the transport of different species within LFAs is derived from the mass conservation principle. It describes the temporal and spatial evolution of their concentrations, considering diffusion, convection, and reaction terms as [35]

$$\frac{\partial[\mathrm{A}]}{\partial t} = D_{\mathrm{A}}\frac{\partial^2[\mathrm{A}]}{\partial x^2} - U\frac{\partial[\mathrm{A}]}{\partial x} - F_{\mathrm{PA}} - F_{\mathrm{RA}}, \tag{4.16a}$$

$$\frac{\partial[\mathrm{P}]}{\partial t} = D_{\mathrm{P}}\frac{\partial^2[\mathrm{P}]}{\partial x^2} - U\frac{\partial[\mathrm{P}]}{\partial x} - F_{\mathrm{PA}} - F_{\mathrm{RPA2}}, \tag{4.16b}$$

$$\frac{\partial[\mathrm{PA}]}{\partial t} = D_{\mathrm{PA}}\frac{\partial^2[\mathrm{PA}]}{\partial x^2} - U\frac{\partial[\mathrm{PA}]}{\partial x} + F_{\mathrm{PA}} - F_{\mathrm{RPA1}}, \tag{4.16c}$$

$$\frac{\partial[\mathrm{RA}]}{\partial t} = F_{\mathrm{RA}} - F_{\mathrm{RPA2}}, \tag{4.16d}$$

$$\frac{\partial[\mathrm{RPA}]}{\partial t} = F_{\mathrm{RPA1}} + F_{\mathrm{RPA2}}, \tag{4.16e}$$

where D represents the molecular diffusion coefficient of each element and U is the average wicking velocity. Before wicking, an initial amount of immobilized capture antibody is present on the TL to form RA and RPA during wicking. Therefore, the concentration of the capture antibody can be expressed as

$$[\mathrm{R}] = [\mathrm{R}]_{\mathrm{initial}} - [\mathrm{RA}] - [\mathrm{RPA}]. \tag{4.17}$$

Eqs. (4.16) and (4.17) illustrate the convection-diffusion-reaction framework to elucidate the evolution of concentrations for all components during wicking. The former embodies a set of partial differential equations, which in this investigation are approached in conjunction with the latter via the finite difference approach (see section 2.5.2). This requires the specification of initial and boundary conditions. The initial concentration of the capture antibody should be known because the test line is applied to the CN membrane prior to wicking. On the other hand, the initial concentrations of all other components remain uniformly zero ($[\mathrm{A}] = [\mathrm{A}] = [\mathrm{PA}] = [\mathrm{RA}] = [\mathrm{RPA}] = 0$) because the CN membrane is not exposed to the sample solution. The boundary conditions for the concentration at the inlet boundary include a fixed amount of analyte ($[\mathrm{A}]_{\mathrm{inlet}}$) and a constant value of labeled detector antibody ($[\mathrm{P}]_{\mathrm{inlet}}$) when the membrane is attached to a liquid reservoir. Furthermore, the fully developed conditions are assumed to be reached at the outlet side. These conditions can be expressed as

$$\text{at the inlet:} \qquad [\mathrm{A}] = [\mathrm{A}]_{\mathrm{inlet}},\ [\mathrm{P}] = [\mathrm{P}]_{\mathrm{inlet}},\ [\mathrm{PA}]_{\mathrm{inlet}} = 0, \tag{4.18a}$$

$$\text{at the outlet:} \qquad \frac{\partial [\mathrm{A}]}{\partial x} = \frac{\partial [\mathrm{P}]}{\partial x} = \frac{\partial [\mathrm{PA}]}{\partial x} = 0. \tag{4.18b}$$

To solve these equations using the finite difference method (FDM), it is necessary to discretize both the length of the CN membrane, which constitutes the domain, and the total wicking time. As an illustration, the discretization of the temporal evolution of [A] based on Eq. (4.16a) is expressed as

$$[\mathrm{A}]_i^{(n+1)} = [\mathrm{A}]_i^{(n)} + \Delta t \left\{ D_{\mathrm{A}} \frac{[\mathrm{A}]_{i+1}^{(n)} - 2[\mathrm{A}]_i^{(n)} + [\mathrm{A}]_{i-1}^{(n)}}{(\Delta x)^2} - U \frac{[\mathrm{A}]_{i+1}^{(n)} - [\mathrm{A}]_i^{(n)}}{\Delta x} - F_{\mathrm{PA},\,i}^{(n)} \right\}, \tag{4.19}$$

where (n) represents the time step, indicating the discrete time points. The index i is the index of the computational cell along the spatial domain, indicating the discrete points within the domain. The term Δt is the temporal discretization, representing the size of the time steps. The term Δx is the spatial discretization, representing the size of the spatial intervals between computational cells along the domain. It is important to note that this method is an explicit algorithm, as it establishes the equations governing the system at the current time (n) and allows the computation of the system state at the subsequent time step $(n+1)$. Since all concentrations throughout the domain are known at each time step using FDM, quantification of the color signal becomes feasible, allowing evaluation of the LFA performance.

Various definitions of the color signal have been proposed in the literature. In the study by Qian and Bau [103], the color signal associated with the test line (TL) is formulated as [P]+[PA]+[RPA] because P contains colored particles. In the current investigation, the definition of the color signal is consistent with the formulation proposed by Liu et al. [105]. Their rationale assumes that the effective signal within the TL correlates with the total concentration of accumulated RPA in that region. Consequently, the detection signal in the TL is quantified by the average concentrations of RPA. This quantification is expressed by integrating the local RPA concentrations over the TL width, denoted as

$$CS = \frac{1}{x_2 - x_1} \int_{x_1}^{x_2} [\mathrm{RPA}]dx, \tag{4.20}$$

where CS is the color signal, and x_1 and x_2 are the integration limits along the spatial domain, i.e., the beginning and end of the TL.

4.3.2 Optimal test line location

In this section, the temporal evolution of [A], [P], and [PA] is studied, with special emphasis on the reaction preceding the printing of the test line. During this stage, only the reversible reaction between A and P (Eq. (4.15a)) takes place in the initial absence of R. Consequently, modifications to the governing equations for [A], [P], and [PA] in this pre-test line stage are introduced as

$$\frac{\partial [\mathrm{A}]}{\partial t} = D_{\mathrm{A}} \frac{\partial^2 [\mathrm{A}]}{\partial x^2} - U \frac{\partial [\mathrm{A}]}{\partial x} - F_{\mathrm{PA}}, \tag{4.21a}$$

$$\frac{\partial [\mathrm{P}]}{\partial t} = D_{\mathrm{P}} \frac{\partial^2 [\mathrm{P}]}{\partial x^2} - U \frac{\partial [\mathrm{P}]}{\partial x} - F_{\mathrm{PA}}, \tag{4.21b}$$

$$\frac{\partial [\mathrm{PA}]}{\partial t} = D_{\mathrm{PA}} \frac{\partial^2 [\mathrm{PA}]}{\partial x^2} - U \frac{\partial [\mathrm{PA}]}{\partial x} + F_{\mathrm{PA}}. \tag{4.21c}$$

The optimization objective is to determine the optimal position of the TL on the membrane where the concentration of PA peaks. In this way, when R is introduced to the membrane on the TL, the production of RPA and consequently the color signal, i.e., test sensitivity, can be maximized. Essentially, the TL must be positioned so that when the mixture containing A, P, and PA enters, it reaches the maximum [PA]. By positioning the TL farther from the beginning, there is more time and space for the reaction between the analyte and the detection antibody to form PA. Since no PA is initially present, the maximum [PA] corresponds to the chemical equilibrium of Eq. (4.15a). At chemical equilibrium, where [PA] no longer changes with time or position ($\partial[\mathrm{PA}]/\partial t = \partial^2[\mathrm{PA}]/\partial x^2 = \partial[\mathrm{PA}]/\partial x = 0$), Eq. (4.21c) implies that the rate of PA formation is zero ($F_{\mathrm{PA}} = 0$). Using the definition of F_{PA} from Eq. (4.15a), and incorporating $[\mathrm{A}]_{\mathrm{eq}} = [\mathrm{A}]_{\mathrm{inlet}} - [\mathrm{PA}]_{\mathrm{eq}}$ and $[\mathrm{P}]_{\mathrm{eq}} = [\mathrm{P}]_{\mathrm{inlet}} - [\mathrm{PA}]_{\mathrm{eq}}$, a quadratic equation is obtained

$$k_{\mathrm{a1}} [\mathrm{A}]_{\mathrm{eq}} [\mathrm{P}]_{\mathrm{eq}} - k_{\mathrm{d1}} [\mathrm{PA}]_{\mathrm{eq}} = 0 \Rightarrow$$

$$k_{\mathrm{a1}} \left([\mathrm{A}]_{\mathrm{inlet}} - [\mathrm{PA}]_{\mathrm{eq}}\right) \left([\mathrm{P}]_{\mathrm{inlet}} - [\mathrm{PA}]_{\mathrm{eq}}\right) - k_{\mathrm{d1}} [\mathrm{PA}]_{\mathrm{eq}} = 0 \Rightarrow$$

$$\underbrace{k_{\mathrm{a1}}}_{\mathcal{A}} [\mathrm{PA}]_{\mathrm{eq}}^2 + \underbrace{\left\{-k_{\mathrm{d1}} - k_{\mathrm{a1}}\left([\mathrm{A}]_{\mathrm{inlet}} + [\mathrm{P}]_{\mathrm{inlet}}\right)\right\}}_{\mathcal{B}} [\mathrm{PA}]_{\mathrm{eq}} + \underbrace{k_{\mathrm{a1}} [\mathrm{A}]_{\mathrm{inlet}} [\mathrm{P}]_{\mathrm{inlet}}}_{\mathcal{C}} = 0, \tag{4.22}$$

with an analytical solution for the equilibrium concentration of the analyte-detector antibody complex ($[\mathrm{PA}]_{\mathrm{eq}}$), since all terms $\mathcal{A}$, $\mathcal{B}$, and $\mathcal{C}$ are known. However, achieving equilibrium typically takes considerable time, leading to potential inconveniences such as an excessively long membrane before reaching the TL. To address this, Ragavendar and Anmol in [106] advocated that 90% of $[\mathrm{PA}]_{\mathrm{eq}}$ should be considered as the optimal concentration ($[\mathrm{PA}]_{\mathrm{optimum}}$) for entering the TL, formulated as

$$[\mathrm{PA}]_{\mathrm{optimum}} = 0.9[\mathrm{PA}]_{\mathrm{eq}} = 0.9\frac{-\mathcal{B}-\sqrt{\mathcal{B}^2-4\mathcal{A}\mathcal{C}}}{2\mathcal{A}}. \tag{4.23}$$

Given the known $[\mathrm{PA}]_{\mathrm{optimum}}$, solving the system of equations (4.21), which captures the spatial and temporal changes of the components in the LFA, allows one to determine when and where the $[\mathrm{PA}]_{\mathrm{eq}}$ and $[\mathrm{PA}]_{\mathrm{optimum}}$ can be achieved.

Figure 4.10 shows the equilibrium state reached during the wicking process of a 30 cm membrane inserted into a fluid reservoir, which is achieved after around 610 s. The inlet concentrations of the analyte and the labeled detector antibody are both set to 10 nM, while the association and dissociation coefficient rates are set to $k_{a1} = 1 \times 10^6\ \mathrm{M}^{-1}\,\mathrm{s}^{-1}$ and $k_{d1} = 1 \times 10^{-3}\ \mathrm{s}^{-1}$, respectively. A uniform diffusion coefficient of $1 \times 10^{-12}\ \mathrm{m}^2\,\mathrm{s}^{-1}$ is assigned to A, P, and PA, as determined in [106]. Within this simulation, an average wicking velocity of $U = 0.5\ \mathrm{mm\,s}^{-1}$

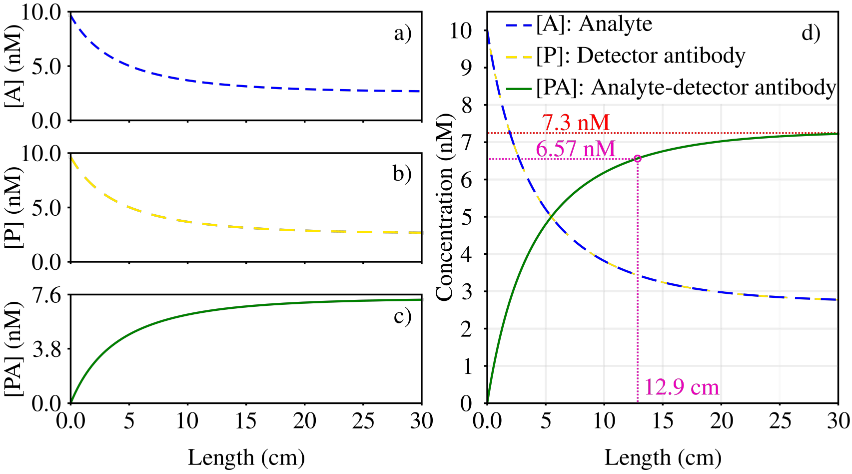

Figure 4.10: Spatial distribution of concentration profiles along the membrane length for a–c) individual components and d) all components. Additionally, the values of $[\mathrm{PA}]_{\mathrm{eq}}$ and $[\mathrm{PA}]_{\mathrm{optimum}}$ along with their corresponding lengths are depicted.

is implemented. Spatially, the simulation uses a resolution of $\Delta x = 10\,\mu\text{m}$, while temporally, a resolution of $\Delta t = 10\,\text{ms}$ is used.

Figure 4.10a–c shows the change in concentration along the membrane length for individual components, while Figure 4.10d presents a comprehensive view of all concentrations with the equilibrium and optimal concentrations of PA. It is observed that $[\text{PA}]_{\text{eq}}$ reaches 7.3 nM, requiring about 30 cm of membrane length. According to Eq. (4.23), the optimal concentration of [PA] is 6.57 nM, which can be reached at a distance of 12.9 cm from the beginning of the membrane. As discussed in previous sections (see sections 2.4.6 and 3.2.3), the length scales considered in this investigation indicate that the membrane length does not exceed 4 cm in industrial settings. Consequently, although Figure 4.10 shows an optimal X_{TL} value exceeding 4 cm for the specified configuration, placing the TL at such a distance is not feasible in real-world scenarios. Nevertheless, these values provide valuable insight into the spatial and temporal dynamics of this LFA.

Table 4.1 presents significant data regarding the optimal positioning of the TL within LFAs. The simulations remain consistent with the previous parameters, except for variations in analyte concentration at the inlet and average wicking velocity. These changes are made to assess the effect of these parameters on the optimal location of the test line. For various inlet concentrations of the target analyte ($[\text{A}]_{\text{inlet}}$), the table presents the optimal value of the analyte-detector antibody complex based on Eq (4.23). Additionally, the table provides insight into the optimal TL position and the time required for complete wetting of the TL over a range of average wicking velocities (U) from 0.1 to 0.5 $\text{mm}\,\text{s}^{-1}$.

For an identical $[\text{A}]_{\text{inlet}}$, as the flow velocity increases, the optimal X_{TL} tends to increase, implying a greater distance from the inlet, resulting in a longer t_{TL}. The results suggest that at identical wicking velocity, higher $[\text{A}]_{\text{inlet}}$ values result in a larger optimal X_{TL} and a longer t_{TL}. In particular, the escalation in optimal X_{TL} and t_{TL} from $[\text{A}]_{\text{inlet}}$ values of 1 to 5 nM is significantly larger than that from 5 to 10 nM. This insight sheds light on the optimal analyte concentration for a given assay, as an increased analyte concentration not only fails to enhance the optimization but also potentially induces the hook effect (see section 2.4.7).

Thus, this methodology can serve as a basis for optimizing TL positioning under different conditions by simply changing the input parameters.

Table 4.1: The optimal test line (TL) location with $D_\mathrm{A} = D_\mathrm{P} = D_\mathrm{PA} = 1 \times 10^{-12}\ \mathrm{m^2\,s^{-1}}$, $[\mathrm{P}]_\mathrm{inlet} = 10\,\mathrm{nM}$, $k_\mathrm{a1} = 1 \times 10^6\ \mathrm{M^{-1}\,s^{-1}}$, $k_\mathrm{d1} = 1 \times 10^{-3}\ \mathrm{s^{-1}}$, $\Delta x = 10\,\mathrm{\mu m}$, $\Delta t = 10\,\mathrm{ms}$.

$[A]_\mathrm{inlet}$ (nM)	$[\mathrm{PA}]_\mathrm{optimum}$ (nM)	U ($\mathrm{mm\,s^{-1}}$)	Optimal X_TL (cm)	t_TL (s)
1	0.811	0.1	2.174	231.44
		0.2	4.347	226.65
		0.3	6.520	224.41
		0.4	8.693	222.99
		0.5	10.865	221.92
5	3.83	0.1	2.548	272.14
		0.2	5.094	266.18
		0.3	7.640	263.41
		0.4	10.186	261.65
		0.5	12.732	260.35
10	6.57	0.1	2.577	275.82
		0.2	5.151	269.54
		0.3	7.726	266.67
		0.4	10.30	264.84
		0.5	12.875	263.46

4.3.3 Structure-sensitivity linkage

To perform a sensitivity analysis, the convection-diffusion-reaction model is integrated with the wicking model introduced in section 4.1.1 for a straight membrane profile at the macro-scale and different characteristics at the micro-scale.

For a straight membrane, the wicking velocity is derived from the wicking time (Eq. (4.7))

$$t = \frac{1}{2}\xi_{\text{eff}} l^2 \Rightarrow \frac{dt}{dl} = \xi_{\text{eff}} l \Rightarrow U(l) = \frac{1}{\xi_{\text{eff}} l}, \tag{4.24}$$

where ξ_{eff} is the wicking coefficient that can be calculated from microstructure simulation data, as shown for type A and type B membranes (see section 4.1.3). By calculating ξ_{eff} from microstructure simulation data and incorporating Eq. (4.24) into Eq. (4.16), the wicking model and the convection-diffusion-reaction model are coupled for membranes with different microstructural properties, facilitating the determination of their test sensitivities.

To study the influence of microstructural characteristics on the wicking coefficient, the methodology of Kunz et al. [24] is used. They established correlations between microstructural morphology and macroscopic material behavior, called structure-property linkage. They determined these relationships by creating about 400 porous microstructures with different geometric properties, where permeability and pore radius were expressed as functions of porosity and ligament radius. They generated synthetic porous structures with different porosities (83%, 85%, 87%, and 89%) and ligament radii, and then performed fluid flow simulations within the pore spaces of these structures to determine their permeabilities, as described in section 3.1.5. The permeability values obtained were then fitted to the general form of the Kozeny-Carman equation (Eq. (2.17)), yielding a geometry factor of $c = 15.7171$. They also calculated the mean pore radius of each generated medium, which showed a linear relationship within the data. Consequently, a linear function was selected, resulting in $r_{\text{p}} = \mathscr{A}\varepsilon + \mathscr{B}r_{\text{l}} + \mathscr{C}$ with $\mathscr{A} = 9.61415 \times 10^{-6}$ m, $\mathscr{B} = 3.17836$ and $\mathscr{C} = -8.15231 \times 10^{-6}$ m, where the pore radius r_{p} is a function of the porosity (ε) and the ligament radius (r_{l}). Using Eq. (3.2) in conjunction with Eq. (3.3), the effective pore radius was calculated. Then, by inserting all the data obtained from these equations into

Eq. (2.43), the wicking time was determined as a function of porosity, ligament radius, wetting properties, and membrane length [24]

$$t = \frac{1}{2} \times \boxed{\frac{15.7171(1-\varepsilon)^2(\mathscr{A}\varepsilon+\mathscr{B}r_{\mathrm{l}}+\mathscr{C})\left(1.98(\mathscr{A}\varepsilon+\mathscr{B}r_{\mathrm{l}}+\mathscr{C})+3.012r_{\mathrm{l}}\right)}{\varepsilon^2 r_{\mathrm{l}}^3}\frac{\mu}{2\gamma_{\mathrm{LG}}\cos\theta}} \times l^2, \tag{4.25}$$

where the box on the second line contains the expression for the wicking coefficient (ξ_{eff}). In this thesis, considering 61 porosities ranging from 83% to 89%, 51 ligament radii ranging from 0.35 to 0.85 µm, and water as the wicking fluid with the properties listed in Table 4.2, the ξ_{eff} values are calculated for 3111 membranes based on Eq. (4.25). Their corresponding total wicking times are then derived as shown in Figure 4.11 for a wicking length of 2 cm, which is a length relevant to LFA applications.

Table 4.2: Parameter values for the wicking time and sensitivity analysis of a straight LFA.

Parameter	Description	Value	From
μ	Viscosity of water	$10^{-3}\,\mathrm{kg\,m^{-1}\,s^{-1}}$	[24]
θ	Contact angle	50°	
γ_{LG}	Surface tension coefficient	$0.073\,\mathrm{N\,m^{-1}}$	
L	Membrane length	2 cm	[105]
k_{a}	All association coefficients	$10^{4}\,\mathrm{M^{-1}\,s^{-1}}$	
k_{d}	All dissociation coefficients	$10^{-7}\,\mathrm{s^{-1}}$	
D_{A}	Diffusion coefficient of A	$10^{-10}\,\mathrm{m^2\,s^{-1}}$	
D_{P}	Diffusion coefficient of P	$10^{-12}\,\mathrm{m^2\,s^{-1}}$	
D_{PA}	Diffusion coefficient of PA	$10^{-12}\,\mathrm{m^2\,s^{-1}}$	
$[\mathrm{A}]_{\mathrm{inlet}}$	Concentration of A at the inlet	100 nM	
$[\mathrm{P}]_{\mathrm{inlet}}$	Concentration of P at the inlet	3.67 nM	
$[\mathrm{R}]_{\mathrm{initial}}$	Initial concentration of R on the TL	1068 nM	

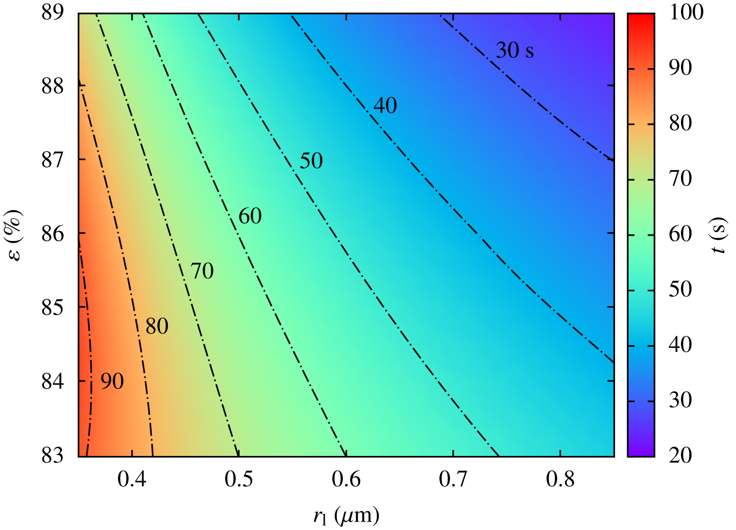

Figure 4.11: Using the information provided in Table 4.2, the total wicking time is calculated for a straight membrane with varying porosities and ligament radii. The contour plot visually represents the variations in wicking time, highlighted by isolines.

This contour plot effectively visualizes total wicking times as a function of porosity and ligament radius. Higher porosity and radius values correspond to faster wicking throughout the entire membrane length.

By substituting the wicking coefficient (ξ_{eff}) from Eq. (4.25) into Eq. (4.24), the wicking velocity can be expressed as a function of porosity, ligament radius, wetting properties, and length. This velocity serves as a crucial parameter in the convection-diffusion-reaction model (Eq. (4.16)). The model is employed in conjunction with the data presented in Table 4.2 to conduct numerical analyses on all 3111 membranes that have been previously examined in this section in terms of their wicking times. In these numerical studies, the TL is positioned from $0.5L$ to $0.65L$, corresponding to a TL width of 3 mm. The spatial resolution used for the numerical study is $\Delta x = 0.5\,\text{mm}$. The time step is computed according to the stability criteria [107] using $\Delta t = \min(\Delta t_{CFL}, 10\,\mathrm{ms})$, where $\Delta t_{CFL} = CFL \cdot \Delta x / U$, and CFL stands for the Courant number.

In CFD simulations, the Courant number indicates how information moves across grid cells in a given time. Particularly, a Courant number greater than one indicates that information is moving through multiple cells per time step, potentially leading to inaccuracies or divergences. To ensure stability and accuracy, a Courant number of 0.1 is chosen for this study. Since the mathematical model is unsteady, the equilibrium time for signal acquisition is set to 600 s, based on the findings of Liu et al. [105], which corresponds to the moment when the mathematical system reaches stability. Therefore, the signal intensities in this study are calculated using Eq. (4.20) at this time to determine the structure-sensitivity linkage, as shown in Figure 4.12a.

Instead of situating the membranes within a liquid reservoir, a boundary condition is imposed at the inlet to emulate the presence of a droplet. By executing 3111 simulations with this new boundary condition, the structure-sensitivity linkage can be investigated as a droplet traverses the membrane. This approach is more application-oriented compared to cases with a reservoir boundary condition, as it is more consistent with real-world scenarios where sample volumes are limited. Consequently, the initial values of $[\mathrm{A}]_{\mathrm{inlet}}$ and $[\mathrm{P}]_{\mathrm{inlet}}$, as shown in Table 4.2, are set to be nonzero only at the beginning of the simulations. Beginning with the second time step, these concentrations are set to zero. Despite the low concentrations at the inlet/initial stage, this condition symbolizes the presence of a liquid droplet, the so-called hypothetical droplet. The goal is to ensure consistency in the values applied to both the droplet and reservoir case studies. Figure 4.12b depicts the structure-sensitivity linkage for a membrane when a hypothetical droplet is introduced.

Comparing the contour plots in Figures 4.11 and 4.12, noticeable differences in the trend of the signal intensity can be observed in 4.12a. This discrepancy arises from the assumption in the inlet boundary condition that constant concentrations of analyte and detector antibody are maintained as the membrane interacts with a reservoir. Consequently, a shorter wicking time results in an earlier arrival of

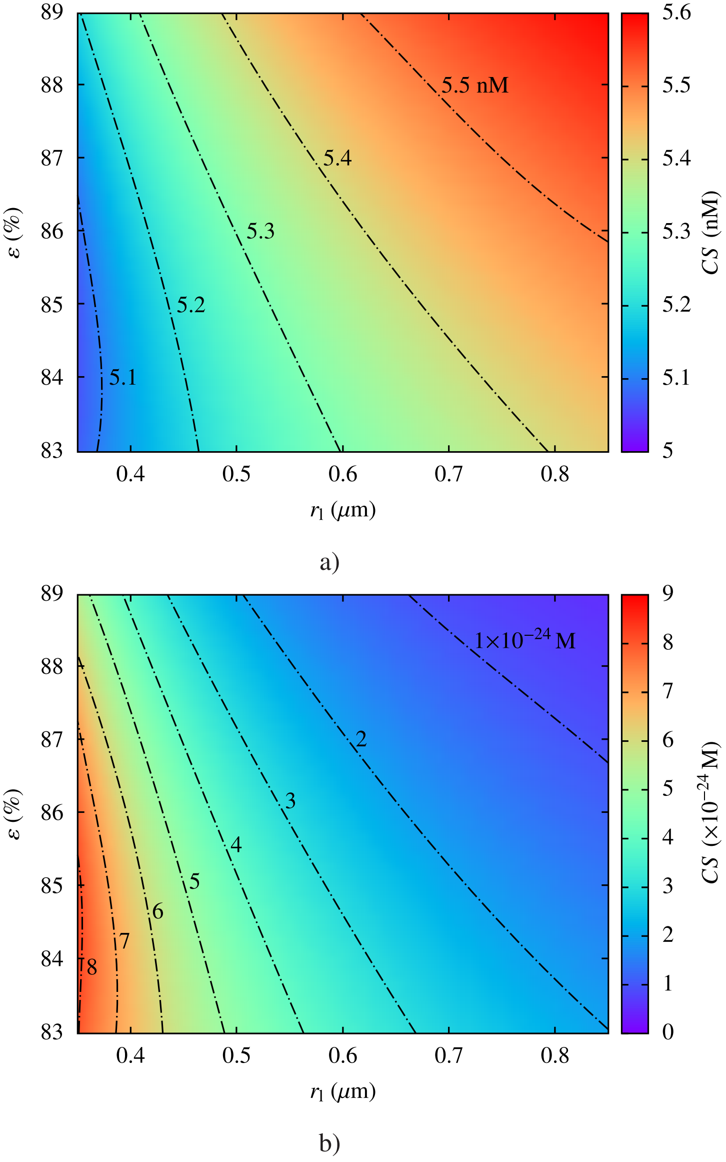

Figure 4.12: Using data from Table 4.2, the color intensity is determined for a straight membrane with different porosities and ligament radii at 600 s. The contour plots visually represent the color intensity variations, highlighted by isolines. In a) the membrane is exposed to a liquid reservoir, and in b) a droplet is applied to the membrane.

these components at the test line (TL), and the continued influx of analyte and detector antibody from the reservoir results in a higher RPA concentration at 600 s, thereby increasing sensitivity.

In contrast, when a hypothetical droplet is applied to the membrane, only a limited amount of analyte and detector antibody is introduced into the test, resulting in a much lower intensity at the TL at 600 s. The structure-intensity linkage shown in Figure 4.12b is derived for the small input values of $[\mathrm{A}]_{\mathrm{inlet}}$ and $[\mathrm{P}]_{\mathrm{inlet}}$, resulting in relatively small intensities. Nonetheless, the trend in this plot provides insight into the effect of porosity and ligament radius on signal intensity. As expected, lower porosities and ligament radii, which correlate with longer wicking times (i.e., slower wicking), allow for more time for the confined PA on the TL to react with R to form RPA, leading to higher intensities at slower wicking velocities. The use of droplets in LFAs instead of reservoirs is more typical and application-oriented. Transitioning from the hypothetical scenario to a real droplet scenario necessitates an augmentation of the input values for $[\mathrm{A}]_{\mathrm{inlet}}$ and $[\mathrm{P}]_{\mathrm{inlet}}$, yet the same trend persists.

By comparing the results of the convection-diffusion-reaction model with experimental investigations, Liu et al. [105] established a detection limit of 0.03 nM for signal intensity. This detection limit corresponds to the threshold observable by the naked eye. Consequently, all signal intensities shown in Figure 4.12a can be detected, while those shown in Figure 4.12b are below the detection limit. To observe a discernible color signal, a larger quantity of A and P is required when a droplet is applied to the membrane.

Another aspect to consider is the effect of diffusion on signal intensity. Analyzing the transport equations (Eqs. (4.16a)–(4.16c)), it becomes clear that the diffusion process influences the transport of A, P, and PA, and consequently the signal intensity. However, the question remains: to what extent? A dimensional analysis of the convection and diffusion terms within the governing equations reveals a magnitude-order ratio of UL/D, known as the Peclet number. The average wicking velocity (U) is typically in the range of 0.1 to 0.5 $\mathrm{mm\,s^{-1}}$ [60], and the length of a test strip (L) typically varies between 2 and 4 cm. By using the diffusion coefficients listed in Table 4.2, large Peclet numbers are obtained. This indicates that convection dominates over diffusion for species transport.

Although the effect of diffusion on signal intensity appears to be limited, an alternative approach is offered by the concept of the effective diffusion coefficient, as explained in [60]. Defined as $D_{\mathrm{eff}} = (\varepsilon/\tau_{\mathrm{eff}})D$, this concept involves the derivation of the ratio of porosity to tortuosity, which can be calculated using Eq. (3.6). To find the signal intensity for a membrane exposed to a liquid reservoir, this time the previous 3111 configurations are simulated using D_{eff}. The theoretical goal is to evaluate the effect of $\varepsilon/\tau_{\mathrm{eff}}$ on the signal intensity. However, the practical assessment of this effect remains challenging, as the signal intensities calculated using D_{eff} are very similar to those obtained using D (see Figure 4.12a). This result is consistent with the expected minimal effect of diffusion on signal intensity.

4.4 Summary

This chapter presents a comprehensive analysis of liquid transport in lateral flow assays (LFAs), integrating theoretical modeling and experimental investigations. A single-phase model is developed to elucidate the macro-scale wicking process. The model is validated through the employment of experimental data. The primary objective of this study is to examine the impact of geometric modifications in the membrane profile on wicking behavior. In pursuit of this objective, a range of membrane geometries is considered, including straight, hexagonal, sand timer-shaped, barbell-shaped, and T-shaped profiles. By focusing exclusively on geometric variations, the study deliberately excludes the effects of membrane-related parameters (e.g., permeability) and fluid-related parameters (e.g., viscosity). To account for these excluded parameters, the model is calibrated using experimental data obtained from straight membranes. This approach enables a comprehensive understanding of the wicking behavior in paper-based membranes with different cross-sectional configurations. The results demonstrate a strong correlation between the model predictions and experimental data. The findings highlight the significance of geometric considerations in the design of LFAs and provide a robust framework for future research aimed at optimizing assay performance.

The convection-diffusion-reaction model presented in this chapter represents a valuable tool for the systematic exploration and understanding of the fundamental processes underlying LFAs. This model addresses the challenge of quantitatively assessing signal intensity in LFAs by incorporating biochemical concentration characteristics, microstructural properties of the porous membrane, and wetting properties. By employing data-driven insights and elucidating the structure-sensitivity linkage, this comprehensive approach makes a substantial contribution to the ongoing efforts to enhance the sensitivity of diagnostic assays.

5 Macroscopic two-phase modeling of wetting in lateral flow assays[1]

Numerical investigations of the wicking process at the micro-scale can be performed using fully resolved porous media models. This approach requires the reconstruction of all the tiny pores within a porous membrane for CFD simulations. While feasible for small regions of interest, this method becomes impractical for analyzing wicking behavior across entire lateral flow assays (LFAs) with typical lengths of 2 to 4 cm. The primary challenge is the immense increase in the number of mesh cells required to model the entire pore space of such a large domain. Solving the governing equations (e.g., Stokes equation) with such numerous mesh cells becomes computationally expensive and time-consuming. To address this challenge in computational simulations of fluid propagation in LFAs, it becomes imperative to consider the domain as a porous zone.

In the previous chapter, a macro-scale single-phase model was developed to simulate liquid transport within axisymmetric LFAs with varying cross-sections and a singular flow path. While the model accurately represents wicking phenomena, its complexity increases with more complex geometries. In addition, any change in geometry requires a complete recalculation from the scratch. To overcome these limitations, a novel two-phase approach is proposed to simulate fluid

---

[1] The two-phase wicking model developed in this chapter is based on the work published in the peer-reviewed journal article by Jamshidi et al. [108]. Reproduced from “Geometric flow control in lateral flow assays: Macroscopic two-phase modeling” Physics of Fluids, November 2024; 36(11): 112108, with the permission of AIP Publishing.

flow through membranes at the macroscopic level. The main objective of this approach is to evaluate the influence of the membrane shape on the motion of the fluid front. This two-phase model provides a more versatile framework capable of simulating wicking in a range of membrane profiles, including the branched configurations commonly employed in multiplexed LFAs.

5.1 Two-phase wicking model

In the previous chapter, the model was based on a single-phase framework in which a wicking fluid (a liquid) enters and occupies the pore space. However, considering the scenario where the pore space is initially occupied by another fluid, such as air, the entry of a second fluid, such as water, results in the displacement of the first. In other words, an incumbent fluid is initially present within the pore space, while an invading fluid displaces it and subsequently occupies the void volume. In this section, a macro-scale two-phase model is introduced to elucidate this displacement, i.e., the wicking phenomenon in LFAs. The invading liquid, such as water or *Porefil®*, is referred to as the wetting phase (index w) due to its favorable interaction with the porous media, while the incumbent gas, such as air, is designated as the non-wetting phase (index n) due to its weaker interaction.

A key parameter, saturation (S), is introduced to distinguish between the phases. The saturation of a particular phase is defined as the volumetric fraction of the void space occupied by that particular phase [29]. Mathematically, the saturation of the phase α is expressed as

$$S_\alpha = \frac{\forall_\alpha}{\forall_\mathrm{p}} \qquad \alpha = \mathrm{n,\ w}, \tag{5.1}$$

where $\forall_\alpha$ represents the volume of the pore space occupied by the phase α (either wetting, denoted as w, or non-wetting, denoted as n), and $\forall_\mathrm{p}$ represents the total volume of the pore space. Since the entire void space is occupied by both phases, the saturation of each phase (denoted as S_n and S_w) is inherently in the range of zero to one, and the sum of the saturations of all the phases must equal one. This can be expressed mathematically as $S_\mathrm{n} + S_\mathrm{w} = 1$.

The two-phase approach in this section aims to model the wicking process that occurs within the membrane. The primary objective is to determine the spatial distribution of fluid saturation throughout the imbibition process. In the context of two incompressible and immiscible fluids in a porous medium, saturation values are employed to quantify the wetting state of the membrane. These values indicate whether the membrane is entirely wet, partially wet, or completely dry. Since both fluids, such as air and water, are considered in this model as continuous entities at the macro-scale, the fully saturated membrane corresponds to $S_\mathrm{n} = 0$ and $S_\mathrm{w} = 1$, while a dry membrane corresponds to $S_\mathrm{n} = 1$ and $S_\mathrm{w} = 0$. In fact, both saturations become nonzero simultaneously only at the interface of the two phases. By determining this evolving saturation field, the model effectively captures the motion of the liquid front within the membrane.

For two-phase flow in porous media involving incompressible and immiscible fluids, the saturation equation for each phase (α) is derived from the principle of mass conservation. This equation can be expressed as [109]

$$\varepsilon \frac{\partial S_\alpha}{\partial t} + \nabla \cdot \mathbf{u}_\alpha = q_\alpha \qquad \alpha = \mathrm{n},\ \mathrm{w}, \tag{5.2}$$

where ε denotes the porosity of the medium, $\mathbf{u}_\alpha$ the velocity vector of the phase α, and q_α the source/sink term. The velocity of each phase is governed by the extension of Darcy's law for two-phase flow as [109]

$$\mathbf{u}_\alpha = -\frac{k_{\mathrm{r}\alpha}\mathbf{K}}{\mu_\alpha} \left(\nabla p_\alpha - \rho_\alpha \mathbf{g} \right) \qquad \alpha = \mathrm{n},\ \mathrm{w}. \tag{5.3}$$

Compared to Darcy's law (Eq. (2.7)), two modifications are observed. The first change is the introduction of the term "relative permeability", denoted as $k_{\mathrm{r}\alpha}$. When single-phase flow is assumed, the Darcy equation uses absolute permeability. However, in the presence of two phases in a porous medium, their interactions affect each other's movement, resulting in the so-called phase permeability

($k_{r\alpha}\mathbf{K}$) being lower than the absolute permeability. The ratio of the relative permeability to the viscosity of the phase α is conventionally called the “mobility”, denoted as $\lambda_\alpha = k_{r\alpha}/\mu_\alpha$ [28]. The second modification concerns the consideration of the effect of gravity.

Capillary pressure is defined as the pressure difference arising across the interface between two immiscible fluids. This pressure difference can also be expressed mathematically as the difference between the pressure of the non-wetting phase and the pressure of the wetting phase, so $p_c = p_n - p_w$ [29].

The complete two-phase flow model is now displayed in the form of

$$\varepsilon\frac{\partial S_\alpha}{\partial t} + \nabla\cdot\mathbf{u}_\alpha = q_\alpha \qquad \alpha = \mathrm{n, w}, \tag{5.4a}$$

$$\mathbf{u}_\alpha = -\frac{k_{r\alpha}\mathbf{K}}{\mu_\alpha}\left(\nabla p_\alpha - \rho_\alpha \mathbf{g}\right) \qquad \alpha = \mathrm{n, w}, \tag{5.4b}$$

$$p_c = p_n - p_w, \tag{5.4c}$$

$$S_n + S_w = 1. \tag{5.4d}$$

For two-phase flow through porous media, only two variables among S_n, S_w, p_n, and p_w can be selected as independent unknowns. Different combinations of independent variables can be chosen to eliminate the remaining dependent variables, resulting in different mathematical formulations describing the same physical model. In this study, the formulation of non-wetting phase pressure and wetting phase saturation (p_n, S_w) is adopted for modeling immiscible two-phase flow. This choice implies that, according to Eq. (5.4c), the wetting phase pressure is related to the non-wetting pressure and the capillary pressure ($p_w = p_n - p_c$), and based on Eq. (5.4d), the non-wetting phase saturation is related to the wetting phase saturation ($S_n = 1 - S_w$). Using these relationships and incorporating Eq. (5.4b) into Eq. (5.4a), the governing equations for the two-phase flow model are obtained as [110]

$$-\varepsilon\frac{\partial S_{\mathrm{w}}}{\partial t}+\nabla\cdot\left(-\frac{k_{\mathrm{rn}}(S_{\mathrm{w}})\mathbf{K}}{\mu_{\mathrm{n}}}\left(\nabla p_{\mathrm{n}}-\rho_{\mathrm{n}}\mathbf{g}\right)\right)=q_{\mathrm{n}}, \tag{5.5a}$$

$$\varepsilon\frac{\partial S_{\mathrm{w}}}{\partial t}+\nabla\cdot\left(-\frac{k_{\mathrm{rw}}(S_{\mathrm{w}})\mathbf{K}}{\mu_{\mathrm{w}}}\left(\nabla p_{\mathrm{n}}-\nabla p_{\mathrm{c}}(S_{\mathrm{w}})-\rho_{\mathrm{w}}\mathbf{g}\right)\right)=q_{\mathrm{w}}. \tag{5.5b}$$

By summing Eqs. (5.5a) and (5.5b), it can be written

$$\nabla\cdot\left(-\frac{k_{\mathrm{rn}}(S_{\mathrm{w}})\mathbf{K}}{\mu_{\mathrm{n}}}\left(\nabla p_{\mathrm{n}}-\rho_{\mathrm{n}}\mathbf{g}\right)-\frac{k_{\mathrm{rw}}(S_{\mathrm{w}})\mathbf{K}}{\mu_{\mathrm{w}}}\left(\nabla p_{\mathrm{n}}-\nabla p_{\mathrm{c}}(S_{\mathrm{w}})-\rho_{\mathrm{w}}\mathbf{g}\right)\right)=q, \tag{5.6}$$

where q represents the total source/sink term, defined as $q=q_{\mathrm{n}}+q_{\mathrm{w}}$. In addition, the relative permeabilities and the capillary pressure are functions of S_{w}.

By using Eq. (5.2) for the wetting phase saturation and Eq. (5.6) for the pressure equation, the formulation of the flow of two incompressible immiscible fluids through porous media in the (p_{n}, S_{w}) representation can be expressed as

$$\varepsilon\frac{\partial S_{\mathrm{w}}}{\partial t}+\nabla\cdot\mathbf{u}_{\mathrm{w}}=q_{\mathrm{w}}, \tag{5.7a}$$

$$-\nabla\cdot\left[\mathbf{K}\left(\lambda_{\mathrm{n}}+\lambda_{\mathrm{w}}\right)\nabla p_{\mathrm{n}}\right]=q-\nabla\cdot\left[\mathbf{K}\left(\lambda_{\mathrm{n}}\rho_{\mathrm{n}}+\lambda_{\mathrm{w}}\rho_{\mathrm{w}}\right)\mathbf{g}\right]-\nabla\cdot\left(\mathbf{K}\lambda_{\mathrm{w}}\nabla p_{\mathrm{c}}\right), \tag{5.7b}$$

where $\lambda_{\mathrm{n}}=k_{\mathrm{rn}}/\mu_{\mathrm{n}}$ and $\lambda_{\mathrm{w}}=k_{\mathrm{rw}}/\mu_{\mathrm{w}}$ represent the mobilities of the non-wetting and wetting phases, respectively. These are functions of S_{w} due to the dependency of the relative permeability on S_{w}. This equation system is fully coupled through Darcy velocity ($\mathbf{u}_{\mathrm{w}}$), which depends on the pressure and mobilities (see Eq. (5.3)).

5.1.1 Relative permeability and capillary pressure curves

Understanding the influence of saturation on both relative permeabilities and capillary pressure facilitates the reduction of unknowns in Eqs. (5.7a) and (5.7b) to S_w and p_n. This section introduces the concept of effective saturation for this purpose. Subsequently, a widely recognized correlation in the literature, the Brooks-Corey model, is presented to describe the influence of saturation on relative permeabilities and capillary pressure.

After the invading (wetting) phase displaces the non-wetting phase, a residual amount of the non-wetting phase remains trapped in the pore space, known as the residual non-wetting saturation (S_nr). Conversely, the residual wetting saturation (S_wr) represents the minimum saturation of the wetting phase that remains trapped in the pores. Using the concept of residual saturations, the effective saturation (S_eff) refers specifically to the portion of the pore space that actively participates in the flow of the wetting phase fluid. This can be expressed as

$$S_\mathrm{eff} = \frac{S_\mathrm{w} - S_\mathrm{wr}}{1 - S_\mathrm{nr} - S_\mathrm{wr}}. \tag{5.8}$$

It is important to note that both saturation (S) and effective saturation (S_eff) are dimensionless quantities confined to the range between zero and one. Brooks and Corey proposed correlations for relative permeability and capillary pressure based on experimental data from various rock formations [111]. These correlations utilize effective saturation (S_eff) as the independent variable. The Brooks-Corey expressions for the non-wetting phase relative permeability (k_rn), the wetting phase relative permeability (k_rw), and the capillary pressure (p_c) are presented as

$$k_\mathrm{rn}\left(S_\mathrm{w}\right) = k_\mathrm{rn,\,max}\left(1 - S_\mathrm{eff}\right)^2\left(1 - S_\mathrm{eff}^{1+\frac{2}{b}}\right), \tag{5.9a}$$

$$k_\mathrm{rw}\left(S_\mathrm{w}\right) = k_\mathrm{rw,\,max} S_\mathrm{eff}^{3+\frac{2}{b}}, \tag{5.9b}$$

$$p_\mathrm{c}\left(S_\mathrm{w}\right) = p_\mathrm{en} S_\mathrm{eff}^{-\frac{1}{b}}, \tag{5.9c}$$

where the exponent b is called the pore size distribution index and has the typical values from 0.2 to 3.0 [28]. The parameters $k_{\mathrm{rn,\,max}}$ and $k_{\mathrm{rw,\,max}}$ indicate the maximum achievable flow capacities for the non-wetting and wetting phases, respectively. These values correspond to the upper limits of relative permeability that each fluid can reach under ideal conditions. Ideal conditions in this context are scenarios where a fluid is completely saturated within a specific pore size range within the porous medium, thereby maximizing its flow potential. For the non-wetting fluid, this means saturation of the larger pores, while for the wetting fluid, it means complete occupancy of the smaller pores.

The parameter p_{en} is the “entry pressure” of the porous medium. During drainage processes (where a gas phase displaces a liquid phase), the concept of entry pressure has a well-defined meaning. It represents the minimum non-wetting phase pressure required to initiate invasion of a water-saturated porous medium [112]. The concept of entry pressure is not directly applicable to imbibition processes (where a liquid phase displaces a gas phase). In this scenario, p_{en} is the entry capillary pressure [113]. The Brooks-Corey model includes a macro-scale entry pressure, which is intended to serve as a macroscopic equivalent to the pore scale entry pressure described by the Young-Laplace equation [114]

$$p_{\mathrm{en}} = \frac{2\gamma_{\mathrm{LG}}\cos\theta}{r_{\mathrm{eff}}}. \tag{5.10}$$

This approach attempts to encapsulate the effects of pore scale phenomena on a larger scale within the porous medium by employing the notion of the effective capillary pore radius.

5.1.2 Initial and boundary conditions

A system of two equations (Eqs. (5.7a) and (5.7b)) with two unknowns (S_{w} and p_{n}) is established. To facilitate a solution, initial and boundary conditions are required. To model imbibition in lateral flow assays in this work, the initial state of wetting phase saturation within the domain is prescribed. The value of S_{w} is provided at the inlet, while a Neumann boundary condition is imposed on this parameter at the outlet. Furthermore, Dirichlet pressure boundary conditions are applied at both the inlet and outlet. This can be written as

$$S_{\mathrm{w}}(\mathbf{x}, 0) = S_{\mathrm{w,\ initial}}, \tag{5.11a}$$

$$S_{\mathrm{w}}(0, t) = S_{\mathrm{w,\ inlet}} \qquad p_{\mathrm{n}}(0, t) = p_{\mathrm{n,\ inlet}} \qquad p_{\mathrm{n}}(\mathbf{x}_{\mathrm{outlet}}, t) = p_{\mathrm{n,\ outlet}}. \tag{5.11b}$$

Furthermore, q_{w} and q_{n} are set to zero, which means that no source/sink term (q) is considered.

5.1.3 Implicit pressure explicit saturation (IMPES) algorithm[2]

»The implicit pressure explicit saturation (IMPES) algorithm is widely used for simulating two-phase flow in porous media. This paper concisely overviews the IMPES approach, focusing on its core principles and numerical implementation details. The governing equations for the IMPES algorithm are presented in Eqs. (5.7a) and (5.7b) for saturation and pressure, respectively. The numerical discretization follows the work of Redondo et al. [109], utilizing a second-order finite difference scheme for the spatial discretization.

Spatial discretization is implemented on a staggered Cartesian grid, with scalar quantities (saturation, pressure) evaluated at cell centers and vector quantities (velocities, gradients) computed at midpoints between cell centers. The absolute permeability tensor is assumed to be isotropic and diagonal. Mobilities, which are functions of saturation, are calculated using a total variation diminishing (TVD) upwind scheme. This scheme minimizes numerical artifacts, particularly in scenarios with sharp saturation transitions, by prioritizing the flow direction and incorporating upstream information into the mobility calculations.

---

[2] The contents of this section are verbatim reproduced from Jamshidi et al. [108], with permission of AIP Publishing.

Velocities are then determined using previously evaluated variables on the cell faces.

The core idea behind IMPES is the separation of pressure and saturation updates. As depicted in Figure 5.1, the IMPES algorithm employed in this study and implemented in PACE3D [82] proceeds as follows:
1. The initial state and boundary conditions are defined. In the simulation, S_w and p_n represent scalar variables associated with a single cell, while $\mathbf{u}_\mathrm{w}$ is a vector variable. To denote variables for the entire computational domain, encompassing all cells, bold font notation is used.
2. Pressure ($\mathbf{p}_\mathrm{n}^{(n)}$) calculation: The non-wetting phase pressure equation (Eq. 5.7b) is solved implicitly for the current time step denoted by the superscript (n). This equation is discretized into a system of linear equations with non-wetting phase pressure values as unknowns. This system can be expressed as $\mathbf{A}^{(n)}\mathbf{p}_\mathrm{n}^{(n)} = \mathbf{b}^{(n)}$, where $\mathbf{A}^{(n)}$ is the system matrix accounting for total transmissibilities (left side of Eq. (5.7b)), $\mathbf{p}_\mathrm{n}^{(n)}$ is the vector containing the non-wetting pressure at all points, and $\mathbf{b}^{(n)}$ includes terms related to flux sources, gravity, and capillary pressure (right side of Eq. (5.7b)). Unlike Redondo et al. [109], we use the biconjugate gradient stabilized (BiCGSTAB) method as the iterative solver for the non-wetting phase pressure equation.
3. Velocity ($\mathbf{u}_\mathrm{w}^{(n)}$) calculation: Pressure gradients are computed across each cell, and together with saturation-dependent mobilities, they determine the velocity field at the current time step.
4. The next time step, denoted as $t^{(n+1)}$, is calculated by summing the current time step ($t^{(n)}$) and the time interval (Δt).
5. The simulation ends when the specified simulation time is reached. If the desired simulation time is not attained, the process continues with further updates of the relevant fields.
6. Intermediate saturation ($\mathbf{S}_\mathrm{w}^{(n+1/2)}$) update: The saturation field, as governed by Eq. (5.7a), is explicitly updated for the first half of the time step ($\Delta t/2$) using the current velocity and current saturation values.
7. Intermediate pressure ($\mathbf{p}_\mathrm{n}^{(n+1/2)}$) computation: The pressure field is updated based on the intermediate saturation values.

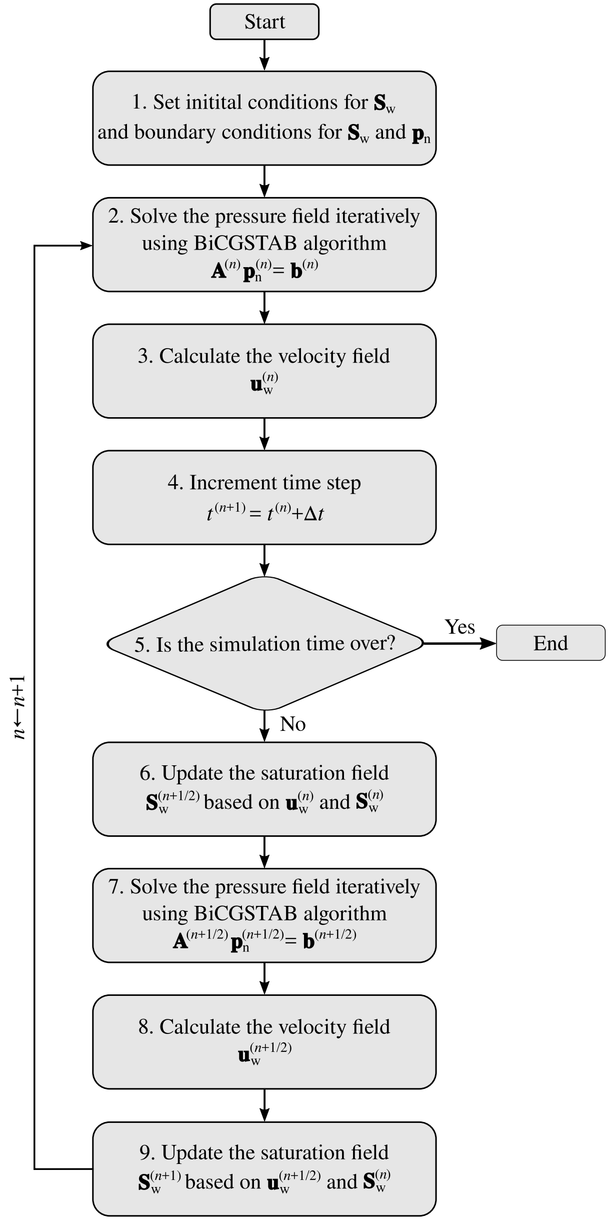

Figure 5.1: The flowchart depicts the iterative solution procedure of the implicit pressure explicit saturation (IMPES) algorithm for two-phase flow simulations. Bold font indicates field variables. Reproduced from [108], with the permission of AIP Publishing.

8. Intermediate velocity ($\mathbf{u}_{\mathrm{w}}^{(n+1/2)}$) calculation: The velocity field is updated based on the intermediate pressure gradients and mobilities. Using the intermediate velocity field improves the numerical stability of the algorithm.
9. Saturation ($\mathbf{S}_{\mathrm{w}}^{(n+1)}$) update: The wetting phase saturation equation (Eq. (5.7a)) is solved explicitly for the next time step, using the intermediate velocity field and current saturation values. The updated saturation field becomes the current reference state ($n \leftarrow n+1$). The entire process is then repeated from step 2.«

5.1.4 Reliability assessment of the IMPES solver

This section presents the verification and validation of the IMPES solver implemented within the PACE3D software environment for imbibition simulations. Case studies documented in the literature are used to achieve this objective. The verification and validation processes aim to establish the reliability and effectiveness of the solver for simulating imbibition phenomena.

Verification

The Buckley-Leverett equation, formulated by Buckley and Leverett, models two-phase flow in porous media [115]. It describes the temporal and spatial evolution of fluid saturations. This equation serves as a cornerstone for the analysis of various processes, including oil production and water flooding. Johansen et al. [116] presented an analytical solution to the Buckley-Leverett equation under constant pressure boundary conditions. This section verifies the implementation of the IMPES solver in PACE3D by employing the parameters used by Johansen et al. [116]. Table 5.1 summarizes the specific parameters used in the simulation.

Table 5.1: Parameters used for the verification of the IMPES solver in PACE3D.

Parameter	Description	Value
	Porous medium	
L	Length	1 m
ε	Porosity	18%
K	Permeability	10^{-12} m^2
	Non-wetting phase (oil)	
μ_n	Viscosity	$10^{-2}\ \text{kg}\,\text{m}^{-1}\,\text{s}^{-1}$
ρ_n	Density	$800\,\text{kg}\,\text{m}^{-3}$
$p_\text{n, inlet}$	Pressure at inlet	$21 \times 10^6\ \text{kg}\,\text{m}^{-1}\,\text{s}^{-2}$ (21 MPa)
$p_\text{n, outlet}$	Pressure at outlet	$17 \times 10^6\ \text{kg}\,\text{m}^{-1}\,\text{s}^{-2}$ (17 MPa)
S_nr	Residual saturation	0.3
	Wetting phase (water)	
μ_w	Viscosity	$10^{-3}\ \text{kg}\,\text{m}^{-1}\,\text{s}^{-1}$
ρ_w	Density	$998\,\text{kg}\,\text{m}^{-3}$
$S_\text{w, inlet}$	Saturation at inlet	0.7
S_wr	Residual saturation	0.25

The effect of gravity is assumed to be negligible and the relative permeability functions for the non-wetting and wetting phases are as follows

$$k_\text{rn}\left(S_\text{w}\right) = 0.8\left(\frac{1 - S_\text{w} - S_\text{nr}}{1 - S_\text{nr} - S_\text{wr}}\right)^2, \tag{5.12a}$$

$$k_\text{rw}\left(S_\text{w}\right) = 0.2\left(\frac{S_\text{w} - S_\text{wr}}{1 - S_\text{nr} - S_\text{wr}}\right)^2. \tag{5.12b}$$

A 1D simulation is performed with a spatial resolution of 100 cells for a domain length of 1 m. The boundary conditions for the simulation are as follows: the values of the non-wetting phase pressure (p_n) at the inlet and outlet and the wetting phase saturation (S_w) at the inlet are given in Table 5.1. A Neumann boundary condition is imposed on S_w, implying a zero-flux condition for this parameter at the outlet. The simulation incorporates a non-wetting phase residual saturation (S_{nr}) of 0.3, defining a lower bound for this parameter. Similarly, a minimum limit of 0.25 is established for the wetting phase residual saturation (S_{wr}). To reflect these conditions, the computational domain is initially saturated with a wetting phase saturation ($S_{\mathrm{w,\,initial}}$) of 0.25 (corresponding to an initial non-wetting phase saturation of 0.75). The simulation then progresses by maintaining a constant wetting phase saturation at the inlet boundary. Due to the imposed pressure difference between the inlet (higher pressure) and outlet, this constant saturation at the boundary continuously displaces the non-wetting phase further into the domain, thereby increasing the overall wetting phase saturation within the system. This mimics the process of wetting phase percolation.

The verification process compares the results obtained by the IMPES solver in PACE3D with the analytical solution of Johansen et al. [116]. Figure 5.2a shows the total flux (combined velocities of non-wetting and wetting phases) plotted against time. A distinct change in slope, observed as a knee in the plot, indicates the breakthrough time. This is the moment when the liquid front reaches the outlet. The analytical solution predicts a breakthrough time of 157.6 s. Notably, the solver results show excellent agreement with the analytical solution proposed by Johansen et al. [116].

Imbibition in porous media often exhibits diffuse interfaces between wetting and non-wetting fluids. These interfaces, as opposed to sharp boundaries, extend over a range of distances within the pore space. The specific method used to determine the location of this diffuse interface varies depending on the material properties and the fluids involved. A common approach to delineating the imbibition front in such scenarios is to select an intermediate value between the maximum saturation level (typically observed at the inlet) and the minimum saturation level (typically derived from either the initial condition or the outlet boundary).

In the present case study, where the wetting phase saturation (S_{w}) at the inlet is 0.7 and the residual wetting phase saturation (S_{wr}) is 0.25, the interface is defined as the point where the wetting phase saturation reaches a value of 0.4905, according to the analytical solution. Consequently, the breakthrough time derived from the IMPES simulation corresponds to the instant when the saturation of the wetting phase (S_w) reaches 0.4905 at the outlet. At half of the breakthrough time, corresponding to a value of 78.8 s, the liquid front ($S_\mathrm{w} = 0.4905$) is located at a

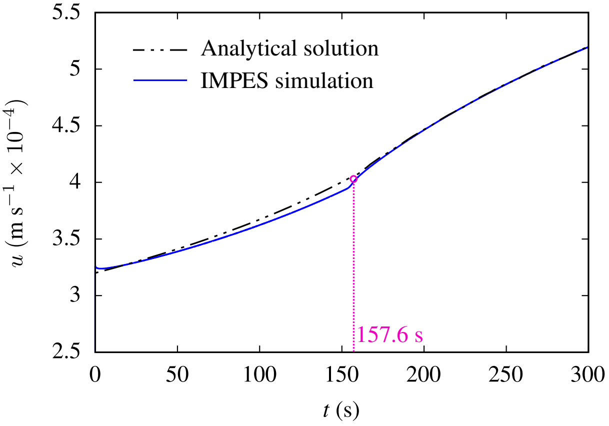

a)

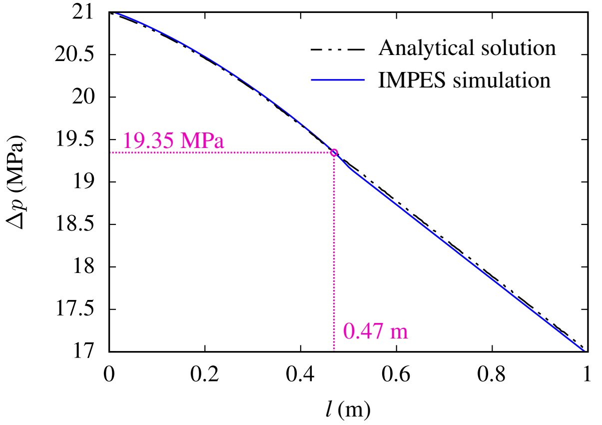

b)

Figure 5.2: Comparison of IMPES solver results in PACE3D with analytical solutions from [116]: a) Total flux (combined velocities of wetting and non-wetting phases) versus time. The breakthrough time is indicated. b) Pressure drop across the domain length at half the breakthrough time.

distance of 0.47 m. The pressure of the non-wetting phase at this point is determined to be 19.35 MPa. As depicted in Figure 5.2b, the pressure profile at half of the breakthrough time presents the key values associated with the interface. The comparison between the results obtained from the IMPES solver and the analytical solution revealed excellent agreement. This close correspondence verifies that the solver has been implemented correctly and is solving the mathematical equations accurately.

Validation[3]

»Altschuh et al. [81] investigated wicking in polymeric porous membranes using a two-phase phase-field approach to simulate wetting behavior within simplified representative structures. The simulation data were then employed to calculate the effective pore radius using Eqs. (3.2) and (3.3). Subsequently, the macro-scale flow model described by Eq. (2.45) was used to predict the wicking time in a straight membrane profile based on the calculated effective pore radius. Notably, the predicted wicking times exhibited good agreement with experimental data, highlighting the effectiveness of their approach. This methodology is referred to as a "semi-analytical solution" in this section due to its reliance on a simplified model for calculating the effective pore radius. Based on their experimental data and semi-analytical solution, this section aims to validate the implemented IMPES solver within PACE3D. The validation process leverages the parameters employed by Altschuh et al. [81]. These specific parameters are summarized in Table 5.2.

The wicking process is investigated through simulations of a straight (rectangular) membrane vertically positioned in a *Porefil*® reservoir. Due to a Bond number not significantly less than unity (detailed in section 3.3.2), the influence of gravity is included in the simulations. The gravitational acceleration vector is set

---

[3] The contents of this section are verbatim reproduced from Jamshidi et al. [108], with permission of AIP Publishing.

Table 5.2: Parameters used for the validation of the IMPES solver in PACE3D.

Parameter	Description	Value	
	Porous membrane	**Type C**	**Type D**
a_1	Width in horizontal direction (mm)	25	25
h_1	Length in vertical direction (mm)	40	40
ε	Porosity (%)	89	82
K	Permeability ($\times 10^{-12}$ m^2)	1.683	0.778
r_p	Mean pore radius (µm)	2.16	1.73
r_l	Mean ligament radius (µm)	0.64	0.72
	Non-wetting phase (air)		
μ_n	Viscosity ($\mathrm{kg\,m^{-1}\,s^{-1}}$)	1.76×10^{-5}	
ρ_n	Density ($\mathrm{kg\,m^{-3}}$)	1.0	
S_nr	Residual saturation (-)	0	
	Wetting phase (*Porefil*®)		
μ_w	Viscosity ($\mathrm{kg\,m^{-1}\,s^{-1}}$)	2.2×10^{-3}	
ρ_w	Density ($\mathrm{kg\,m^{-3}}$)	1800	
$S_\mathrm{w,\,inlet}$	Saturation at inlet (-)	1	
S_wr	Residual saturation (-)	0.01	
γ_LG	Surface tension coefficient ($\mathrm{N\,m^{-1}}$)	0.016	
θ	Contact angle (°)	0	

to $\mathbf{g} = (0, -9.81, 0)^\mathrm{T}\ \mathrm{m\,s^{-2}}$. This inclusion is consistent with the semi-analytical solution, allowing a direct comparison between the simulation results and those obtained from both semi-analytical and experimental methods.

This approach focuses on two-phase flow simulations of wicking processes in distinct membrane profiles, which differs from the 1D single-phase model for unidirectional flow analysis within test strips. The two-phase model operates by discretizing the test strip profile. Straight membranes allow the representation of the computational domain in either one or two dimensions. Conversely, non-straight membranes, like those with a barbell-shaped profile, necessitate a 2D computational mesh to capture variations in the cross-sectional area accessible to the wicking liquid.

Wicking processes in two separate membrane types from Table 5.2 are simulated using the IMPES solver in PACE3D. For the investigated straight membrane, simulations are conducted using both a uniform 1D mesh containing 160 cells and a 2D mesh with dimensions of 100×160 cells. Both meshes yield a spatial resolution of 2.5×10^{-4} m. To ensure the accuracy of the solution, a TVD limiter with a small value of 0.01 is implemented. The relative permeabilities are calculated using Eqs. (5.9a) and (5.9b), with both $k_{\mathrm{rn,\,max}}$ and $k_{\mathrm{rw,\,max}}$ set to unity.

Boundary conditions for the simulation are defined as follows: i) at the inlet, $p_{\mathrm{n}} = p_{\mathrm{w}} + p_{\mathrm{c}} = p_{\mathrm{atm}} + p_{\mathrm{c}}$ and $S_{\mathrm{w}} = 1$, and ii) at the outlet, $p_{\mathrm{n}} = p_{\mathrm{atm}} - \rho_{\mathrm{n}} g h_1$. A Neumann boundary condition is imposed on S_{w} (zero-flux) at the outlet. iii) On both sides of the 2D domain, Neumann boundary conditions are imposed for both p_{n} and S_{w}.

This case study employs the IMPES algorithm for solving the governing equations of two-phase flow in porous membranes (Eq. (5.7)). The functions of relative permeabilities and capillary pressure based on effective saturation are established further using the Brooks-Corey model. When the effective saturation (defined by Eq. (5.8)) approaches zero, i.e., $S_{\mathrm{w}} \to S_{\mathrm{wr}}$, the relative permeability of the wetting phase also approaches zero ($k_{\mathrm{rw}} \to 0$). Since relative permeability reflects a phase's ability to flow within the porous media, a zero value of k_{rw} signifies complete immobility for the wetting phase. This would effectively block the wetting phase flow. Moreover, this leads to unrealistically high capillary pressure values (approaching infinity) during the simulation. To mitigate these numerical instabilities, a threshold value for the wetting phase saturation is implemented. Accordingly, the computational domain is initially saturated with a wetting phase saturation of 0.011. This value is chosen to be close to the residual wetting phase saturation (S_{wr}), considering $S_{\mathrm{nr}} = 0$.

The wetting phase commences its ascension from the reservoir through the pore space. In computational terms, $S_{\mathrm{w}} = 1$ from the inlet upwards, progressively filling the cells initially containing $S_{\text{w, initial}} = 0.011$. Once the wetting phase saturation surpasses the threshold of 0.011, the liquid front is considered to have reached that cell. Consequently, the foremost computational cell where S_{w} exceeds 0.011 is identified as the location of the liquid front.

To validate the implementation of the IMPES solver within the PACE3D software, this section utilizes a modified version of the capillary pressure derived from the Brooks-Corey model. This adjustment involves dividing the original capillary pressure equation (Eq. (5.9c)) by a factor of 1.4. While the unmodified Brooks-Corey model is commonly used for two-phase flow simulations in porous media, the modified version is employed here to achieve consistency when comparing the simulation results generated by the IMPES solver with the experimental data. It is important to distinguish that this adjustment is not intended to validate the Brooks-Corey model itself, but rather to facilitate a more effective validation of the solver's ability to capture the physics of the two-phase flow and wicking process within porous membranes. Hence, the following modified Brooks-Corey model is used for consistency in the remaining simulations presented in this study

$$k_{\text{rn}}(S_{\text{w}}) = (1 - S_{\text{eff}})^2 \left(1 - S_{\text{eff}}^{1+\frac{2}{b}}\right), \tag{5.13a}$$

$$k_{\text{rw}}(S_{\text{w}}) = S_{\text{eff}}^{3+\frac{2}{b}}, \tag{5.13b}$$

$$p_{\text{c}}(S_{\text{w}}) = \frac{1}{1.4} p_{\text{en}} S_{\text{eff}}^{-\frac{1}{b}}, \tag{5.13c}$$

with $b = 2$. Note that the entry pressure (p_{en}) is determined using Eq. (5.10). This equation incorporates the effective capillary radius, which is calculated based on Eqs. (3.2) and (3.3).

Figure 5.3 presents a comprehensive comparison between experimental observations and model predictions for wicking behavior in two distinct porous membrane types, designated as type C and type D. The experimental data points are represented by the symbols in the figure. Overlaid upon these data points are

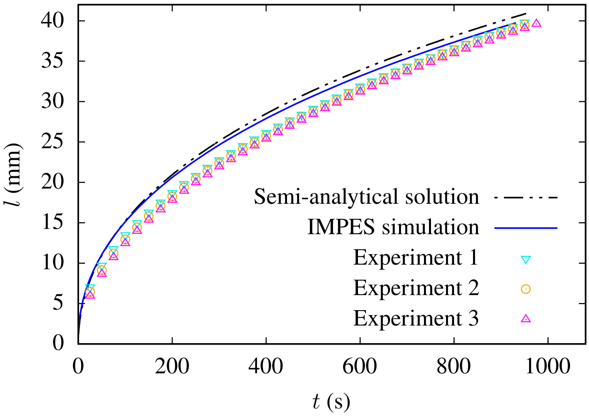

a)

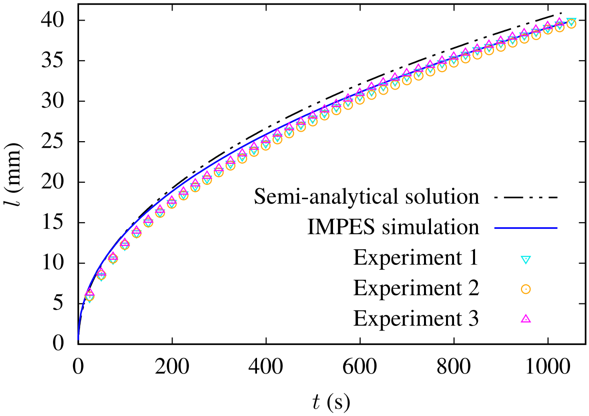

b)

Figure 5.3: Comparison of wicking curves for two porous membrane types: a) type C and b) type D. Solid lines represent the results of the IMPES solver (1D and 2D simulations). Experimental data are depicted by symbols, while dashed lines show the semi-analytical solutions from [81]. Reproduced from [108], with the permission of AIP Publishing.

the curves depicting the predictions from both the semi-analytical method (represented by dashed lines) and the IMPES solver (represented by solid lines). The figure reveals a strong agreement between the model predictions and the experimental data for both porous membrane types.

A comparative analysis was performed to evaluate the performance of the semi-analytical solution and the IMPES simulation against experimental data. Percentage error analysis was applied using the experimental data as reference values for position measurements at different time points. The percentage error was calculated using

$$Error = \left| \frac{l - l_{\text{experiment}}}{l_{\text{experiment}}} \right| \cdot 100, \tag{5.14}$$

where l represents the predicted wicking length from one of the methods and $l_{\text{experiment}}$ represents the wicking length from Experiment 2. The average percentage error was calculated to provide a quantitative measure of the deviation of each method from the experimental data. The semi-analytical solution yielded an average percentage error of 18.85%, while the IMPES simulation achieved a lower average error of 15.70% for membrane type C. For membrane type D, these values were 14.78% and 10.03%, respectively.

This comparison shows that while both methods provide reasonable approximations to the experimental results, the IMPES simulations exhibit greater accuracy with lower errors compared to semi-analytical solutions. The reduced error of the IMPES solver suggests that the numerical simulation better captures the dynamics of the system under study and provides a closer representation of the experimental data for both membrane types. This observation provides strong validation for the accuracy and effectiveness of the implemented IMPES solver in simulating wicking phenomena within porous membranes.«

Comparison with the single-phase method[4]

»A macro-scale, single-phase model has been established to investigate the dynamics of liquid transport within lateral flow assays (LFAs). The primary objective of this model was to understand how variations in membrane geometry affect the wicking phenomenon. To isolate the geometrical effects, the model intentionally excluded membrane-related parameters (e.g., permeability) and fluid-related parameters (e.g., viscosity). These excluded effects were implicitly considered by calibrating Eq. (4.7) against experimental data obtained from a straight membrane.

While the single-phase model provided valuable insights, a two-phase approach, i.e., the IMPES simulation, is used in this section to consider the influence of microstructure characteristics and fluid properties. To perform a direct comparison between the two-phase and single-phase methods, four membrane profiles are chosen. These profiles have been previously investigated using the single-phase model and range from straight to hexagonal, sand-timer-shaped, and barbell-shaped profiles.

The IMPES simulation setup for this analysis builds upon the validation case with two key modifications: i) Membrane type: Membrane type A (see Table 3.1) is employed. In the experimental investigation and the single-phase model, in contrast, a *UniSart® CN 140 backed* membrane was utilized. ii) Wetting phase properties: To maintain consistency with the experimental data and the single-phase model, water is chosen as the wetting phase. Its properties are detailed in Table 3.2. This choice gives a surface tension coefficient (γ_{LG}) of $0.053\,\mathrm{N\,m^{-1}}$ and a contact angle (θ) of 36° [8].

Figure 5.4 shows a comparison between the wicking curves predicted by both the single-phase model and the IMPES solver, along with experimental data for various membrane profiles. The observed good agreement between the predictions of

---

[4] The contents of this section are verbatim reproduced from Jamshidi et al. [108], with permission of AIP Publishing.

the IMPES solver and the experimental data for all investigated membrane profiles indicates its ability to accurately capture the wicking behavior within these porous materials. This finding serves as a valuable validation of the effectiveness of the implemented IMPES solver in simulating wicking phenomena in LFAs.

The proposed approach in this section incorporates the influence of microstructural characteristics such as porosity and absolute permeability. In other words, it leverages micro-scale data within macro-scale simulations. Consequently, this methodology for investigating the wicking process in LFAs can be categorized as a multi-scale approach. The successful application of the IMPES solver to various cases in this section demonstrates its versatility and robustness in simulating fluid flow through different membrane types and configurations.«

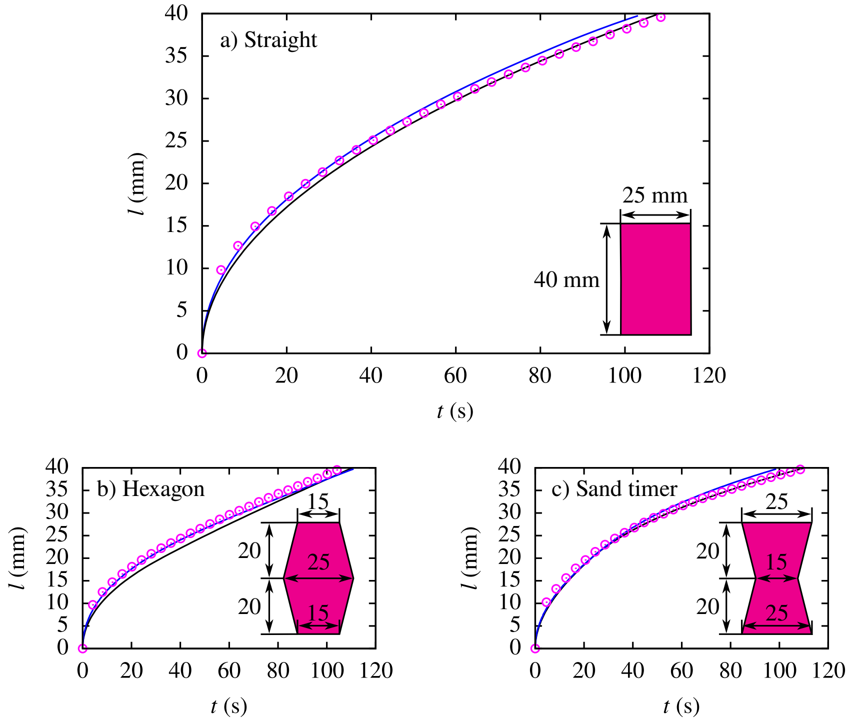

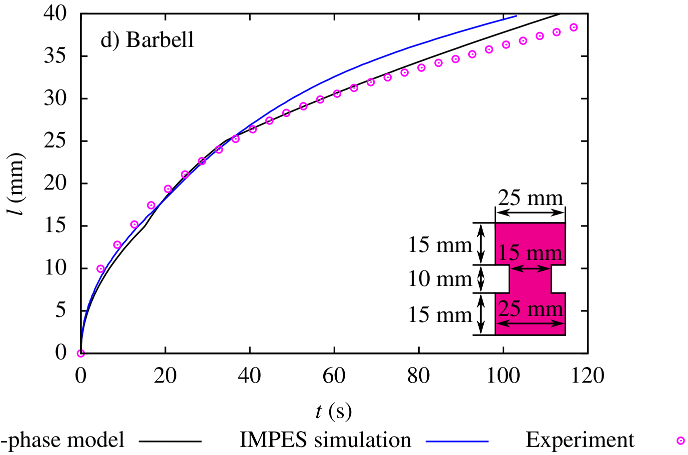

Figure 5.4: Comparison of wicking curves for various membrane profiles: a) straight, b) hexagonal, c) sand timer-shaped, and d) barbell-shaped configuration. Results are presented for the single-phase model, two-phase IMPES simulation, and experimental investigations. Inset figures depict the dimensions of each profile in millimeters. Reproduced from [108], with the permission of AIP Publishing.

5.2 Influence of geometry on wicking in multi-branch membranes[5]

»In this section, the IMPES solver is used to investigate the wicking process in multi-branch membranes. These geometries are characterized by the presence of multiple flow paths, allowing multiple experiments to be performed simultaneously, thereby increasing experimental throughput. By using the IMPES algorithm to simulate fluid flow within these structures, a more comprehensive understanding of wicking behavior in such complex geometries can be achieved.

---

[5] The contents of this section are verbatim reproduced from Jamshidi et al. [108], with permission of AIP Publishing.

The design of lateral flow assays (LFAs) can be guided by the principles of optimal flow configurations observed in nature, as embodied in the constructal law [117, 118]. This law suggests that natural systems evolve toward configurations that promote optimal efficiency in transporting a fluid. Examples of this phenomenon can be seen in the tree-shaped structures of blood vessels, tree branches, and river basins. Motivated by this principle, numerous studies have explored the application of optimal design principles in branched flow networks [119–123]. These studies focus on minimizing the total hydraulic resistance within the network, taking into account factors such as individual segment geometry, branching patterns, number of branches, and material properties such as permeability. Typically, constraints are imposed on the network design, such as a fixed occupied area, volume, or total length. As documented in the literature, Lagrange multipliers can be used to derive optimal geometries that minimize flow resistance within these given constraints. This section explores the application of some of these optimized geometries as potential membrane profiles for LFA test strips.

5.2.1 Wicking in Y-shaped membranes

The initial exploration of multi-branch membranes commences with the simplest geometry: Y-shaped profiles, as shown schematically in Figure 5.5. These profiles have a single level of bifurcation, which allows for the creation of two distinct fluid flow paths within the membrane. Assuming identical widths and lengths for the daughter segments, the geometry of the Y-shaped profile can be systematically varied by adjusting the following parameters: i) Length ratio (l_2/l_1): This parameter is defined as the ratio of the length of a daughter segment (l_2) to the length of the first (main/parent) segment (l_1). ii) Width ratio (a_2/a_1): This parameter represents the ratio between the width of a daughter segment (a_2) and the width of the first segment (a_1). iii) Branching angle (δ): This parameter defines the angle formed between the two daughter segments.

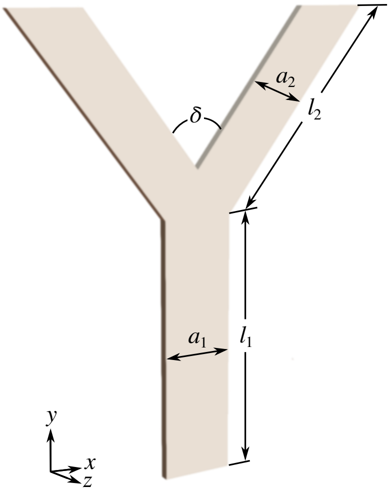

Figure 5.5: Illustration of the membrane profile with a Y-shaped configuration. Reproduced from [108], with the permission of AIP Publishing.

The analysis of branching patterns has attracted significant scientific interest across both natural and engineered systems. The Hess-Murray law, named after Walter Rudolf Hess and Cecil Dunmore Murray, establishes a correlation between the radii of successive branches in bifurcating or trifurcating vessels observed in biological tissues [124, 125]. This law is premised on minimizing the work required for blood or lymph circulation within living organisms. It defines an “optimal branching ratio” expressed as $r_{b+1}/r_b = 2^{-1/3} \approx 0.7937$ where the index b represents the bifurcation level, and r_b and r_{b+1} denote the radii of the parent and daughter vessels, respectively.

The Hess-Murray law has been rigorously re-evaluated through extensive theoretical and experimental studies. These investigations have confirmed its validity under well-defined conditions, particularly for vessels with micro-scale radii. However, as evidenced by the research documented in [126, 127], the applicability of the law diminishes for vessels with larger dimensions. While the Hess-Murray law offers a valuable “cubic root of 2” correlation for branching ratios,

Table 5.3: Length ratio (l_2/l_1), width ratio (a_2/a_1), and branching angle (δ) of Y-shaped membrane profiles.

Sample	l_2/l_1 (-)	a_2/a_1 (-)	δ (°)	From
Y1	0.4672	0.394	60	[128]
Y2	0.567	0.433	60	[126]
Y3	$2^{-\frac{1}{3}} \approx 0.7937$	$2^{-\frac{1}{3}} \approx 0.7937$	75	[124, 125]
Y4	1	$2^{-\frac{3}{7}} \approx 0.743$	75	[129]
Y5	$2^{-\frac{1}{2}} \approx 0.707$	$2^{-\frac{1}{4}} \approx 0.8409$	90	[130]
Y6	0.8	0.8	135	[131]

researchers have explored alternative configurations in the literature. Table 5.3 summarizes these additional branching ratios and angles in addition to the Hess-Murray configuration.

The Y-shaped membrane profiles used in this study are derived from several sources, each offering a different perspective on optimal branching configurations. **Y1 profile** is adapted from the work of Shou et al. [128], who investigated flow dynamics in tree-shaped networks. Their theoretical work aimed at designing the distribution of the radius and length of local branches to achieve the fastest capillary flow. **Y2 profile** originates from the re-evaluation of the Hess-Murray law by Sciubba [126]. Sciubba proposed an alternative shape based on the functionality of the capillary network, suggesting that both the optimal bifurcation angle and the optimal radius ratio depend on the shape of the domain served by the bifurcation. **Y3 profile** is based on the Hess-Murray law and is consistent with the concept of maximum physical efficiency for connecting successive vessel segments. The size ratio is consistent with the law's suggestion for impermeable tree networks, as described by Miguel et al. [132]. **Y4 profile** is adapted from examples in a study by Bejan and Lorente [129] who focused on optimizing the global performance of flow systems subject to global constraints. They assumed a constrained total volume occupied by the channels and sought to minimize the total flow resistance in the Y-shaped configuration. **Y5 profile** is derived from a study by Soni et al. [130], which presents an analytical approach for both steady and unsteady flows. Their approach yielded optimal relationships for the homothetic ratio of tube sizes and optimal angles between daughter tubes. These optimal relationships satisfy the criterion of minimizing flow impedance, taking into account both geometry and svelteness ratio. **Y6 profile** is adapted from the work of Sehn et al. [131] who studied the laminar flow of non-Newtonian fluids in Y-shaped structures with varying ratios of parent and daughter tube sizes using numerical analysis.

In contrast to the case studies using the 1D single-phase model, where the focus was on the wicking behavior within single-passage membranes, the two-phase approach investigates wicking in multi-passage (multi-branch) membranes. These membranes provide multiple paths for fluid flow, as exemplified by the Y-shaped profile where the flow splits into two daughter segments. Due to the significantly smaller thickness of the membrane in the z-direction compared to the other two spatial directions, the fluid motion within these Y-shaped profiles can be simulated using the 2D two-phase model. This is done using the validated IMPES solver implemented in the PACE3D software. Subsequently, a comparative analysis of the simulation results obtained for different Y-shaped configurations is performed to evaluate the influence of the aforementioned geometric parameters on the wicking behavior.

Y-shaped membrane profiles with dimensions given in Table 5.3 are investigated using wicking simulations. These profiles possess an overall vertical length of 25 ± 0.5 mm and a first segment width of 3.86 mm. The simulations employ an equidistant grid with a resolution of 7.9×10^{-5} m. This resolution is determined to be sufficiently fine after a mesh independence study (not shown). Boundary conditions identical to those used in the validation case are applied to both the non-wetting phase pressure and the wetting phase saturation. Air and water are employed as the non-wetting and wetting phases, respectively, with their properties detailed in Table 3.2. Residual saturations of 0 and 0.01 are assigned to the non-wetting and wetting phases, respectively, while the initial wetting phase saturation is set to 0.011. The TVD limiter is assigned a value of 0.01. Membrane type A, as described in Table 3.1, is selected for the simulations.

Figure 5.6 presents the results for the wicking length as a function of time within the Y-shaped membranes. Due to the symmetric geometry of the profiles around the y-axis, the liquid front propagates identically in the two daughter segments. Consequently, the vertical coordinate of the liquid front within the first segment and subsequently within one of the daughter segments is monitored to represent the wicking length.

The results reveal a higher wicking velocity in the early stages of the process. All investigated geometries exhibit similar wicking behavior until the liquid front reaches their respective bifurcation points, which can vary in vertical position. Beyond these points, differences in the wicking curves become apparent. Notably, the wicking curves for Y-shaped membranes with identical branching angles remain closely aligned. Among the investigated geometries, the Y-shaped profile with a 60° branching angle from [128] exhibits the fastest imbibition, while the 135° Y-shaped membrane displays the slowest wicking time. In general, a longer wicking time is associated with a larger branching angle for Y-shaped membranes. This phenomenon can be explained by the constraint imposed on the total length in the y-direction. When considering a fixed vertical length for all Y-shaped geometries with comparable width ratios, a larger branching angle translates to a longer path for the fluid to travel within the porous membrane, resulting in a longer wicking time.

Analogous to the observations made during the analysis of wicking in T-shaped membranes with expansions, the presence of a junction in Y-shaped profiles leads to a decrease in wicking velocity within the subsequent segment. Another recurring wicking phenomenon observed in both T-shaped and Y-shaped profiles relates to the influence of earlier liquid entry into subsequent segments. As illustrated in Figure 5.6, earlier entry into the second segment results in a steeper slope of the wicking curve, indicating a higher liquid velocity in that segment. Specifically, the wicking velocity observed in the second segment of the Y4 profile

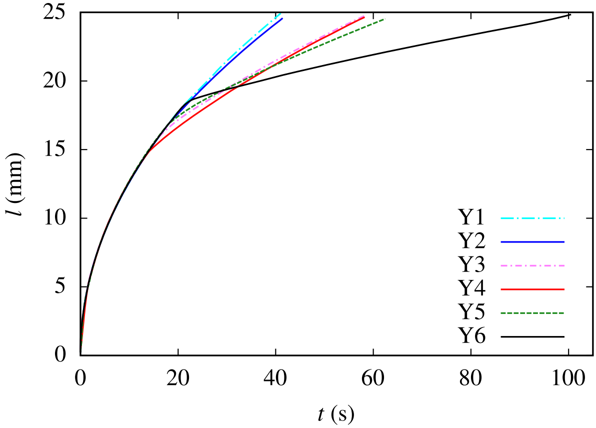

Figure 5.6: Wicking length of water over time in Y-shaped membranes (profiles in Table 5.3). Reproduced from [108], with the permission of AIP Publishing.

(solid red line) surpasses that of the Y6 profile (solid black line). Consequently, the liquid front in Y4 progresses faster, overtaking the liquid front in Y6. This translates to a slower overall wicking process in Y6 compared to Y4.

5.2.2 Wicking in membranes with four branches

This section investigates the wicking behavior within membranes characterized by two levels of bifurcation, forming a tree-shaped structure, as shown in Figure 5.7a. The dimensions of these tree-shaped membranes are obtained from the literature. In addition to the use of existing geometries, this study incorporates novel technology. *Sartorius* has developed a method for engraving various patterns into CN membranes. For the purposes of this study, *Sartorius* has kindly provided two membrane profiles from their multiplexed LFAs, as depicted in Figure 5.7b and c.

Tree-shaped flow networks with two bifurcation levels are characterized by the emergence of two daughter branches from a single parent branch at each bifurcation point in the subsequent level. The length and width ratios between these daughter and parent branches are expressed as l_{b+1}/l_b and a_{b+1}/a_b, respectively, where the index b ($b = 1, 2$) denotes the bifurcation level.

Natural systems exhibit characteristic size changes at vessel bifurcations. As documented by Miguel [132], the ratio of successive lengths and diameters between daughter and parent vessels defines a scale factor, or homothetic ratio, independent of the specific bifurcation level (b). Notably, for laminar flow conditions, the Hess-Murray law proposes optimal length and width ratios of $2^{-1/3}$ for ideal connections between parent and daughter vessels. This translates to a halving of diameters and lengths after every three successive branching generations. However, alternative configurations have been explored by researchers and may be more applicable in certain scenarios, as documented in the literature. Table 5.4 summarizes these alternative branching ratios and angles for tree-shaped membrane profiles (Tree1, Tree3, and Tree4), in addition to the configuration derived from the Hess-Murray law (Tree2).

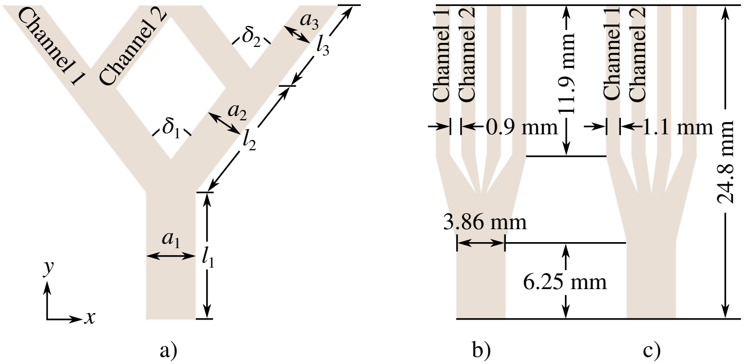

Figure 5.7: Illustration of the membrane profile with four branches: a) tree-shaped configuration; b) *Sartorius* multiplex I, and c) *Sartorius* multiplex II. Reproduced from [108], with the permission of AIP Publishing.

Table 5.4: Length ratio (l_{b+1}/l_b) and width ratio (a_{b+1}/a_b) between the $b+1$st branch and the bth branch, and branching angle (δ_1 and δ_2) of tree-shaped membrane profiles.

Sample	l_{b+1}/l_b (-)	a_{b+1}/a_b (-)	δ_1 (°)	δ_2 (°)	From
Tree1	0.4799	0.4306	60	60	[128]
Tree2	$2^{-\frac{1}{3}} \approx 0.7937$	$2^{-\frac{1}{3}} \approx 0.7937$	75	75	[124, 125]
Tree3	0.5	0.5	81.72	106.22	[133]
Tree4	0.5	0.5	90	90	[133]

The wicking processes in tree-shaped membrane profiles with dimensions given in Table 5.4 and multiplexed membranes provided by *Sartorius* are studied using 2D simulations. All these profiles have a total vertical length of 25 ± 0.5 mm and a first segment width of $a_1 = 3.86\,\mathrm{mm}$. The simulations are performed using the IMPES solver within the PACE3D software framework. An equidistant grid with a resolution of 7.9×10^{-5} m is used. Other simulation setups are similar to those employed for wicking in Y-shaped membranes.

Figures 5.8–5.10 present the wetting phase saturation profiles obtained from 2D simulations of wicking within the tree-shaped membrane (Tree2) based on the Hess-Murray law and within the multiplexed membranes designed by *Sartorius*. These figures serve to visualize the spreading behavior of the liquid. The evolution of the liquid interface within the remaining tree-shaped geometries listed in Table 5.4 is presented in appendix A. The figures reveal a gradual diffusion of the liquid interface as it propagates throughout the domain. This diffusive behavior is a consequence of employing a small TVD limiter value in the simulations. This choice aligns with the observation of a diffuse interface in the wicking experiments. Conversely, simulations using a larger TVD limiter value would have resulted in a sharper delineation of the liquid interface.

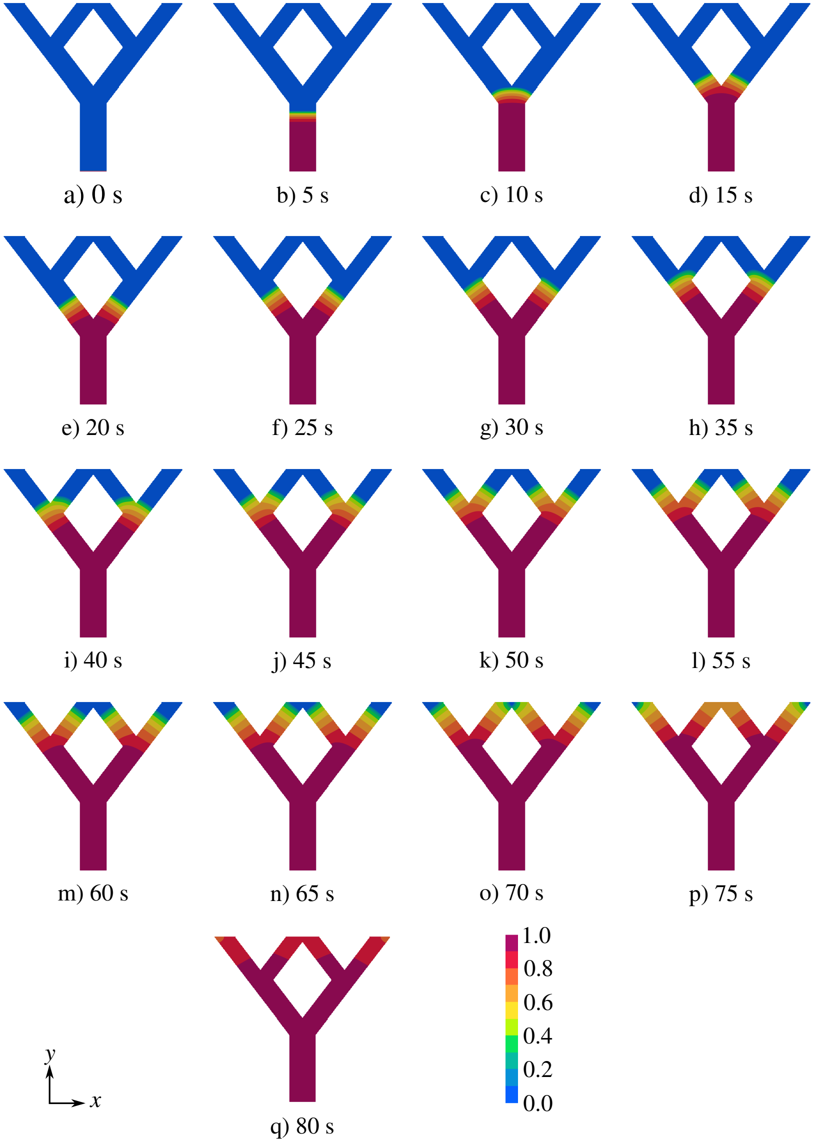

Figure 5.8: The wetting phase (water) saturation in Tree2 membrane profile from Table 5.4, where the evolution is displayed every 5 seconds. Reproduced from [108], with the permission of AIP Publishing.

Tree-shaped networks are characterized by a hierarchical structure. An initial segment (bottom segment) bifurcates into two daughter segments (middle segments), and each daughter segment further splits into two channels (top segments). As shown in Figure 5.8, the geometry is symmetric around the y-axis. As a result, the fluid spreads evenly through the inner channels (channel 2). This is also evident in the wicking in the outer channels (channel 1). After about 70 s, the figure shows that the wicking in Tree2 membrane progresses to the end of channel 2, while this time is 80 s for channel 1. This phenomenon can be attributed to the closer proximity of the middle segment to channel 2. This allows the wicking fluid to enter channel 2 before reaching channel 1, resulting in the observed difference in wetting times. This observation highlights the influence of channel arrangement on wicking behavior within these geometries since other parameters such as length or width ratios remain identical for both inner and outer channels.

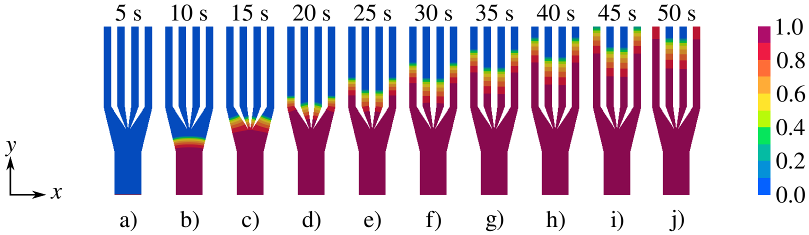

Figure 5.9: The wetting phase (water) saturation in the multiplex I designed by *Sartorius*, where the evolution is displayed every 5 seconds. Reproduced from [108], with the permission of AIP Publishing.

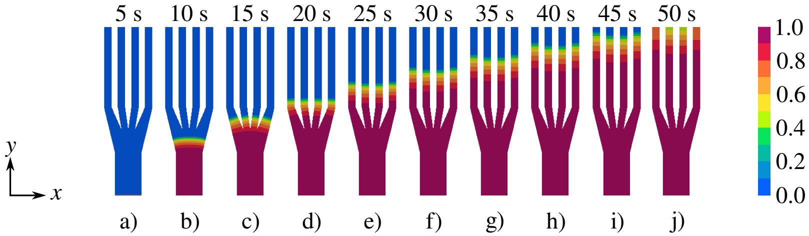

Figure 5.10: The wetting phase (water) saturation in the multiplex II designed by *Sartorius*, where the evolution is displayed every 5 seconds. Reproduced from [108], with the permission of AIP Publishing.

As evident in Figure 5.9, the liquid fronts in the outer branches advance faster than those in the inner branches. This phenomenon can be attributed to the narrower inlet of the inner branches, which restricts fluid inflow and consequently leads to a longer wicking time. In contrast, Figure 5.10 depicts wider inlets for the inner channels, resulting in comparable advancement of the liquid fronts across all branches.

The results for the wicking length as a function of time within the tree-shaped and multiplexed membranes are shown in Figure 5.11. Due to the symmetric geometry of the profiles around the *y*-axis (see Figure 5.7), only the liquid fronts in the bottom segment and the left middle segment and then in channels 1 and 2 of each profile need to be plotted. Consequently, the vertical coordinates of the liquid fronts in all these segments are monitored to represent the wicking length.

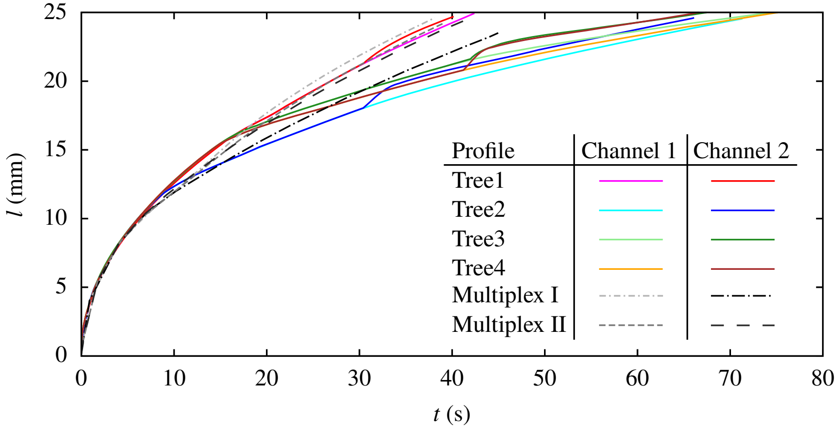

Figure 5.11: Wicking length over time for the tree-shaped membranes from Table 5.4 and multiplexed membranes designed by *Sartorius*. Reproduced from [108], with the permission of AIP Publishing.

The results demonstrate a higher wicking velocity at the initial stages of the process for all investigated geometries. This behavior persists until the liquid front reaches the first bifurcation point for each geometry, with these points potentially exhibiting variations in vertical position. Beyond these points, distinct features emerge in the wicking curves.

Among the geometries studied, the outer branches (channel 1) of multiplex I display the fastest wicking. This is due to two factors: the shorter fluid path through the 25 mm membrane and the wider inflow segment, characteristics not shared by the inner branches (channel 2). Notably, the difference in wicking times between channels 1 and 2 in multiplex II is less pronounced compared to multiplex I.

Within the tree-shaped geometries, Tree1 exhibits the fastest imbibition, comparable to the wicking processes observed in both multiplexed LFAs. Conversely, Tree2, Tree3, and Tree4 exhibit slower wicking processes due to the requirement for the wicking liquid to traverse longer membranes.

As noted earlier in this section and illustrated in Figure 5.11, wicking in channel 2 of tree-shaped membranes is generally faster than in channel 1. This phenomenon is due to the closer proximity of the middle segment to channel 2, which gives the wicking liquid preferential access compared to channel 1. This observation suggests a valuable design strategy. By strategically manipulating the arrangement of branches within a tree-shaped network, wicking velocity can be tailored to optimize device performance for a specific application.

5.2.3 Wicking in membranes with asymmetric branches

Up to this point, the investigations have focused on wicking processes in membranes with branches that exhibit symmetry around the vertical axis. To elucidate the influence of asymmetry on wicking behavior, the 2D wicking simulation is repeated for a modified tree-shaped network based on the Hess-Murray law. This modified network is generated by removing the right inner channel from the previously studied symmetric design. The resulting visualizations of fluid propagation within this asymmetric network are presented in Figure 5.12.

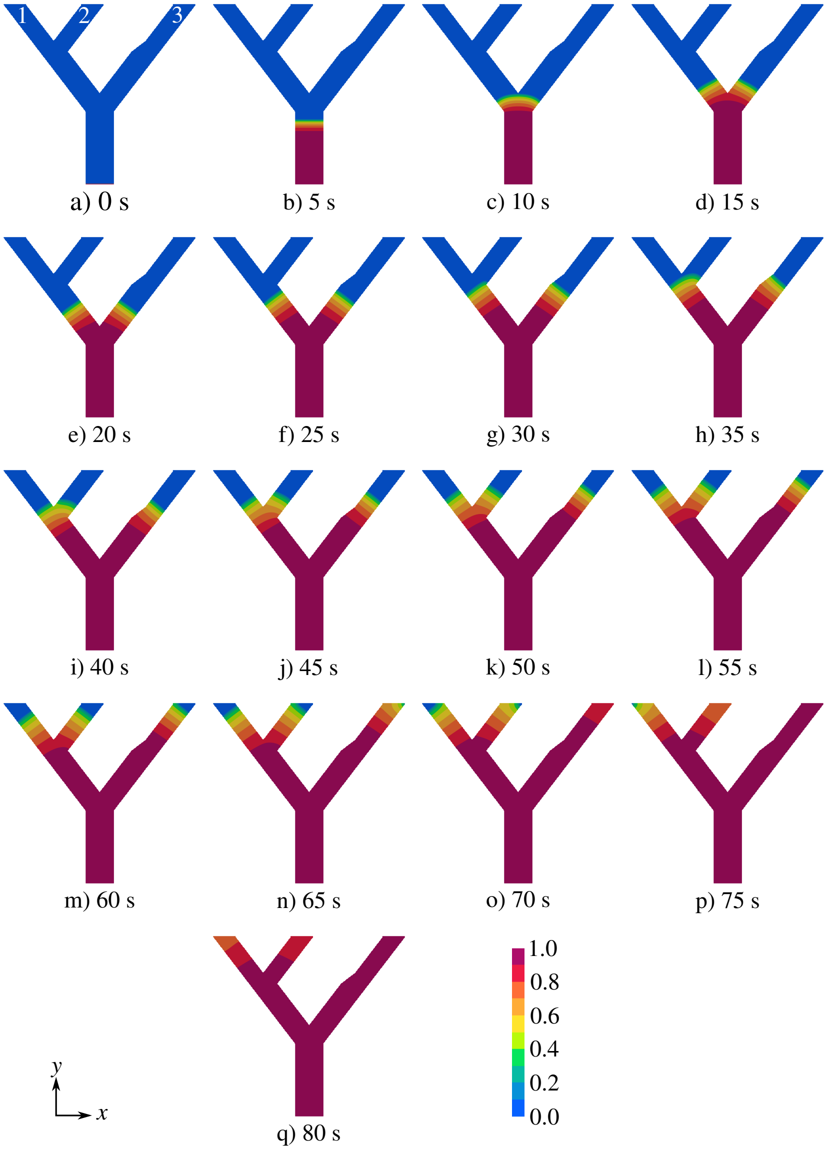

a) 0 s b) 5 s c) 10 s d) 15 s e) 20 s f) 25 s g) 30 s h) 35 s i) 40 s j) 45 s k) 50 s l) 55 s m) 60 s n) 65 s o) 70 s p) 75 s q) 80 s

Figure 5.12: The wetting phase (water) saturation in the asymmetric Tree2 membrane profile from Table 5.4, where the evolution is displayed every 5 seconds. Reproduced from [108], with the permission of AIP Publishing.

As can be seen, the fluid front shows different evolutions through the asymmetric channels. When labeled from the left, as shown in Figure 5.12a, the wicking in the right channel (channel 3) progresses faster. This is due to two factors: the absence of a bifurcation in the right middle segment and the reduced total pore space compared to the total pore space of channels 1 and 2. In simpler terms, all incoming fluid from the right middle segment can wet the membrane in channel 3 more quickly. This behavior is in contrast to the observations for the symmetric membrane based on the Hess-Murray law, as shown in Figure 5.8, where wicking in the outer channels takes longer. However, consistent with the findings for symmetric tree-shaped membranes, wicking in channel 2 remains faster than in channel 1 due to the closer proximity of the middle segment to channel 2. The observations in this section highlight that not only does the arrangement of the channels influence wicking behavior, but the presence of asymmetry also plays a significant role.

Figure 5.13 depicts the evolution of the wicking fronts within the channels of the asymmetric tree-shaped membrane as a function of time. Due to the asymmetry, data for all three liquid fronts are presented for comparative analysis. The figure

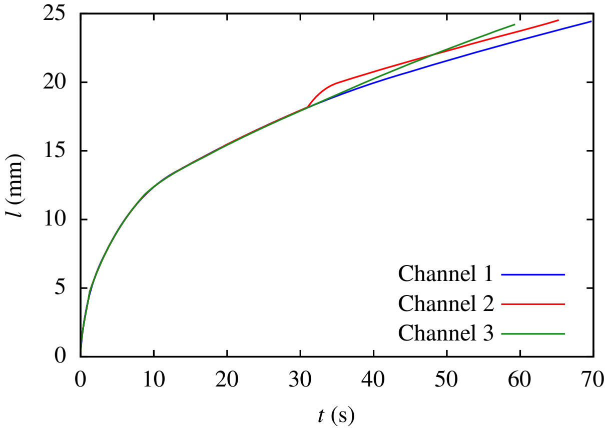

Figure 5.13: Wicking length over time for the asymmetric Tree2 membrane from Table 5.4. Reproduced from [108], with the permission of AIP Publishing.

reveals a faster movement of the wetting fluid across the membrane in the early stages. The wicking curves for channels 1 and 2 show identical behavior before reaching the bifurcation point where the liquid splits. However, because channel 2 is closer to the incoming fluid, it exhibits a higher wetting phase saturation earlier than channel 1. Within channel 3, the fluid movement initially mirrors channels 1 and 2 until just over 30 s. Notably, the wicking front in channel 3 surpasses that of channel 2 shortly before reaching 50 s.«

5.3 Influence of membrane on wicking in multi-branch membranes[6]

»This section investigates the influence of membrane type on the wicking behavior in multiplexed LFAs designed by *Sartorius* (see Figure 5.7). Two different membrane types from Table 3.1 are selected for wicking simulations using the IMPES solver in PACE3D. The simulation setup replicates that used in section 5.2.2 for consistency. Due to the symmetry of the geometries around the y-axis, only the liquid fronts within an outer channel (channel 1) and an inner channel (channel 2) are captured for analysis. Figure 5.14 presents the wicking curves for these channels in both membrane types A (dashed lines) and B (solid lines).

As expected, the wicking trends observed for membrane type B are similar to those for type A. However, the wicking process is significantly slower for membrane type B due to its lower permeability. Furthermore, when using the same membrane type but different designs (multiplex I and II), the geometric factors cause the disparity between the wicking curves of the two channels. For example, in the case of membrane type A, the difference in wicking times between channels 1 and 2 is less pronounced in multiplex II compared to multiplex I. This observation is also true for membrane type B. Interestingly, a comparison of the

---

[6] The contents of this section are verbatim reproduced from Jamshidi et al. [108], with permission of AIP Publishing.

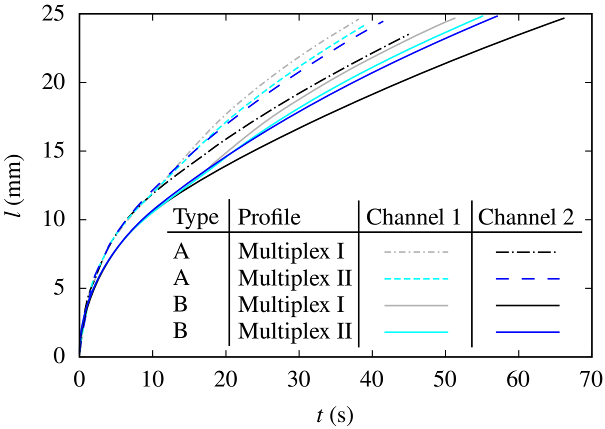

Figure 5.14: Wicking length over time for the multiplexed membranes designed by *Sartorius* with the membrane types from Table 3.1. Reproduced from [108], with the permission of AIP Publishing.

wicking curves for different membrane types shows that the choice of membrane material can either increase or decrease the existing discrepancies in wicking behavior between channels. Using this knowledge, it becomes possible to manipulate or control the wicking behavior not only by geometric design but also by strategic selection of different membrane types.«

5.4 Summary

This chapter presents a macroscopic, two-phase model for investigating fluid transport within lateral flow assays (LFAs). The model employs the implicit pressure explicit saturation (IMPES) algorithm and accounts for the displacement of an initial (incumbent) fluid by an invading fluid during the imbibition process. Microscopic properties, characterized using the methods presented in chapter 3, are utilized as input data for the macroscopic IMPES simulations. This integration of micro-scale data into macro-scale modeling allows the study of the wicking behavior in different LFAs while considering the influence of both the underlying microstructural properties and the macroscopic features. The robustness of this multi-scale approach is established through verification and validation against existing literature and experimental data. This process demonstrates that the proposed approach provides a reliable tool for simulating fluid flow across various membrane types and configurations.

To quantify the wicking process in Y-shaped and multi-branch membranes, the vertical positions of the liquid fronts within each channel are monitored. The study reveals that for Y-shaped membranes, the branching angle has a significant influence on the wicking behavior. In addition, for membranes with four branches, the wicking velocity decreases as the inflow entrance narrows. These factors are critical considerations when designing LFAs for multiple tests. In addition to the parameters of length ratio, width ratio, branching angle, bifurcation point location, and inflow inlet width, other factors such as asymmetry and membrane type can also influence the wicking behavior of LFAs. The knowledge gained in this chapter can be used to optimize design parameters, including wicking time and velocity, for specific LFA applications and target analytes.

6 Conclusion and future work

This dissertation comprehensively investigated capillary-driven two-phase flows within porous membrane structures, focusing on the fluid flow mechanisms relevant to lateral flow assays (LFAs) used in medical diagnostics. To elucidate the underlying fluid dynamics, both micro- and macro-scale perspectives were considered. The analysis of porous structures and their associated micro-scale flow characteristics informed the development of single-phase models and two-phase simulations for macro-scale fluid flow.

Characterization

Initially, synthetic porous structures were generated using the Voronoi tessellation (VT) algorithm. Additionally, real porous structures were explored by integrating imaging methods with data conversion techniques. This approach resulted in the creation of digital twins of real structures as 3D reconstructed models for further analysis. The generation process ensured identical porosities between the real and digital structures. The porosity of real membranes was determined using a gravimetric method, with observed values ranging from approximately 0.8 to 0.9. Other micro-scale parameters such as pore and ligament radii, tortuosity, and permeability were analyzed using the software package PACE3D based on equidistant grids. A linear proportionality between tortuosity and porosity was observed for the studied membranes.

Single-phase modeling

At the macro-scale, a single-phase model has been developed to study liquid transport within single-passage, multi-segment membranes used in LFAs. This model enabled the analysis of how geometrical changes in the membrane profile affect the wicking process. Membrane-related parameters were excluded from the single-phase model, and their effects were captured by fitting Eq. (4.7) to experimental data from straight membranes. Various membrane geometries, including straight, hexagonal, sand timer-shaped, barbell-shaped, and T-shaped profiles, were investigated. Macro-scale wicking experiments were conducted for different membrane profiles to determine the wicking time over the entire membrane length. The results demonstrated a strong agreement between the single-phase model and experimental data.

For wicking in hexagonal and sand timer-shaped profiles with equal widths at the beginning and end, a shorter wicking time compared to a straight membrane was observed when half or more of the profile consisted of a converging segment. Conversely, a predominantly diverging shape for more than half of the membrane length resulted in a longer wicking time. Wicking in T-shaped membrane profiles revealed that an expansion leads to a decrease in velocity in the subsequent segment, where the velocity remains almost constant. Flow resistance decreased as the aspect ratio between the width of the second segment and the first segment decreased, allowing the fluid to reach its final position more quickly. Earlier liquid entry into the second segment resulted in a steeper slope of the wicking length, indicating a higher liquid velocity in this segment. Overall, expansions in the different membrane profiles reduced the wicking velocity, and all slopes of liquid propagation in the second segments were lower than that of the straight membrane. The single-phase model predicted a non-smooth fluid motion with distinct knees for barbell-shaped membrane profiles, which accurately reflected the observed experimental wicking behavior.

Two-phase simulation[1]

»In the present study, a multi-scale modeling framework was developed to investigate capillary-driven fluid dynamics in polymeric porous membranes employed in lateral flow assays (LFAs). The framework incorporates microscopic characteristics of the membranes into a macroscopic, two-phase flow model, leading to a comprehensive understanding of wicking phenomena in LFAs. The model explicitly accounts for the complex interactions between the permeating and displaced fluids within the porous structure, providing a refined representation of the wicking process.

Utilizing the implicit pressure explicit saturation (IMPES) algorithm, the two-phase model captures both microstructural and macroscopic influences on fluid flow. The effectiveness of the model has been rigorously validated against established literature and experimental data, demonstrating its reliability for simulating fluid transport across various membrane configurations. To the best of our knowledge, the approach proposed in this study represents a novel numerical modeling technique for investigating the wicking process within multiplexed LFAs. This innovative framework offers a comprehensive approach to study the wicking process within membranes of arbitrary profiles and with different membrane properties. This is a significant step forward in the field of LFA research.

A quantitative analysis of the wicking process in Y-shaped and multi-branch membranes was performed by tracking the vertical progression of the liquid fronts (wicking length), which quantifies the extent of liquid advancement within the channels. The results show a significant influence of the branching angle on the wicking dynamics in Y-shaped membranes. For instance, a membrane with a vertical length of 25 cm requires approximately 41 s to wick when the branching angle is 60° (Y1 profile). However, this value increases to approximately 101 s for a branching angle of 135° (Y6 profile).

---

[1] The contents of this section are verbatim reproduced from Jamshidi et al. [108], with permission of AIP Publishing.

Four-branch membranes are advantageous for multiplexed LFAs involving four tests. These membranes exhibit different wicking times for a vertical length of 25 cm. For example, Tree1 profile requires only about 40 s for complete wicking, while Tree2, Tree3, and Tree4 require more than 65 s. For four-branch membranes, the wicking velocity exhibits an inverse relationship with the inflow entrance width. These findings are crucial for the design of multiplexed LFAs, as they inform the consideration of factors such as length ratio, width ratio, branching angle, bifurcation point location, and inflow entrance dimensions, along with asymmetry and membrane type.

The results of this study enable the manipulation of wetting behavior within lateral flow assays (LFAs). By leveraging the acquired data, precise control over wetting characteristics can be achieved, thereby enhancing LFA performance and reliability.«

Sensitivity analysis

A convection-diffusion-reaction model was employed to address the challenge of quantitatively assessing signal intensity in LFAs. This model facilitated the determination of the optimal test line location. In addition, the model was coupled with the single-phase model to predict signal intensity in straight membranes. This approach incorporated the microstructural properties of the porous membrane and wetting properties, providing a multi-scale perspective.

By utilizing data-driven information and a holistic understanding of the structure-sensitivity relationship, this comprehensive approach has the potential to significantly contribute to ongoing research efforts aimed at enhancing the sensitivity of diagnostic assays.

Summary

The methodologies presented in this thesis contribute to a comprehensive understanding of the physical transport processes within LFAs. This understanding facilitates the manipulation of the wicking process to achieve a desired velocity at a specific location within the LFA. It also allows for the optimization of channel geometry and arrangement, ultimately leading to reduced measurement times and enhanced assay sensitivity. Finally, the knowledge gained from this research regarding transport processes in LFAs and sensitivity analysis has the potential to be applied to the development and improvement of commercial products.

Outlook

In this dissertation, multi-scale approaches were used to comprehensively investigate the complex processes governing fluid flow in lateral flow assays (LFAs). At the micro-scale, a detailed characterization of wetting parameters in porous polymer membranes was performed. At the macro-scale, capillary flow phenomena in LFAs have been studied using three complementary approaches: experimental investigations, single-phase modeling, and two-phase simulations.

Future research efforts could be directed toward anisotropic porous membranes. In the present study, isotropic porous media were investigated. In this context, isotropic means that the absolute permeability tensor is diagonal with equal diagonal elements, indicating uniform permeability in all directions. However, real porous membranes may exhibit anisotropic properties, where the resistance to fluid flow varies with direction. The inclusion of an anisotropic permeability tensor in the model would allow a more complete understanding of the imbibition process in the anisotropic LFAs.

The influence of backing cards on the wicking process in LFAs could be investigated in future studies. Typically, porous membranes in LFAs are mounted on backing cards for several reasons, including manufacturability, handling, and improved mechanical stability. The presence of the backing card introduces new boundary conditions that are not currently considered. Future investigations could integrate these conditions into the models to reveal the impact of backing cards on fluid flow and lead to optimized designs for improved LFA performance.

The potential to strategically combine different membrane types for different branches within a multiplexed LFA could be explored. As shown in Figure 5.14, the membrane type has a significant effect on the wicking process. This finding suggests that strategically combining different membrane types within a single LFA design could be beneficial. Future research could explore this concept with a focus on designing multiplexed LFAs with tailored wicking times and velocities, even with limitations on overall device size. Optimizing the combination of membrane types has the potential to significantly improve the efficiency and effectiveness of multiplexed LFAs.

Finally, topology optimization techniques could be used to achieve desired flow distributions within multiplexed LFAs. This approach could lead to the development of novel LFA designs with optimized performance characteristics. By using computational methods to optimize the spatial arrangement and structure of the membranes, it would be possible to achieve more precise control of fluid flow within the LFA, ultimately improving its diagnostic capabilities.

In conclusion, by exploring anisotropic porous membranes, incorporating the influence of backing cards, designing multiplexed LFAs with tailored membrane combinations, and applying topology optimization techniques, future research has the potential to further enhance the performance and applicability of lateral flow assays in medical diagnostics.

Bibliography

[1] F. A. Coutelieris and J. Delgado, *Transport processes in porous media*, 1st ed., ser. Advanced Structured Materials. Springer Berlin, Heidelberg, 2012.

[2] M. Quintard and S. Whitaker, "Convection, dispersion, and interfacial transport of contaminants: Homogeneous porous media," *Advances in Water Resources*, vol. 17, no. 4, pp. 221–239, 1994. [Online]. Available: https://www.sciencedirect.com/science/article/pii/0309170894900027

[3] T. Kristian Stevik, Kari Aa, G. Ausland, and J. Fredrik Hanssen, "Retention and removal of pathogenic bacteria in wastewater percolating through porous media: A review," *Water Research*, vol. 38, no. 6, pp. 1355–1367, 2004. [Online]. Available: https://www.sciencedirect.com/science/article/pii/S0043135403007140

[4] M. Farzan, R. Roth, J. Schoelkopf, J. Huwyler, and M. Puchkov, "The processes behind drug loading and release in porous drug delivery systems," *European Journal of Pharmaceutics and Biopharmaceutics*, vol. 189, pp. 133–151, 2023. [Online]. Available: https://www.sciencedirect.com/science/article/pii/S0939641123001418

[5] M. Shojaeefard, G. Molaeimanesh, M. Nazemian, and M. Moqaddari, "A review on microstructure reconstruction of pem fuel cells porous electrodes for pore scale simulation," *International Journal of Hydrogen Energy*, vol. 41, no. 44, pp. 20 276–20 293, 2016. [Online]. Available: https://www.sciencedirect.com/science/article/pii/S0360319916326738

[6] S. Kasetsirikul, M. J. A. Shiddiky, and N.-T. Nguyen, “Challenges and perspectives in the development of paper-based lateral flow assays,” *Microfluidics and Nanofluidics*, vol. 24, no. 2, p. 17, February 2020. [Online]. Available: https://doi.org/10.1007/s10404-020-2321-z

[7] J. D. Bishop, H. V. Hsieh, D. J. Gasperino, and B. H. Weigl, “Sensitivity enhancement in lateral flow assays: A systems perspective,” *Lab Chip*, vol. 19, pp. 2486–2499, 2019. [Online]. Available: http://dx.doi.org/10.1039/C9LC00104B

[8] P. Altschuh, “Skalenübergreifende Analyse makroporöser Membranen im Kontext digitaler Zwillinge,” Ph.D. dissertation, Karlsruhe Institute of Technology (KIT), Karlsruhe, 2020.

[9] M. K. Das, P. P. Mukherjee, and M. K, *Modeling transport phenomena in porous media with applications*. Cham: Springer Cham, 2018.

[10] J. Ettrich, “Fluid flow and heat transfer in cellular solids,” Ph.D. dissertation, Karlsruhe Institute of Technology (KIT), Karlsruhe, September 2014.

[11] D. Wildenschild and A. P. Sheppard, “X-ray imaging and analysis techniques for quantifying pore-scale structure and processes in subsurface porous medium systems,” *Advances in Water Resources*, vol. 51, pp. 217–246, 2013, 35th Year Anniversary Issue. [Online]. Available: https://www.sciencedirect.com/science/article/pii/S0309170812002060

[12] B. Dietrich, W. Schabel, M. Kind, and H. Martin, “Pressure drop measurements of ceramic sponges – Determining the hydraulic diameter,” *Chemical Engineering Science*, vol. 64, no. 16, pp. 3633–3640, 2009. [Online]. Available: https://www.sciencedirect.com/science/article/pii/S0009250909003133

[13] B. Ghanbarian, A. G. Hunt, R. P. Ewing, and M. Sahimi, “Tortuosity in porous media: A critical review,” *Soil Science Society of America Journal*, vol. 77, no. 5, pp. 1461–1477, 2013. [Online]. Available: https://acsess.onlinelibrary.wiley.com/doi/abs/10.2136/sssaj2012.0435

[14] J. Fu, H. R. Thomas, and C. Li, “Tortuosity of porous media: Image analysis and physical simulation,” *Earth-Science Reviews*, vol. 212, p. 103439, 2021. [Online]. Available: https://www.sciencedirect.com/science/article/pii/S0012825220304852

[15] L. Shen and Z. Chen, “Critical review of the impact of tortuosity on diffusion,” *Chemical Engineering Science*, vol. 62, no. 14, pp. 3748–3755, 2007. [Online]. Available: https://www.sciencedirect.com/science/article/pii/S0009250907003144

[16] J. Joos, “Microstructural characterisation, modelling and simulation of solid oxide fuel cell cathodes,” Ph.D. dissertation, Karlsruhe Institute of Technology (KIT), Karlsruhe, 2017.

[17] G. E. Archie, “The electrical resistivity log as an aid in determining some reservoir characteristics,” *Transactions of the AIME*, vol. 146, no. 01, pp. 54–62, 1942.

[18] S. P. Friedman, “Soil properties influencing apparent electrical conductivity: A review,” *Computers and Electronics in Agriculture*, vol. 46, no. 1, pp. 45–70, 2005, applications of Apparent Soil Electrical Conductivity in Precision Agriculture. [Online]. Available: https://www.sciencedirect.com/science/article/pii/S0168169904001255

[19] R. Masoodi and K. M. Pillai, *Wicking in porous materials: Traditional and modern modeling approaches*. Boca Raton: CRC Press, 2012, p. 380. [Online]. Available: https://www.taylorfrancis.com/books/e/9780429105067

[20] K. Vafai, *Handbook of porous media*, 2nd ed. Boca Raton: Crc Press, 2005.

[21] A. Nabovati, E. W. Llewellin, and A. C. Sousa, “A general model for the permeability of fibrous porous media based on fluid flow simulations using the lattice boltzmann method,” *Composites Part A: Applied Science and*

Manufacturing, vol. 40, no. 6, pp. 860–869, 2009. [Online]. Available: https://www.sciencedirect.com/science/article/pii/S1359835X09001080

[22] F. A. Dullien, *Porous media: Fluid transport and pore structure*, 2nd ed. San Diego: Academic press, 2012.

[23] Y. Çengel and J. Cimbala, *Fluid mechanics: Fundamentals and applications*, 4th ed. New York: McGraw-Hill Education, 2018.

[24] W. Kunz, P. Altschuh, M. Bremerich, M. Selzer, and B. Nestler, "Establishing structure–property linkages for wicking time predictions in porous polymeric membranes using a data-driven approach," *Materials Today Communications*, vol. 35, p. 106004, 2023. [Online]. Available: https://www.sciencedirect.com/science/article/pii/S2352492823006955

[25] F. M. White, *Fluid mechanics*, 7th ed., ser. Mcgraw-Hill series in mechanical engineering. New York, NY: McGraw-Hill, 2009.

[26] B. Kronberg, K. Holmberg, and B. Lindman, *Surface and interfacial tension*. John Wiley & Sons, Ltd, 2014, ch. 12, pp. 231–249. [Online]. Available: https://onlinelibrary.wiley.com/doi/abs/10.1002/9781118695968.ch12

[27] A. Marchand, J. H. Weijs, J. H. Snoeijer, and B. Andreotti, "Why is surface tension a force parallel to the interface?" *American Journal of Physics*, vol. 79, no. 10, pp. 999–1008, October 2011. [Online]. Available: https://doi.org/10.1119%2F1.3619866

[28] P. Bastian, "Numerical computation of multiphase flows in porous media," Habilitation thesis, Christian-Albrecht University of Kiel, Kiel, 1999.

[29] T. Ahmed, "Chapter 4 - fundamentals of rock properties," in *Reservoir engineering handbook*, 4th ed., T. Ahmed, Ed. Boston: Gulf Professional Publishing, 2010, pp. 189–287. [Online]. Available: https://www.sciencedirect.com/science/article/pii/B9781856178037500122

[30] H. K. Versteeg and W. Malalasekera, *An introduction to computational fluid dynamics*, 2nd ed. Harlow: Pearson Education Limited, 2007.

[31] N. Fries, “Capillary transport processes in porous materials – Experiment and model,” Ph.D. dissertation, University of Bremen, Göttingen, 2010.

[32] R. Masoodi, K. M. Pillai, and P. P. Varanasi, “Role of hydraulic and capillary Radii in improving the effectiveness of capillary model in wicking,” in *Fluids engineering division summer meeting*, vol. Volume 1: Symposia, Parts A and B, 08 2008, pp. 251–259. [Online]. Available: https://doi.org/10.1115/FEDSM2008-55172

[33] R. Masoodi and K. Pillai, “A general formula for capillary suction-pressure in porous media,” *Journal of Porous Media*, vol. 15, no. 8, pp. 775–783, 2012.

[34] R. Masoodi, K. M. Pillai, and P. P. Varanasi, “Darcy’s law-based models for liquid absorption in polymer wicks,” *American Institute of Chemical Engineers AIChE J.*, vol. 53, pp. 2769–2782, 2007. [Online]. Available: https://aiche.onlinelibrary.wiley.com/doi/full/10.1002/aic.11322

[35] Liu Zhi, He Xiaocong, Han Jiaxiu, Zhang Xiuhai, Li Fei, Li Ang, Qu Zhiguo, and Xu Feng, “Liquid wicking behavior in paper-like materials: Mathematical models and their emerging biomedical applications,” *Microfluidics and Nanofluidics*, vol. 22, no. 11, p. 132, 2018.

[36] F. Jamshidi, W. Kunz, P. Altschuh, M. Bremerich, R. Przybylla, M. Selzer, and B. Nestler, “Geometric flow control in lateral flow assays: Macroscopic single-phase modeling,” *Physics of Fluids*, vol. 34, no. 6, p. 062110, June 2022. [Online]. Available: https://doi.org/10.1063/5.0093316

[37] M. A. F. Zarandi, K. M. Pillai, and A. S. Kimmel, “Spontaneous imbibition of liquids in glass-fiber wicks. part i: Usefulness of a sharp-front approach,” *AIChE Journal*, vol. 64, no. 1, pp. 294–305,

2018. [Online]. Available: https://aiche.onlinelibrary.wiley.com/doi/abs/10.1002/aic.15965

[38] J. M. Bell and F. K. Cameron, “The flow of liquids through capillary spaces,” *The Journal of Physical Chemistry*, vol. 10, no. 8, pp. 658–674, 1906. [Online]. Available: https://doi.org/10.1021/j150080a005

[39] R. Lucas, “Über das Zeitgesetz des kapillaren Aufstiegs von Flüessigkeiten,” *Kolloid-Zeitschrift*, vol. 23, pp. 15–22, 1918.

[40] E. W. Washburn, “The dynamics of capillary flow,” *Physical Review*, vol. 17, pp. 273–283, March 1921. [Online]. Available: https://link.aps.org/doi/10.1103/PhysRev.17.273

[41] J. Berthier, D. Gosselin, and E. Berthier, “A generalization of the Lucas-Washburn-Rideal law to composite microchannels of arbitrary cross section,” *Microfluidics and Nanofluidics*, vol. 19, pp. 497–507, 2016.

[42] J. Cai, E. Perfect, C.-L. Cheng, and X. Hu, “Generalized modeling of spontaneous imbibition based on Hagen-Poiseuille flow in tortuous capillaries with variably shaped apertures,” *Langmuir*, vol. 30, no. 18, pp. 5142–5151, 2014, pMID: 24785579. [Online]. Available: https://doi.org/10.1021/la5007204

[43] R. Sharma and D. S. Ross, “Kinetics of liquid penetration into periodically constricted capillaries,” *Journal of the Chemical Society, Faraday Transactions*, vol. 87, pp. 619–624, 1991. [Online]. Available: http://dx.doi.org/10.1039/FT9918700619

[44] T. L. Staples and D. G. Shaffer, “Wicking flow in irregular capillaries,” *Colloids and Surfaces A: Physicochemical and Engineering Aspects*, vol. 204, no. 1, pp. 239–250, 2002. [Online]. Available: https://www.sciencedirect.com/science/article/pii/S0927775701011384

[45] D. Patro, S. Bhattacharyya, and V. Jayaram, “Flow kinetics in porous ceramics: Understanding with non-uniform capillary models,” *Journal*

of the American Ceramic Society, vol. 90, no. 10, pp. 3040–3046, 2007. [Online]. Available: https://ceramics.onlinelibrary.wiley.com/doi/abs/10.1111/j.1551-2916.2007.01776.x

[46] M. Reyssat, L. Courbin, E. Reyssat, and H. A. Stone, "Imbibition in geometries with axial variations," *Journal of Fluid Mechanics*, vol. 615, p. 335–344, 2008.

[47] E. M. Benner and D. N. Petsev, "Potential flow in the presence of a sudden expansion: Application to capillary driven transport in porous media," *Physical Review E*, vol. 87, p. 033008, March 2013. [Online]. Available: https://link.aps.org/doi/10.1103/PhysRevE.87.033008

[48] W. W. Liou, Y. Peng, and P. E. Parker, "Analytical modeling of capillary flow in tubes of nonuniform cross section," *Journal of Colloid and Interface Science*, vol. 333, no. 1, pp. 389–399, 2009. [Online]. Available: https://www.sciencedirect.com/science/article/pii/S0021979709000897

[49] H. Mehrabian, P. Gao, and J. J. Feng, "Wicking flow through microchannels," *Physics of Fluids*, vol. 23, no. 12, p. 122108, 2011. [Online]. Available: https://doi.org/10.1063/1.3671739

[50] J. Cai, T. Jin, J. Kou, S. Zou, J. Xiao, and Q. Meng, "Lucas–washburn equation-based modeling of capillary-driven flow in porous systems," *Langmuir*, vol. 37, no. 5, pp. 1623–1636, 2021, pMID: 33512167. [Online]. Available: https://doi.org/10.1021/acs.langmuir.0c03134

[51] R. Masoodi and K. M. Pillai, "Darcy's law-based model for wicking in paper-like swelling porous media," *American Institute of Chemical Engineers AIChE J.*, vol. 56, pp. 2257–2267, 2010. [Online]. Available: https://aiche.onlinelibrary.wiley.com/doi/abs/10.1002/aic.12163

[52] S. Whitaker, "Flow in porous media I: A theoretical derivation of Darcy's law," *Transport in Porous Media*, vol. 1, no. 1, pp. 3–25, 1986.

[53] M. M. Gong and D. Sinton, "Turning the page: Advancing paper-based microfluidics for broad diagnostic application," *Chemical Reviews*, vol.

117, no. 12, pp. 8447–8480, 2017, pMID: 28627178. [Online]. Available: https://doi.org/10.1021/acs.chemrev.7b00024

[54] G. A. Posthuma-Trumpie, J. Korf, and A. van Amerongen, "Lateral flow (immuno)assay: Its strengths, weaknesses, opportunities and threats. a literature survey," *Analytical and Bioanalytical Chemistry*, vol. 393, pp. 569–582, 2009.

[55] E. B. Bahadır and M. K. Sezgintürk, "Lateral flow assays: Principles, designs and labels," *TrAC Trends in Analytical Chemistry*, vol. 82, pp. 286 – 306, 2016. [Online]. Available: http://www.sciencedirect.com/science/article/pii/S0165993616300668

[56] C. L. A. Berli and P. A. Kler, "A quantitative model for lateral flow assays," *Microfluidics and Nanofluidics*, vol. 20:104, 2016. [Online]. Available: https://link.springer.com/article/10.1007/s10404-016-1771-9

[57] R. T. Armstrong, M. L. Porter, and D. Wildenschild, "Linking pore-scale interfacial curvature to column-scale capillary pressure," *Advances in Water Resources*, vol. 46, pp. 55–62, 2012. [Online]. Available: https://www.sciencedirect.com/science/article/pii/S0309170812001443

[58] J. E. McClure, S. Berg, and R. T. Armstrong, "Capillary fluctuations and energy dynamics for flow in porous media," *Physics of Fluids*, vol. 33, no. 8, p. 083323, 2021. [Online]. Available: https://doi.org/10.1063/5.0057428

[59] H. Li, D. Han, M. A. Hegener, G. M. Pauletti, and A. J. Steckl, "Flow reproducibility of whole blood and other bodily fluids in simplified no reaction lateral flow assay devices," *Biomicrofluidics*, vol. 11, no. 2, p. 024116, 04 2017. [Online]. Available: https://doi.org/10.1063/1.4979815

[60] D. Gasperino, T. Baughman, H. V. Hsieh, D. Bell, and B. H. Weigl, "Improving lateral flow assay performance using computational modeling," *Annual Review of Analytical Chemistry*, vol. 11, no. 1,

pp. 219–244, 2018, pMID: 29595992. [Online]. Available: https://doi.org/10.1146/annurev-anchem-061417-125737

[61] A. Ley, P. Altschuh, V. Thom, M. Selzer, B. Nestler, and P. Vana, "Characterization of a macro porous polymer membrane at micron-scale by confocal-laser-scanning microscopy and 3d image analysis," *Journal of Membrane Science*, vol. 564, pp. 543 – 551, 2018. [Online]. Available: http://www.sciencedirect.com/science/article/pii/S0376738818313048

[62] G. E. Fridley, "Methods and models to control and predict behavior of two dimensional paper networks for diagnostics," Ph.D. dissertation, University of Washington, Seattle, 2014.

[63] N. Sathishkumar and B. J. Toley, "Development of an experimental method to overcome the hook effect in sandwich-type lateral flow immunoassays guided by computational modelling," *Sensors and Actuators B: Chemical*, vol. 324, p. 128756, 2020. [Online]. Available: https://www.sciencedirect.com/science/article/pii/S0925400520311035

[64] M. A. Mansfield, *The use of nitrocellulose membranes in lateral-flow assays*. Totowa, NJ: Humana Press, 2005, pp. 71–85. [Online]. Available: https://doi.org/10.1007/978-1-59259-951-6_4

[65] K. Lee, N. Ivanova, V. Starov, N. Hilal, and V. Dutschk, "Kinetics of wetting and spreading by aqueous surfactant solutions," *Advances in Colloid and Interface Science*, vol. 144, no. 1, pp. 54–65, 2008, designer Molecules for Interfacial Activity, in honour of Alan R. Pitt. [Online]. Available: https://www.sciencedirect.com/science/article/pii/S0001868608001255

[66] S. Suo and Y. Gan, "Tuning capillary flow in porous media with hierarchical structures," *Physics of Fluids*, vol. 33, no. 3, p. 034107, 03 2021. [Online]. Available: https://doi.org/10.1063/5.0038634

[67] M. Liu, S. Suo, J. Wu, Y. Gan, D. AH Hanaor, and C. Chen, "Tailoring porous media for controllable capillary flow," *Journal of Colloid and*

Interface Science, vol. 539, pp. 379–387, 2019. [Online]. Available: https://www.sciencedirect.com/science/article/pii/S0021979718315108

[68] E. Elizalde, R. Urteaga, and C. L. A. Berli, "Rational design of capillary-driven flows for paper-based microfluidics," *Lab Chip*, vol. 15, pp. 2173–2180, 2015. [Online]. Available: http://dx.doi.org/10.1039/C4LC01487A

[69] C. G. Jean-Louis Auriault, Claude Boutin, "Introduction," in *Homogenization of coupled phenomena in heterogenous media*. John Wiley & Sons, Ltd, 2009, pp. 1–26. [Online]. Available: https://onlinelibrary.wiley.com/doi/abs/10.1002/9780470612033.fmatter

[70] R. Altmann, P. Henning, and D. Peterseim, "Numerical homogenization beyond scale separation," *Acta Numerica*, vol. 30, p. 1–86, 2021.

[71] A. Abdulle, O. Budáč, and A. Imboden, "A three-scale offline–online numerical method for fluid flow in porous media," *Journal of Computational Physics*, vol. 337, pp. 175–202, 2017. [Online]. Available: https://www.sciencedirect.com/science/article/pii/S0021999117300992

[72] C. G. Jean-Louis Auriault, Claude Boutin, "An introduction to upscaling methods," in *Homogenization of coupled phenomena in heterogenous media*. John Wiley & Sons, Ltd, 2009, ch. 1, pp. 29–54. [Online]. Available: https://onlinelibrary.wiley.com/doi/abs/10.1002/9780470612033.ch1

[73] S. Whitaker, *The method of volume averaging*, 1st ed. Davis: Springer Dordrecht, November 1998.

[74] J. Niessner, "Multi-scale modeling of multi-phase-multi-component processes in heterogeneous porous media," Ph.D. dissertation, Mitteilungen / Institut für Wasser- und Umweltsystemmodellierung, University of Stuttgart; H. 151, Stuttgart, 2006.

[75] R. J. Atkin and R. E. Craine, "Continuum theories of mixtures: Applications," *IMA Journal of Applied Mathematics*, vol. 17, no. 2, pp. 153–207, 04 1976. [Online]. Available: https://doi.org/10.1093/imamat/17.2.153

[76] J. Hu, S. Wang, L. Wang, F. Li, B. Pingguan-Murphy, T. J. Lu, and F. Xu, “Advances in paper-based point-of-care diagnostics,” *Biosensors and Bioelectronics*, vol. 54, pp. 585–597, 2014. [Online]. Available: https://www.sciencedirect.com/science/article/pii/S095656631300777X

[77] M. Sajid, A.-N. Kawde, and M. Daud, “Designs, formats and applications of lateral flow assay: A literature review,” *Journal of Saudi Chemical Society*, vol. 19, no. 6, pp. 689–705, 2015. [Online]. Available: https://www.sciencedirect.com/science/article/pii/S131961031400129X

[78] J. Tate and G. Ward, “Interferences in immunoassay,” *The Clinical Biochemist Reviews*, vol. 25, no. 2, p. 105, 2004.

[79] M. Griebel, T. Dornseifer, and T. Neunhoeffer, *Numerical simulation in fluid dynamics*. Philadelphia: Society for Industrial and Applied Mathematics, 1998.

[80] H. P. Langtangen and S. Linge, *Finite difference computing with PDEs: A modern software approach*. Cham: Springer Cham, 2017.

[81] P. Altschuh, W. Kunz, M. Bremerich, A. Reiter, M. Selzer, and B. Nestler, “Wicking in porous polymeric membranes: Determination of an effective capillary radius to predict the flow behavior in lateral flow assays,” *Membranes*, vol. 12, no. 7, 2022. [Online]. Available: https://www.mdpi.com/2077-0375/12/7/638

[82] J. Hötzer, A. Reiter, H. Hierl, P. Steinmetz, M. Selzer, and B. Nestler, “The parallel multi-physics phase-field framework PACE3D,” *Journal of Computational Science*, vol. 26, pp. 1–12, 2018.

[83] P. Altschuh, Y. C. Yabansu, J. Hötzer, M. Selzer, B. Nestler, and S. R. Kalidindi, “Data science approaches for microstructure quantification and feature identification in porous membranes,” *Journal of Membrane Science*, vol. 540, pp. 88 – 97, 2017. [Online]. Available: http://www.sciencedirect.com/science/article/pii/S0376738817308347

[84] F. Jamshidi, W. Kunz, P. Altschuh, T. Lu, M. Laqua, A. August, F. Löffler, M. Selzer, and B. Nestler, “A 3D computational method for determination of pores per inch (PPI) of porous structures,” *Materials Today Communications*, vol. 34, p. 105413, 2023. [Online]. Available: https://www.sciencedirect.com/science/article/pii/S2352492823001034

[85] J. Schindelin, I. Arganda-Carreras, E. Frise, V. Kaynig, M. Longair, T. Pietzsch, S. Preibisch, C. Rueden, S. Saalfeld, B. Schmid, J.-Y. Tinevez, D. J. White, V. Hartenstein, K. Eliceiri, P. Tomancak, and A. Cardona, “Fiji: An open-source platform for biological-image analysis,” *Nature Methods*, vol. 9, no. 7, pp. 676–682, 2012.

[86] T. Saito and J.-I. Toriwaki, “New algorithms for euclidean distance transformation of an n-dimensional digitized picture with applications,” *Pattern Recognition*, vol. 27, no. 11, pp. 1551–1565, 1994.

[87] K. Palágyi and A. Kuba, “A 3d 6-subiteration thinning algorithm for extracting medial lines,” *Pattern Recognition Letters*, vol. 19, no. 7, pp. 613–627, 1998.

[88] M. Halisch, E. Vogt, C. Müller, A. Cano-Odena, D. Pattyn, P. Hellebaut, and K. van der Kamp, “Capillary flow porometry-assessment of an alternative method for the determination of flow relevant parameters of porous rocks,” in *Proceedings of international symposium of the society of core analysts, Napa Valley, California, USA*, 2013, pp. 16–19.

[89] L. Hecht, D. van Rossum, and A. Dietzel, “Femtosecond-laser-structured nitrocellulose membranes for multi-parameter point-of-care tests,” *Microelectronic Engineering*, vol. 158, pp. 52–58, 2016, micro and Nano Technologies for Biology and Life Sciences. [Online]. Available: https://www.sciencedirect.com/science/article/pii/S0167931716301320

[90] J. Bico and D. Quéré, “Precursors of impregnation,” *Europhysics Letters (EPL)*, vol. 61, no. 3, pp. 348–353, February 2003. [Online]. Available: https://doi.org/10.1209/epl/i2003-00196-9

[91] G. Løvoll, Y. Méheust, K. J. Måløy, E. Aker, and J. Schmittbuhl, “Competition of gravity, capillary and viscous forces during drainage in a two-dimensional porous medium, a pore scale study,” *Energy*, vol. 30, no. 6, pp. 861–872, 2005, second International Onsager Conference. [Online]. Available: https://www.sciencedirect.com/science/article/pii/S0360544204001860

[92] K. Li, D. Zhang, H. Bian, C. Meng, and Y. Yang, “Criteria for applying the lucas-washburn law,” *Scientific Reports*, vol. 5, p. 14085, 09 2015. [Online]. Available: https://doi.org/10.1038/srep14085

[93] N. Brandt, L. Griem, C. Herrmann, E. Schoof, G. Tosato, Y. Zhao, P. Zschumme, and M. Selzer, “Kadi4mat: A research data infrastructure for materials science,” *Data Science Journal*, vol. 20, no. 1, 2021.

[94] F. Jamshidi, W. Kunz, P. Altschuh, M. Bremerich, R. Przybylla, M. Selzer, and B. Nestler, “Source data belonged to "Geometric flow control in lateral flow assays: Macroscopic single-phase modeling",” June 2022. [Online]. Available: https://doi.org/10.5281/zenodo.6389659

[95] G. Huang, X. Wei, Y. Gu, Z. Kang, L. Lao, L. Li, J. Fan, and D. Shou, “Heterogeneously engineered porous media for directional and asymmetric liquid transport,” *Cell Reports Physical Science*, vol. 3, no. 1, p. 100710, 2022. [Online]. Available: https://www.sciencedirect.com/science/article/pii/S2666386421004409

[96] D. Shou, L. Ye, J. Fan, K. Fu, M. Mei, H. Wang, and Q. Chen, “Geometry-induced asymmetric capillary flow,” *Langmuir*, vol. 30, no. 19, pp. 5448–5454, 2014, pMID: 24762329. [Online]. Available: https://doi.org/10.1021/la500479e

[97] M. S. Wiederoder, S. Smith, P. Madzivhandila, D. Mager, K. Moodley, D. L. DeVoe, and K. J. Land, “Novel functionalities of hybrid paper-polymer centrifugal devices for assay performance enhancement,” *Biomicrofluidics*, vol. 11, no. 5, p. Art.Nr.: 054101, 2017, 43.22.01; LK 01.

[98] T. Williams, C. Kelley, and many others, “Gnuplot 5.0 patchlevel 5: An interactive plotting program,” http://gnuplot.sourceforge.net/, October 2016.

[99] D. Erickson, D. Li, and C. Park, “Numerical simulations of capillary-driven flows in nonuniform cross-sectional capillaries,” *Journal of Colloid and Interface Science*, vol. 250, no. 2, pp. 422–430, 2002. [Online]. Available: https://www.sciencedirect.com/science/article/pii/S002197970298361X

[100] S. Hong and W. Kim, “Dynamics of water imbibition through paper channels with wax boundaries,” *Microfluidics and Nanofluidics*, vol. 19, no. 4, pp. 845–853, 2015. [Online]. Available: https://doi.org/10.1007/s10404-015-1611-3

[101] J. Tirapu-Azpiroz, A. F. Silva, M. E. Ferreira, W. F. L. Candela, P. W. Bryant, R. L. Ohta, M. Engel, and M. B. Steiner, “Modeling fluid transport in two-dimensional paper networks,” *Journal of Micro/Nanolithography, MEMS, and MOEMS*, vol. 17, no. 2, pp. 1 – 10, 2018. [Online]. Available: https://doi.org/10.1117/1.JMM.17.2.025003

[102] E. Fu, S. A. Ramsey, P. Kauffman, B. Lutz, and P. Yager, “Transport in two-dimensional paper networks,” *Microfluidics and Nanofluidics*, vol. 10, no. 1, pp. 29–35, January 2011. [Online]. Available: https://doi.org/10.1007/s10404-010-0643-y

[103] S. Qian and H. H. Bau, “A mathematical model of lateral flow bioreactions applied to sandwich assays,” *Analytical Biochemistry*, vol. 322, no. 1, pp. 89–98, 2003. [Online]. Available: https://www.sciencedirect.com/science/article/pii/S0003269703004949

[104] Z. Liu, J. Hu, A. Li, S. Feng, Z. Qu, and F. Xu, “The effect of report particle properties on lateral flow assays: A mathematical model,” *Sensors and Actuators B: Chemical*, vol. 248, pp. 699–707, 2017. [Online]. Available: https://www.sciencedirect.com/science/article/pii/S092540051730624X

[105] Z. Liu, Z. Qu, R. Tang, X. He, H. Yang, D. Bai, and F. Xu, “An improved detection limit and working range of lateral flow assays based on a mathematical model,” *Analyst*, vol. 143, pp. 2775–2783, 2018. [Online]. Available: http://dx.doi.org/10.1039/C8AN00179K

[106] M. S. Ragavendar and C. M. Anmol, “A mathematical model to predict the optimal test line location and sample volume for lateral flow immunoassays,” in *2012 annual international conference of the IEEE engineering in medicine and biology society*, 2012, pp. 2408–2411.

[107] F. Jamshidi, H. Heimel, M. Hasert, X. Cai, O. Deutschmann, H. Marschall, and M. Wörner, “On suitability of phase-field and algebraic volume-of-fluid openfoam® solvers for gas–liquid microfluidic applications,” *Computer Physics Communications*, vol. 236, pp. 72–85, 2019. [Online]. Available: https://www.sciencedirect.com/science/article/pii/S0010465518303631

[108] F. Jamshidi, S. Bayat, A. Ernst, and B. Nestler, “Geometric flow control in lateral flow assays: Macroscopic two-phase modeling,” *Physics of Fluids*, vol. 36, no. 11, p. 112108, November 2024. [Online]. Available: https://doi.org/10.1063/5.0233556

[109] C. Redondo, G. Rubio, and E. Valero, “On the efficiency of the impes method for two phase flow problems in porous media,” *Journal of Petroleum Science and Engineering*, vol. 164, pp. 427–436, 2018. [Online]. Available: https://www.sciencedirect.com/science/article/pii/S0920410518300780

[110] P. Horgue, C. Soulaine, J. Franc, R. Guibert, and G. Debenest, “An open-source toolbox for multiphase flow in porous media,” *Computer Physics Communications*, vol. 187, pp. 217–226, 2015. [Online]. Available: https://www.sciencedirect.com/science/article/pii/S0010465514003403

[111] R. Brooks and A. Corey, *Hydraulic properties of porous media*, ser. Colorado State University Hydrology Paper. Colorado State University, 1964.

[112] X. Lu, A. Kharaghani, H. Adloo, and E. Tsotsas, “The brooks and corey capillary pressure model revisited from pore network simulations of capillarity-controlled invasion percolation process,” *Processes*, vol. 8, no. 10, 2020. [Online]. Available: https://www.mdpi.com/2227-9717/8/10/1318

[113] S. Patari and P. S. Mahapatra, “Liquid wicking in a paper strip: An experimental and numerical study,” *ACS Omega*, vol. 5, no. 36, pp. 22 931–22 939, 2020, pMID: 32954142. [Online]. Available: https://doi.org/10.1021/acsomega.0c02407

[114] J. Niessner, “The role of interfacial areas in two-phase flow in porous media: Bridging scales and coupling models,” Habilitation thesis, University of Stuttgart, Stuttgart, 2010.

[115] S. E. Buckley and M. C. Leverett, “Mechanism of fluid displacement in sands,” *Transactions of the AIME*, vol. 146, no. 01, pp. 107–116, 1942.

[116] T. E. Johansen, L. A. James, and X. Liu, “On the Buckley-Leverett equation with constant-pressure boundary conditions,” *SPE Journal*, vol. 21, no. 06, pp. 2301–2307, 12 2016. [Online]. Available: https://doi.org/10.2118/183639-PA

[117] A. Bejan and S. Lorente, “Constructal theory of generation of configuration in nature and engineering,” *Journal of Applied Physics*, vol. 100, no. 4, p. 041301, 08 2006. [Online]. Available: https://doi.org/10.1063/1.2221896

[118] ——, “The constructal law and the evolution of design in nature,” *Physics of Life Reviews*, vol. 8, no. 3, pp. 209–240, 2011. [Online]. Available: https://www.sciencedirect.com/science/article/pii/S1571064511000509

[119] A. F. Miguel and L. A. Rocha, *Tree-shaped fluid flow and heat transfer*. Cham: Springer Cham, 2018.

[120] A. F. Miguel, “Toward an optimal design principle in symmetric and asymmetric tree flow networks,” *Journal of Theoretical Biology*, vol. 389,

pp. 101–109, 2016. [Online]. Available: https://www.sciencedirect.com/science/article/pii/S0022519315005263

[121] ——, “A general model for optimal branching of fluidic networks,” *Physica A: Statistical Mechanics and its Applications*, vol. 512, pp. 665–674, 2018. [Online]. Available: https://www.sciencedirect.com/science/article/pii/S0378437118309269

[122] ——, “Constructal branching design for fluid flow and heat transfer,” *International Journal of Heat and Mass Transfer*, vol. 122, pp. 204–211, 2018. [Online]. Available: https://www.sciencedirect.com/science/article/pii/S0017931017355710

[123] X. Zhang and S. Lorente, “Capillary trees for passively pumping water,” *Journal of Physics D: Applied Physics*, vol. 55, no. 16, p. 165503, January 2022. [Online]. Available: https://dx.doi.org/10.1088/1361-6463/ac40ba

[124] W. R. Hess, “Über die periphere Regulierung der Blutzirkulation,” *Pflüger’s Archiv für die gesamte Physiologie des Menschen und der Tiere*, vol. 168, no. 9, pp. 439–490, 08 1917. [Online]. Available: https://doi.org/10.1007/BF01681580

[125] C. D. Murray, “The physiological principle of minimum work: I. the vascular system and the cost of blood volume,” *Proceedings of the National Academy of Sciences*, vol. 12, no. 3, pp. 207–214, 1926.

[126] E. Sciubba, “A critical reassessment of the hess–murray law,” *Entropy*, vol. 18, no. 8, 2016. [Online]. Available: https://www.mdpi.com/1099-4300/18/8/283

[127] V. R. Pepe, L. A. O. Rocha, and A. F. Miguel, “Is it hess-murray law always valid?” in *Proceedings of the constructal law conference 2017*, A.-M. Morega and S. Lorente, Eds. The Publishing House of the Romanian Academy, Bucharest, Romania, May 2017, article, pp. 444–455. [Online]. Available: http://hdl.handle.net/10174/21202

[128] D. Shou, L. Ye, and J. Fan, "Treelike networks accelerating capillary flow," *Physical Review E*, vol. 89, p. 053007, May 2014. [Online]. Available: https://link.aps.org/doi/10.1103/PhysRevE.89.053007

[129] A. Bejan, L. Rocha, and S. Lorente, "Thermodynamic optimization of geometry: T- and y-shaped constructs of fluid streams," *International Journal of Thermal Sciences*, vol. 39, no. 9, pp. 949–960, 2000. [Online]. Available: https://www.sciencedirect.com/science/article/pii/S1290072900011765

[130] B. Soni, A. F. Miguel, and A. Kumar Nayak, "A mathematical analysis for constructal design of tree flow networks under unsteady flow," *Proceedings of the Royal Society A: Mathematical, Physical and Engineering Sciences*, vol. 476, no. 2240, p. 20200377, 2020. [Online]. Available: https://royalsocietypublishing.org/doi/abs/10.1098/rspa.2020.0377

[131] A. Sehn, V. d. R. Pepe, A. F. Miguel, F. Zinani, and L. A. O. Rocha, "Numerical study of non-newtonian fluid flows in y-shaped structures," in *XXXVIII Ibero-Latin American Congress on computational methods in engineering*, 2017.

[132] A. F. Miguel, "Fluid flow in a porous tree-shaped network: Optimal design and extension of hess–murray's law," *Physica A: Statistical Mechanics and its Applications*, vol. 423, pp. 61–71, 2015. [Online]. Available: https://www.sciencedirect.com/science/article/pii/S0378437114010607

[133] S. Lorente and A. Bejan, "Heterogeneous porous media as multiscale structures for maximum flow access," *Journal of Applied Physics*, vol. 100, no. 11, p. 114909, 12 2006. [Online]. Available: https://doi.org/10.1063/1.2396842

List of Figures

List of Tables

Symbols and Abbreviations

Acronyms (first used)

1D	One-dimensional, p. 13
2D	Two-dimensional, p. 75
3D	Three-dimensional, p. 54
A	Analyte, p. 34
BC	Boundary condition, p. 48
BCLW	Bell-Cameron-Lucas-Washburn, p. 31
BiCGSTAB	Biconjugate gradient stabilized, p. 117
CFD	Computational fluid dynamics, p. 47
CL	Control line, p. 33
CLSM	Confocal laser scanning microscopy, p. 55
CN	Cellulose nitrate, p. 33
COVID-19	Coronavirus disease 2019, p. 2
CS	Control surface, p. 22
CT	Computed tomography, p. 55
CV	Control volume, p. 22
EDF	Euclidean distance field, p. 58
FDM	Finite difference method, p. 49
FEM	Finite element method, p. 49
FVM	Finite volume method, p. 49

IMPES	Implicit pressure explicit saturation, p. 116
LED	Light-emitting diode, p. 66
LFA	Lateral flow assay, p. i
LW	Lucas-Washburn, p. 31
P	Detector antibody, p. 34
PA	Analyte-detector antibody complex, p. 33
POCT	Point-of-care testing, p. 2
R	Capture antibody, p. 34
RA	Capture antibody–analyte complex, p. 34
RDT	Rapid diagnostic test, p. 2
RPA	Capture antibody-analyte-detector antibody complex, p. 34
RVE	Representative volume element, p. 42
SWOT	Strengths, weaknesses, opportunities, threats, p. 33
TL	Test line, p. 33
TVD	Total variation diminishing, p. 116
VE	Volume element, p. 42
VT	Voronoi tessellation, p. 54
WHO	World Health Organization, p. 2

Exponents (first used)

b	Brooks-Corey constant, p. 114
m	Cementation exponent, p. 11
(n)	nth time step, p. 94

Greek symbols (first used)

α	Angle between velocity and normal vectors, p. 22	[rad]
β	Intensive property, p. 22	[-]
γ	Surface tension coefficient, p. 18	[$\mathrm{N\,m^{-1}}$]
ε	Porosity, p. 9	[-]

θ	Contact angle, p. 19	[rad]
λ	Mobility, p. 112	$[\mathrm{kg^{-1}\,m\,s}]$
μ	Dynamic viscosity, p. 12	$[\mathrm{kg\,m^{-1}\,s^{-1}}]$
ξ_{eff}	Wicking coefficient, p. 77	$[\mathrm{s\,m^{-2}}]$
ρ	Density, p. 21	$[\mathrm{kg\,m^{-3}}]$
σ	Conductivity, p. 11	$[\mathrm{S\,m^{-1}}]$
τ	Tortuosity, p. 10	[-]
ϕ	Potential, p. 60	[V]

Indices (first used)

α	Phase identifier, p. 110
Ω	Domain of interest, p. 9
a	Association, p. 92
A	Analyte, p. 94
atm	Atmosphere, p. 76
b	Bifurcation level, p. 133
c	Capillary, p. 76
d	Dissociation, p. 92
D	Diffusion, p. 37
eff	Effective, p. 11
en	Entry, p. 114
eq	Equilibrium, p. 96
g	Geometric, p. 10
h	Hydraulic, p. 11
i	ith computational cell, p. 94
$\mathcal{K}$	Kinetic, p. 37
l	Ligament, p. 15
L	Liquid, p. 63

LG	Liquid-gas interface, p. 20
m	Index of summation, p. 80
max	Maximum, p. 114
n	Non-wetting phase, p. 110
n	nth layer, p. 80
nr	Non-wetting phase residual, p. 114
p	Pore (space), p. 9
P	Detector antibody, p. 94
PA	Analyte-detector antibody complex, p. 92
$\mathcal{R}$	Residence, p. 36
RA	Capture antibody-analyte complex, p. 92
RPA	Capture antibody-analyte-detector antibody complex, p. 92
SG	Solid-gas interface, p. 20
SL	Solid-liquid interface, p. 20
TL	Test line, p. 36
Ꝟ	Volume, p. 10
w	Wetting phase, p. 110
wr	Wetting phase residual, p. 114
x, y, z	Three-dimensional spatial dimensions in Cartesian coordinates, p. 57

Operators (first used)

$\nabla\square$	Gradient. p. 12
$\frac{\partial\square}{\partial\square}$	Partial derivative, p. 13
$\Delta\square$	Change in a variable, p. 14
$\frac{d\square}{d\square}$	Ordinary derivative, p. 17

$\square^{\mathrm{T}}$	Transpose, p. 22
$\int\square$	Integral, p. 23
$\nabla\cdot\square$	Divergence, p. 23
$\Sigma\square$	Summation, p. 25
$\nabla^2\square$	Laplacian, p. 26
$\dot{\square}$	Time derivative, p. 26
$\mathcal{O}(\square)$	Order of magnitude, p. 43
$\square \rightleftarrows \square$	Forward and reverse reactions, p. 92
$[\square]$	Concentration, p. 92

Roman symbols (first used)

a	Membrane width as indicator of cross-sectional area, p. 76	$[\mathrm{m}]$
$\mathbf{a}$	Acceleration vector, p. 25	$[\mathrm{m}^2]$
A	Area, p. 15	$[\mathrm{m}^2]$
B	Fluid property, p. 22	
Bo	Bond number, p. 71	[-]
c	Constant in Kozeny-Carman equation, p. 16	[-]
C	Concentration, p. 37	[M]
Ca	Capillary number, p. 27	[-]
CF	Correction factor, p. 60	[-]
CFL	Courant number, p. 103	[-]
CS	Color signal, p. 95	[M]
D	Diffusion coefficient, p. 37	$[\mathrm{m}^2\,\mathrm{s}^{-1}]$
F	Rate of formation, p. 92	$[\mathrm{M}\,\mathrm{s}^{-1}]$
$\mathscr{F}$	Formation factor, p. 11	[-]
$\mathbf{F}$	Force vector, p. 25	[N]
$\mathbf{g}$	Acceleration of gravity vector, p. 26	$[\mathrm{m}\,\mathrm{s}^{-1}]$
h, l, x, z	Length, p. 76	[m]

H	Aggregate length of multiple layers, p. 80	[m]
I	Current , p. 61	[A]
k_a	Association rate constant, p. 92	$[\mathrm{M^{-1}\,s^{-1}}]$
k_B	Forward reaction rate, p. 37	$[\mathrm{M^{-1}\,s^{-1}}]$
k_d	Dissociation rate constant, p. 92	$[\mathrm{s^{-1}}]$
k_r	Relative permeability, p. 111	[-]
K	Permeability, p. 13	$[\mathrm{m^2}]$
$\mathbf{K}$	Second-order Permeability tensor, p. 12	$[\mathrm{m^2}]$
L	Length, p. 10	[m]
m	Mass, p. 22	[kg]
min	Minimum function, p. 103	[-]
$\mathbf{n}$	Normal vector, p. 22	[-]
p	Pressure, p. 12	[Pa]
P	Perimeter, p. 10	[m]
q	Source/sink term, p. 111	$[\mathrm{s^{-1}}]$
Q	Volumetric flow rate, p. 13	$[\mathrm{m^3\,s^{-1}}]$
r	Radius, p. 14	[m]
R	Resistance , p. 61	$[\Omega]$
Re	Reynolds number, p. 63	[-]
S	Saturation, p. 110	[-]
$\mathcal{S}$	Surface, p. 10	$[\mathrm{m^2}]$
t	Wicking time, p. 74	[s]
T	Temperature, p. 22	[K]
$\mathbf{u}$	Darcy velocity vector, p. 12	$[\mathrm{m\,s^{-1}}]$
u	Darcy velocity, p. 13	$[\mathrm{m\,s^{-1}}]$
U	Velocity, p. 13	$[\mathrm{m\,s^{-1}}]$
U,V,W	Velocity components, p. 22	$[\mathrm{m\,s^{-1}}]$

$\mathbf{U}$	Velocity vector, p. 21	$[\mathrm{m\,s^{-1}}]$
$\forall$	Volume, p. 9	$[\mathrm{m^3}]$
$\mathcal{W}$	Work, p. 18	[J]
W	Lambert W function, p. 28	[-]
$\mathscr{W}$	Width, p. 37	[m]
We	Weber number, p. 72	[-]
$\mathbf{x}$	Spatial vector, p. 22	[m]
x,y,z	Three-dimensional spatial dimensions in Cartesian coordinates, p. 12	[m]

A Appendix

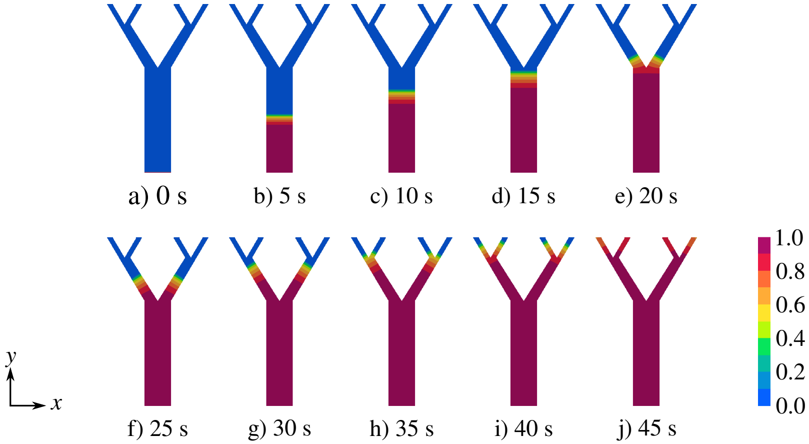

Figure A.1: The wetting phase (water) saturation in Tree1 membrane profile from Table 5.4, where the evolution is displayed every 5 seconds. Reproduced from [108], with the permission of AIP Publishing.

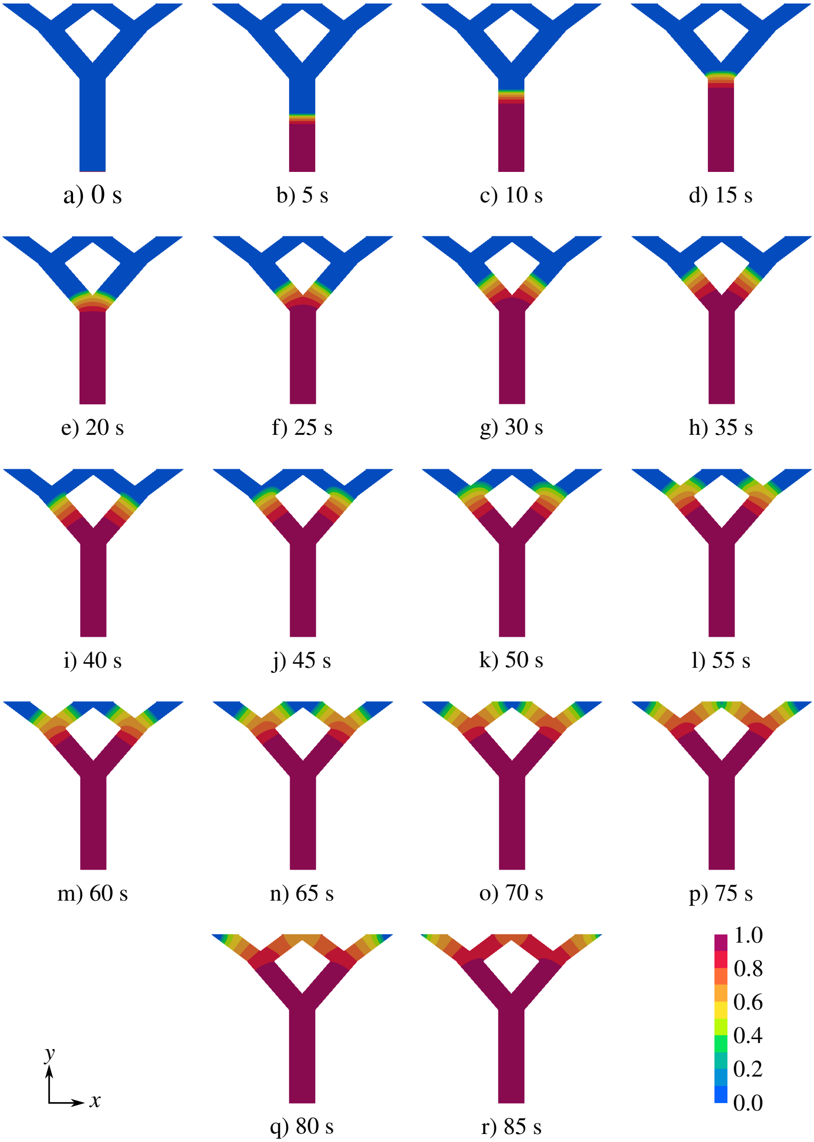

Figure A.2: The wetting phase (water) saturation in Tree3 membrane profile from Table 5.4, where the evolution is displayed every 5 seconds. Reproduced from [108], with the permission of AIP Publishing.

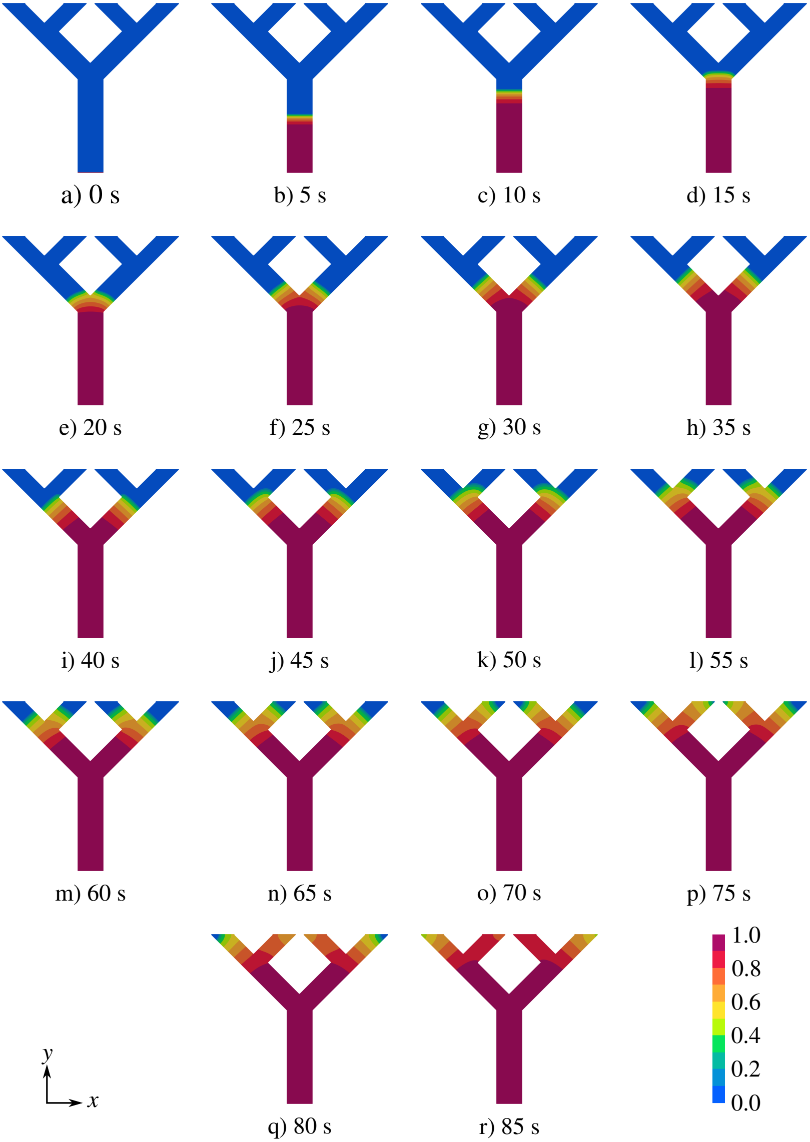

Figure A.3: The wetting phase (water) saturation in Tree4 membrane profile from Table 5.4, where the evolution is displayed every 5 seconds. Reproduced from [108], with the permission of AIP Publishing.

B Publications

Journal articles

[1] **F. Jamshidi**, H. Heimel, M. Hasert, X. Cai, H. Marschall, M. Wörner, "On suitability of phase field and algebraic volume of fluid OpenFOAM® solvers for gas-liquid microfluidic applications", *Computer Physics Communications*, Volume 236, Pages 72-85, March 2019. [Online]. Available: https://doi.org/10.1016/j.cpc.2018.10.015

[2] A. August, **F. Jamshidi**, A. Kneer, R. H. Wolf, M. Wirtz, B. Nestler, "Development of synthetic open porous structures for improved heat transfer", *International Journal of Heat and Mass Transfer*, Volume 159, 120071, October 2020. [Online]. Available: https://doi.org/10.1016/j.ijheatmasstransfer.2020.120071

[3] S. Tavakkol, T. Zirwes, J. A. Denev, **F. Jamshidi**, N. Weber, H. Bockhorn, D. Trimis, "An Eulerian-Lagrangian method for wet biomass carbonization in rotary kiln reactors", *Renewable and Sustainable Energy Reviews*, Volume 139, 110582, April 2021. [Online]. Available: https://doi.org/10.1016/j.rser.2020.110582

[4] **F. Jamshidi**, W. Kunz, P. Altschuh, M. Bremerich, R. Przybylla, M. Selzer, B. Nestler, "Geometric flow control in lateral flow assays: Macroscopic single-phase modeling", *Physics of Fluids*, Volume 34, 062110, June 2022. [Online]. Available: https://doi.org/10.1063/5.0093316

[5] **F. Jamshidi**, W. Kunz, P. Altschuh, T. Lu, M. Laqua, A. August, F. Löffler, M. Selzer, B. Nestler, “A 3D computational method for determination of pores per inch (PPI) of porous structures”, *Materials Today Communications*, Volume 34, 105413, March 2023. [Online]. Available: https://doi.org/10.1016/j.mtcomm.2023.105413

[6] B. Nestler, F. Finsterwalder, L. Wallat, L. Griem, W. Kunz, M. Reder, J. Holland-Cunz, **F. Jamshidi**, M. Selzer, “Neue Materialien mit poröser Mikrostruktur: Beschleunigte Entwicklung durch Simulationen und Datenanalyse”, *Athene - Magazin der Heidelberger Akademie der Wissenschaften 2/2023*, November 2023. [Online]. Available: https://www.hadw-bw.de/Athene-Magazin

[7] **F. Jamshidi**, S. Bayat, A. Ernst, B. Nestler, “Geometric flow control in lateral flow assays: Macroscopic two-phase modeling”, *Physics of Fluids*, Volume 36, 112108, November 2024. [Online]. Available: https://doi.org/10.1063/5.0233556

Conference proceedings paper

[1] S. Tavakkol, T. Zirwes, J. A. Denev, **F. Jamshidi**, H. Bockhorn, “Development of an OpenFOAM solver for numerical simulation of carbonization of biomasses in rotary kilns”, OpenFOAM Workshop, June 2020, Arlington, Virginia, USA. [Online]. Available: https://doi.org/10.5445/IR/1000128493

Conference oral presentations

[1] **F. Jamshidi**, A. August, A. Reiter, A. Kneer, M. Selzer, B. Nestler, “Fluid flow and heat transfer modeling through metal foams or lamella structure”,

International Society for Porous Media – InterPore2019, May 2019, Valencia, Spain.

[2] **F. Jamshidi**, A. Reiter, M. Selzer, B. Nestler, “Fluid simulation of a rising bubble in a quiescent liquid: Coupled Phase-field Navier-Stokes model”, International Symposium on Phase-Field Modelling in Materials Science – PF19, July 2019, Bochum, Germany.

[3] **F. Jamshidi**, A. August, A. Reiter, A. Kneer, M. Selzer, B. Nestler, “Numerical and semi-analytical investigation on forced convection in tubes fully/partially filled with metal foam”, International Society for Porous Media – InterPore2020, September 2020, Online.

[4] **F. Jamshidi**, W. Kunz, B. Nestler, “Fluid flow in porous membranes: Modeling fluid propagation in porous membranes”, Technical Colloquium: Materials Design & Manufacturing, October 2022, Online.

[5] **F. Jamshidi**, A. Ernst, B. Nestler, “Geometric flow control in lateral flow assays”, 6th International Conference on Materials Science & Nanotechnology, September 2023, Rome, Italy.

[6] **F. Jamshidi**, B. Nestler, “Enhancing lateral flow assay sensitivity through computational modeling”, 5th International Conference on Materials Science & Nanotechnology, Future Materials, October 2024, Athens, Greece.

Posters

[1] M. Serres, **F. Jamshidi**, X. Cai, H. Marschall, O. Deutschmann, R. Philippe, V. Vidal, M. Wörner, “Taylor flow entering a porous medium: experiment and simulation”, 15th International Conference on Microreaction Technology (IMRET 2018), October 2018, Karlsruhe, Germany. [Online]. Available: https://publikationen.bibliothek.kit.edu/1000087411

[2] A. A. Gonzalez, W. Kunz, **F. Jamshidi**, P. Altschuh, A. Reiche, M. Bremerich, M. Selzer, B. Nestler, “Lateral flow assay optimization by means of digital modeling”, Jahrestreffen der ProcessNet-Fachgruppen Fluidverfahrenstechnik und Membrantechnik, March 2019, Potsdam, Germany.

[3] **F. Jamshidi**, J. Holland-Cunz, W. Kunz, A. August, B. Nestler, “Digital twins: Synthetic and real porous media”, IAM Networking Seminar – Additive Manufacturing, July 2024, Karlsruhe, Germany. [Online]. Available: https://doi.org/10.5445/IR/1000172580

Dataset

[1] **F. Jamshidi**, W. Kunz, P. Altschuh, M. Bremerich, R. Przybylla; M. Selzer; B. Nestler, “Source data belonged to "Geometric flow control in lateral flow assays: Macroscopic single-phase modeling"”, Zenodo, June 2022. [Online]. Available: https://doi.org/10.5281/zenodo.6389659

Master’s thesis

[1] **F. Jamshidi**, “CFD simulation of an air bubble in microfluidics using Volume of Fluid and Phase Field methods in OpenFOAM”, Karlsruhe Institute of Technology, Institute of Fluid Mechanics (ISTM), July 2016. [Online]. Available: https://publikationen.bibliothek.kit.edu/1000078984

Supervised student theses

[1] X. Hong, “Phase field simulation of a droplet impacting on solid and liquid surfaces using Pace3D”, Bachelor’s thesis, Karlsruhe Institute of Technology (KIT), Institute for Applied Materials - Microstructure Modelling and Simulation (IAM-MMS), June 2018.

[2] L. Xu, “Phase field Simulation of a bubble rising in a quiescent liquid using Pace3D”, Bachelor’s thesis, KIT, IAM-MMS, July 2018.

[3] J. Ji, “Numerical investigation of heat transfer and fluid flow in a circular channel with metal foams or lamella structures”, Bachelor’s thesis, KIT, IAM-MMS and Institute of Thermal Process Engineering (TVT), September 2018.

[4] A. M. Rasnani, “Numerical investigation of heat transfer and fluid flow in a circular channel with metal foams, lamella or shovel structures using Pace3D”, KIT, IAM-MMS, November 2018.

[5] E. Kuschminder, “Numerical study of heat transfer in flow regimes in a pipe with internal porosity”, Diploma thesis, KIT, IAM-MMS and TVT, April 2019.

[6] J. Hötzel, “Numerical and semi-analytical investigation on convective heat transfer in pipes with internal porosity”, Bachelor’s thesis, KIT, IAM-MMS, September 2019.

[7] C. Lu, “Metal Foams: Reconstruction and Simulation”, Master’s thesis, KIT, IAM-MMS, May 2021.

[8] R. Przybylla, “Macroscopic modeling approach for the geometric design of the rapid test strips”, Bachelor’s thesis, KIT, IAM-MMS, September 2021.

[9] T. Lu, “Spatial distribution of pores in porous”, Master’s thesis, KIT, IAM-MMS, March 2022.

[10] D. Böhm, "Weiterentwicklung und Optimierung einer grafischen Nutzeroberfläche zur Auslegung von Diagnostikmembranen", Project work, Karlsruhe University of Applied Sciences (HKA), Institute of Digital Materials Science, July 2022.

[11] B. Herold, "Integration of macroscopic wicking investigations into KadiStudio and its application for automated analysis of diagnostic membranes", Bachelor's thesis, KIT, IAM-MMS, February 2024.